

THE UNDERLYING EVENT IN HARD SCATTERING COLLISIONS
OF PROTON AND ANTIPROTON AT 1.8 TEV

By

RICHARD MARTIN HAAS

A DISSERTATION PRESENTED TO THE GRADUATE SCHOOL
OF THE UNIVERSITY OF FLORIDA IN PARTIAL FULFILLMENT
OF THE REQUIREMENTS FOR THE DEGREE OF
DOCTOR OF PHILOSOPHY

UNIVERSITY OF FLORIDA

2001

UMI Number: 3027520



UMI Microform 3027520

Copyright 2002 by Bell & Howell Information and Learning Company.

All rights reserved. This microform edition is protected against
unauthorized copying under Title 17, United States Code.

Bell & Howell Information and Learning Company
300 North Zeeb Road
P.O. Box 1346
Ann Arbor, MI 48106-1346

ACKNOWLEDGMENTS

It is difficult for me to envision reaching this stage without the support of several people. Whether it was the late-night conversations, the words of encouragement, or the friendship shown by so many, I appreciated the experiences. In particular, there are a few individuals who have played significant roles and whom I wish to expressly thank.

Rick Field provided invaluable advice and guidance over the course of my graduate career at the University of Florida. He created an environment in which I was encouraged to pursue various topics while always having recourse to his counsel. Instead of producing an automaton, this setting yielded an educated and enthusiastic scientist capable of independent thought. Rick's role as a mentor and good-natured willingness to further my development contributed strongly to my progress. His willingness to offer honest words and opinions concerning the significant opportunities available to me inevitably served to aid in casting the best possible decisions. Both friend and advisor, he has taught me much over the last few years.

Originally I began graduate school with the intent of concentrating on theoretical cosmology. While my own interests changed to particle physics, had I continued with astrophysics, I know that I would have enjoyed working for Jim Fry. Jim was one of the first University of Florida professors I met. He always offered good advice and occasionally provided his valuable signature for grant proposals. The choice to follow a different course of study came with some remorse for I considered

Jim to be an excellent physicist and a close friend. Fortunately, he has remained a friend and an individual whose opinion I seek when making difficult decisions. I will miss the ultra-hot Thai food and the insightful conversations.

As a third year student, I had the good fortune to be introduced to experimental particle physics by Guenakh Mitselmakher through a course he taught. He would lace his descriptions of detector anatomy with the stories of various scientists' missed opportunities for a discovery or the excitement of finding new phenomena (several stories of Pontecorvo come to mind). He and his tales added an excitement to particle physics that attracted several young students to the field. Guenakh's dedication, noticeable by the many hours spent in the department at night working, was not lost on me. I know that the CMS end cap muon system will be successful under his guiding hand and wish him the best.

My indoctrination into the culture of CDF would have entailed additional obstacles if not for Andrei Nomerotski. He patiently taught me the intricacies of the Run 1 analysis software in the unfortunately necessary tribal nature of learning how to use the programs. One of the most insightful and intuitive experimentalists I know, he illustrated that simple arguments using reasonable assumptions often serve the same purpose and lead to a better understanding of the physics than the derivation of arbitrarily complex sets of equations. I thank Andrei for enriching my understanding of experimental particle physics.

Several friends have provided fond memories during my time as a graduate student. While it seems unfair to mention only certain individuals, no malice is meant in explicitly thanking them and not others. Brian Baker insured that I saw occasional sunlight with rounds of golf in the spring and assisted with various business

initiatives that allowed for a life outside of physics. The monthly spaghetti Western renaissance fest at Mike Jones' place provided needed breaks. After moving west, movie night was replaced with the biannual pilgrimage to Loard's. Evenings at the Fermilab User's Center with Alexei Safonov always proved interesting. My experience with the intermediate silicon layers for the Run II upgrade would have been less fulfilling if not for Tony Affolder, Chris Hill, and former CDF godparent Joel Goldstein. Conferences at the Stanford Linear Accelerator Center provided opportunities to visit Carey Heckman. The weekend hikes in the Palo Alto foothills and memorable conversations were alone worth the trips.

Without the support and encouragement of both my mother and father, completing my graduate studies would have been much more difficult if not impossible. I cherished the Sunday phone calls and excursions to Fermilab. I can only hope that my achievements have made them proud.

Sisu, the fluffiest cat, was my companion throughout my graduate experience in Florida. Her needs of playing with a ribbon, a warm lap to sit on, and me scratching her head constituted therapeutic relaxation after long days and nights in the department.

Words serve as poor messengers to express the feelings I have for Ilsa Webeck. Her love and encouragement have been priceless during these years.

TABLE OF CONTENTS

ACKNOWLEDGMENTS	ii
LIST OF TABLES	viii
LIST OF FIGURES	x
ABSTRACT	xxii
CHAPTERS	
1 PARTICLE PHYSICS	1
1.1 Historical Prelude	2
1.2 Particles and Forces	8
1.3 Particle Theories	12
2 STANDARD MODEL DYNAMICS	17
2.1 Quantum Chromodynamics	17
2.1.1 Asymptotic Freedom	23
2.1.2 Parton Densities	31
2.1.3 QCD Questions	37
2.2 Hadron Collisions	38
2.3 Modeling Collision Events	42
2.3.1 Monte-Carlo Models	42
2.3.1.1 HERWIG	45
2.3.1.2 ISAJET	47
2.3.1.3 PYTHIA	51
3 THE TEVATRON AND CDF	54
3.1 The Fermilab Accelerators	55
3.2 Collider Detector at Fermilab	62
3.2.1 Silicon Vertex Detector	70
3.2.2 Vertex Tracking Chamber	74
3.2.3 Central Tracking Chamber	76
3.2.4 Calorimeters	81
3.2.5 Muon Chambers	84

3.2.6	Beam Beam Counters	85
3.2.7	Triggers	88
4	DATA CONSTRUCTION AND REDUCTION	94
4.1	Min-Bias Data	95
4.2	Jet20 Data	97
4.3	Z Boson Data	99
4.4	J/ψ B Data	104
4.4.1	J/ψ Selection	107
4.4.2	Event Selection	109
5	DATA ANALYSIS TECHNIQUES	115
5.1	Jet Definitions	117
5.2	$\Delta\phi$ Correlations	118
5.2.1	Angular Correlations in Min-Bias and Jet20 Data	121
5.2.2	Angular Correlations in Z Data	128
5.2.3	Angular Correlations in J/ψ B Data	133
5.3	Systematics	142
6	EVENT STRUCTURE	143
6.1	Event Structure in Dijet Data	143
6.1.1	The Dijet Transverse Region: Theory and Data	149
6.1.1.1	Sources of Charged Particle Multiplicity	154
6.2	Event Structure in Z Data	159
6.2.1	The Z Transverse Region: Theory and Data	164
6.3	Event Structure in J/ψ B Data	170
6.3.1	Event Structure using the Leading Jet	171
6.3.1.1	Comparison of J/ψ and Dijet Data	175
6.3.2	Event Structure using the J/ψ	180
6.3.2.1	Comparison of J/ψ and Z Data	185
7	CONCLUSION	192
7.1	Theoretical Comparisons	192
7.2	The Underlying Event	194
7.3	Future Endeavors	195
APPENDICES		
A	NOTATION	197
A.1	Metric, Four Vectors, and Operators	197
A.2	Levi-Civita Tensor	198

B	MATRIX PROPERTIES	199
B.1	Gamma Matrices	199
B.2	Gell-Mann Matrices	202
C	DATA SYSTEMATICS	205
	REFERENCES	209
	BIOGRAPHICAL SKETCH	215

LIST OF TABLES

1.1	The fundamental fermions in the Standard Model.	9
1.2	Standard Model gauge boson properties and mediated forces.	11
3.1	CDF detector systems. The systems are composed of several elements which are denoted by various abbreviations.	69
3.2	Characteristics of the CDF calorimeters. Segmentation corresponds to the tower size in $\Delta\eta \times \Delta\phi$ and energy resolution is given by σ_E/\sqrt{E} with energy measured in GeV. The symbol \oplus in the energy resolution denotes addition of the constant term in quadrature. . .	84
3.3	CDF Level 1, 2, and 3 trigger acceptance rates at an instantaneous luminosity of $5 \times 10^{30} \text{ cm}^{-2} \text{ sec}^{-1}$	89
4.1	The Min-Bias data sample used in the analysis of the underlying event.	96
4.2	Track selection criteria for the Min-Bias data sample.	97
4.3	Level 1, Level 2, and combined prescaling factors for the Jet20, Jet50, Jet70, and Jet100 data samples.	98
4.4	The Jet20 data sample used in the analysis of the underlying event.	98
4.5	Selection criteria for the inclusive electron data sample.	100
4.6	Selection criteria for the loose Z data sample.	101
4.7	Track selection criteria for the Z data sample.	104
4.8	Number of events satisfying the selection criteria used to create the Z sample.	104
4.9	CDF Level 2 dimuon triggers.	108
4.10	Selection criteria which form a data sample containing J/ψ candidates predominately from B decay.	113

4.11	Selection criteria to create a data sample containing J/ψ candidates with high efficiency in the CTC and characteristics appropriate to the underlying event analysis.	114
7.1	Average charged multiplicity and scalar p_T sum in the transverse regions for the data samples used in this analysis.	194

LIST OF FIGURES

2.1	Feynman diagram for the tree level quark-gluon vertex.	30
2.2	Feynman diagrams for tree level $q\bar{q}$ production from $q\bar{q}$ and gluon pairs.	31
2.3	Illustration of a $p\bar{p}$ collision in which a “hard” 2-to-2 parton scattering with transverse momentum, p_T^{hard} , has occurred. The resulting “dijet” event contains particles that originate from the two outgoing partons (plus final-state radiation) and particles that come from the breakup of the proton and antiproton (i.e. “beam-beam remnants”).	40
2.4	Illustration of a $p\bar{p}$ collision in which multiple parton interactions have occurred. In addition to the “hard” 2-to-2 parton scattering with transverse momentum p_T^{hard} , there is an additional “semi-hard” parton-parton scattering that contributes particles to the underlying event. For PYTHIA, we include the contributions from multiple parton scattering in the beam-beam remnant component.	40
2.5	Illustration of a $p\bar{p}$ collision in which a Z boson with large transverse momentum, $p_T(Z)$, has been produced. The resulting event contains particles that originate from the “away-side” outgoing parton (plus final-state radiation) and particles that come from the breakup of the proton and antiproton (i.e. “beam-beam remnants”).	41
3.1	The ensemble of accelerators used for Run I of the Tevatron. The experiment begins in the Cockroft-Walton generator (not shown in the figure) located before the linear accelerator. The Main Ring and Tevatron physically share the same tunnel.	56
3.2	Mechanism to produce antiprotons. Protons collide with a target which gives rise to a broad spectrum of secondary particles. The secondary particles are focused by a lithium lens. A pulsed dipole magnet selects antiprotons, while the remaining particles are directed towards a beam dump.	59

3.3	Schematic of one quarter of the CDF detector for Run 1. The placement and dimensions of the forward calorimeter is incorrect in the figure, but has been included to illustrate the pseudorapidity range of CDF.	63
3.4	A schematic of a SVX ladder for an inner barrel layer. Three silicon detectors are wirebonded together and attached to readout electronics mounted on a common support structure. The dummy ear is connected to a corresponding ladder in another SVX barrel. . . .	72
3.5	Configuration of the ladders within a SVX barrel and the accompanying support instrumentation.	73
3.6	Views of the VTX from the CDF event display software package in both r - ϕ (left) and r - z (right). The r - ϕ view identifies the VTX octants containing sense wire hits. The r - z view shows the sense wire hits within the 28 drift modules. The positions of the SVX barrels are noted by the two large boxes within the VTX. Calorimetry information is provided in both views by the rectangular indicators outside of the VTX. The crosses along the beamline in the r - z view represent reconstructed vertices. A high-quality primary vertex is indicated by the large seriffed cross. The event pseudorapidity is calculated from this vertex and marked on the outside of the VTX r - z view.	75
3.7	View of the central tracking chamber end plate. The wire slot locations of the nine superlayers are shown. The larger cells are located in the axial layers, whereas the smaller cells are in the stereo layers.	78
3.8	Segmentation of the calorimeter system at CDF in η - ϕ space. For $\phi \sim 45^\circ$, the shaded region at $\eta \sim 3.6$ represents only electromagnetic calorimeter coverage and the dark region at $\eta \sim 4.0$ represents no calorimeter coverage. The complete system is composed of eight such figures.	82
3.9	CDF central muon coverage in η - ϕ . The ϕ gaps in the CMX detector occur when the CMX intersects the floor (large gap) and the Tevatron (small gap).	86
4.1	Histogram of the invariant mass distribution constructed from the two leading electrons. The shaded region corresponds to events with $ \eta_Z \leq 4$ and $81.187 \leq M(e^+e^-) \leq 101.187 \text{ GeV}/c^2$	103

4.2	Illustration of an event in the r - ϕ plane with primary and secondary vertices. Lines with arrows represent particle tracks. The two dimensional distance between vertices is given by L_{xy} . The distance of closest approach to the primary vertex for extrapolated tracks is the impact parameter, d	106
4.3	Pseudo-proper decay length distributions for prompt and B decay produced J/ψ . Both distributions are normalized to the same scale.	112
5.1	Toward, away, and transverse regions for azimuthal angles in the plane perpendicular to the beam axis (left). With $ \eta \leq 1$, each of these three regions corresponds to an area of $4\pi/3$ in $\eta - \phi$ space (right).	120
5.2	The average charged multiplicity as a function of the angles between the leading jet and the tracks for $p_T(\text{jet1}) \geq 5$. The angular bin size is 3.6° . Indicated are the towards, transverse, and away regions as defined in equations 5.2, 5.3, and 5.4, respectively. The leading jet tracks are included in the towards direction.	122
5.3	The average scalar sum of transverse momentum as a function of the angles between the leading jet and the tracks for $p_T(\text{jet1}) \geq 5$. The angular bin size is 3.6° . Indicated are the towards, transverse, and away regions as defined in equations 5.2, 5.3, and 5.4, respectively. The leading jet tracks are included in the towards direction.	123
5.4	The average charged multiplicity as a function of the angles between the leading jet and the tracks for $p_T(\text{jet1}) \geq 30$. The angular bin size is 3.6° . Indicated are the towards, transverse, and away regions as defined in equations 5.2, 5.3, and 5.4, respectively. The leading jet tracks are included in the towards direction.	125
5.5	The average scalar sum of transverse momentum as a function of the angles between the leading jet and the tracks for $p_T(\text{jet1}) \geq 30$. The angular bin size is 3.6° . Indicated are the towards, transverse, and away regions as defined in equations 5.2, 5.3, and 5.4, respectively. The leading jet tracks are included in the towards direction.	126

5.6	The average charged multiplicity as a function of the angles between the Z boson and the tracks for $p_T(Z) \geq 5$. The angular bin size is 3.6° . Indicated are the towards, transverse, and away regions as defined in equations 5.2, 5.3, and 5.4, respectively. The Z boson decay products have been removed.	129
5.7	The average scalar sum of transverse momentum as a function of the angles between the Z boson and the tracks for $p_T(Z) \geq 5$. The angular bin size is 3.6° . Indicated are the towards, transverse, and away regions as defined in equations 5.2, 5.3, and 5.4, respectively. The Z boson decay products have been removed.	130
5.8	The average charged multiplicity as a function of the angles between the Z boson and the tracks for $p_T(Z) \geq 30$. The angular bin size is 3.6° . Indicated are the towards, transverse, and away regions as defined in equations 5.2, 5.3, and 5.4, respectively. The Z boson decay products have been removed.	131
5.9	The average scalar sum of transverse momentum as a function of the angles between the Z boson and the tracks for $p_T(Z) \geq 30$. The angular bin size is 3.6° . Indicated are the towards, transverse, and away regions as defined in equations 5.2, 5.3, and 5.4, respectively. The Z boson decay products have been removed.	132
5.10	The average charged multiplicity as a function of the angles between the leading jet and the tracks for $p_T(\text{jet1}) \geq 5$. The angular bin size is 3.6° . Indicated are the towards, transverse, and away regions as defined in equations 5.2, 5.3, and 5.4, respectively. The leading jet tracks are included in the towards direction.	134
5.11	The average scalar sum of transverse momentum as a function of the angles between the leading jet and the tracks for $p_T(\text{jet1}) \geq 5$. The angular bin size is 3.6° . Indicated are the towards, transverse, and away regions as defined in equations 5.2, 5.3, and 5.4, respectively. The leading jet tracks are included in the towards direction.	135
5.12	The average charged multiplicity as a function of the angles between the leading jet and the tracks for $p_T(\text{jet1}) \geq 30$. The angular bin size is 3.6° . Indicated are the towards, transverse, and away regions as defined in equations 5.2, 5.3, and 5.4, respectively. The leading jet tracks are included in the towards direction.	136

5.13	The average scalar sum of transverse momentum as a function of the angles between the leading jet and the tracks for $p_T(\text{jet1}) \geq 30$. The angular bin size is 3.6° . Indicated are the towards, transverse, and away regions as defined in equations 5.2, 5.3, and 5.4, respectively. The leading jet tracks are included in the towards direction.	137
5.14	The average charged multiplicity as a function of the angles between the J/ψ and the tracks for $p_T(J/\psi) \geq 5$. The angular bin size is 3.6° . Indicated are the towards, transverse, and away regions as defined in equations 5.2, 5.3, and 5.4, respectively. The J/ψ decay products have been removed.	138
5.15	The average scalar sum of transverse momentum as a function of the angles between the J/ψ and the tracks for $p_T(J/\psi) \geq 5$. The angular bin size is 3.6° . Indicated are the towards, transverse, and away regions as defined in equations 5.2, 5.3, and 5.4, respectively. The J/ψ decay products have been removed.	139
5.16	The average charged multiplicity as a function of the angles between the J/ψ and the tracks for $p_T(J/\psi) \geq 30$. The angular bin size is 3.6° . Indicated are the towards, transverse, and away regions as defined in equations 5.2, 5.3, and 5.4, respectively. The J/ψ decay products have been removed.	140
5.17	The average scalar sum of transverse momentum as a function of the angles between the J/ψ and the tracks for $p_T(J/\psi) \geq 30$. The angular bin size is 3.6° . Indicated are the towards, transverse, and away regions as defined in equations 5.2, 5.3, and 5.4, respectively. The J/ψ decay products have been removed.	141
6.1	Dijet data for the average number of charged particles as a function of the transverse momentum of the leading charged jet. The contribution from the leading charged jet is included. The solid and open boxes represent data from the Min-Bias and Jet20 samples, respectively. The bin size in $p_T(\text{jet1})$ is 1 GeV/c. The uncertainty for the uncorrected data points combines statistical and correlated systematic uncertainties.	144

6.2	Dijet data for the average number of toward, away, and transverse charged particles as a function of the transverse momentum of the leading charged jet. The contribution from the leading charged jet is included. The solid and open boxes represent data from the Min-Bias and Jet20 samples, respectively. The bin size in $p_T(\text{jet1})$ is 1 GeV/c. The uncertainty for the uncorrected data points combines statistical and correlated systematic uncertainties.	146
6.3	Dijet data for the average scalar p_T sum of toward, away, and transverse charged particles as a function of the transverse momentum of the leading charged jet. The contribution from the leading charged jet is included. The solid and open boxes represent data from the Min-Bias and Jet20 samples, respectively. The bin size in $p_T(\text{jet1})$ is 1 GeV/c. The uncertainty for the uncorrected data points combines statistical and correlated systematic uncertainties.	148
6.4	Comparison between dijet data and theoretical predictions for the average number of charged particles as a function of $p_T(\text{jet1})$. The contribution from the leading charged jet is included. The solid and open boxes represent data in 1 GeV/c bins from the Min-Bias and Jet20 samples, respectively. The theoretical predications are generated by the QCD hard scattering models of HERWIG, ISAJET, and PYTHIA and have been corrected for the CTC efficiency. The uncertainty for the uncorrected data points combines statistical and correlated systematic uncertainties.	150
6.5	Comparison between dijet data and theoretical predictions in the transverse region for the average number of charged particles as a function of $p_T(\text{jet1})$. The contribution from the leading charged jet is included. The solid and open triangles represent data in 1 GeV/c bins from the Min-Bias and Jet20 samples, respectively. The theoretical predications are generated by the QCD hard scattering models of HERWIG, ISAJET, and PYTHIA and have been corrected for the CTC efficiency. The uncertainty for the uncorrected data points combines statistical and correlated systematic uncertainties.	151

6.6	Comparison between dijet data and theoretical predictions in the transverse region for the average scalar p_T sum of charged particles as a function of $p_T(\text{jet1})$. The contribution from the leading charged jet is included. The solid and open triangles represent data in 1 GeV/c bins from the Min-Bias and Jet20 samples, respectively. The theoretical predictions are generated by the QCD hard scattering models of HERWIG, ISAJET, and PYTHIA and have been corrected for the CTC efficiency. The uncertainty for the uncorrected data points combines statistical and correlated systematic uncertainties.	153
6.7	Dijet data and predictions from HERWIG for the average number of charged particles as a function of $p_T(\text{jet1})$ in the transverse region. Theoretical hard scattering and beam beam remnant contributions are isolated. The solid and open boxes represent data in 1 GeV/c bins from the Min-Bias and Jet20 samples, respectively. The theoretical predictions have been corrected for the CTC efficiency. The uncertainty for the uncorrected data points combines statistical and correlated systematic uncertainties.	155
6.8	Dijet data and predictions from ISAJET for the average number of charged particles as a function of $p_T(\text{jet1})$ in the transverse region. Theoretical hard scattering and beam beam remnant contributions are isolated. The solid and open boxes represent data in 1 GeV/c bins from the Min-Bias and Jet20 samples, respectively. The theoretical predictions have been corrected for the CTC efficiency. The uncertainty for the uncorrected data points combines statistical and correlated systematic uncertainties.	156
6.9	Dijet data and predictions from PYTHIA for the average number of charged particles as a function of $p_T(\text{jet1})$ in the transverse region. Theoretical hard scattering and beam beam remnant contributions are isolated. The solid and open boxes represent data in 1 GeV/c bins from the Min-Bias and Jet20 samples, respectively. The theoretical predictions have been corrected for the CTC efficiency. The uncertainty for the uncorrected data points combines statistical and correlated systematic uncertainties.	157

6.10	Comparison of the average charged particle multiplicity arising from the hard scattering component (left) and beam beam remnants (right) as a function of the transverse momentum of the leading charged jet as generated by HERWIG, ISAJET, and PYTHIA. The theoretical predications have been corrected for the CTC efficiency.	158
6.11	Z boson data for the average number of charged particles excluding Z boson decay products as a function of the transverse momentum of the Z boson. The bin size is 5 GeV/c. The errors on the (uncorrected) data include both statistical and correlated systematic uncertainties.	160
6.12	Z boson data for the average number of toward, away, and transverse charged particles excluding Z boson decay products as a function of the transverse momentum of the Z boson. The bin size is 5 GeV/c. The errors on the (uncorrected) data include both statistical and correlated systematic uncertainties.	161
6.13	Z boson data for the average scalar p_T sum of charged particles excluding Z boson decay products as a function of the transverse momentum of the Z boson. The bin size is 5 GeV/c. The errors on the (uncorrected) data include both statistical and correlated systematic uncertainties.	162
6.14	Z boson data for the average scalar p_T sum of toward, away, and transverse charged particles excluding Z boson decay products as a function of the transverse momentum of the Z boson. The bin size is 5 GeV/c. The errors on the (uncorrected) data include both statistical and correlated systematic uncertainties.	163
6.15	Comparison between Z boson data and theoretical predictions for the average number of charged particles excluding Z boson decay products as a function of $p_T(Z)$. The solid triangles represent Z boson data in 5 GeV/c bins. The theoretical predications are generated by the QCD hard scattering models of ISAJET and PYTHIA and have been corrected for the CTC efficiency. The uncertainty for the uncorrected data points combines statistical and correlated systematic uncertainties.	166

6.16	Comparison between Z boson data and theoretical predictions in the transverse region for the average number of charged particles excluding Z boson decay products as a function of $p_T(Z)$. The solid triangles represent Z boson data in 5 GeV/c bins. The theoretical predictions are generated by the QCD hard scattering models of ISAJET and PYTHIA and have been corrected for the CTC efficiency. The uncertainty for the uncorrected data points combines statistical and correlated systematic uncertainties.	167
6.17	Comparison between Z boson data and theoretical predictions for the average scalar p_T sum of charged particles excluding Z boson decay products as a function of $p_T(Z)$. The solid triangles represent Z boson data in 5 GeV/c bins. The theoretical predictions are generated by the QCD hard scattering models of ISAJET and PYTHIA and have been corrected for the CTC efficiency. The uncertainty for the uncorrected data points combines statistical and correlated systematic uncertainties.	168
6.18	Comparison between Z boson data and theoretical predictions in the transverse region for the average scalar p_T sum of charged particles excluding Z boson decay products as a function of $p_T(Z)$. The solid triangles represent Z boson data in 5 GeV/c bins. The theoretical predictions are generated by the QCD hard scattering models of ISAJET and PYTHIA and have been corrected for the CTC efficiency. The uncertainty for the uncorrected data points combines statistical and correlated systematic uncertainties.	169
6.19	J/ψ B data for the average number of charged particles as a function of $p_T(\text{jet1})$. The contribution from the leading charged jet is included. The bin size in $p_T(\text{jet1})$ is 2 GeV/c. The uncertainty for the uncorrected data points combines statistical and correlated systematic uncertainties.	171
6.20	J/ψ B data for the average number of toward, away, and transverse charged particles as a function of $p_T(\text{jet1})$. The contribution from the leading charged jet is included. The bin size in $p_T(\text{jet1})$ is 2 GeV/c. The uncertainty for the uncorrected data points combines statistical and correlated systematic uncertainties.	172

6.21	J/ψ B data for the average scalar p_T sum of charged particles as a function of $p_T(\text{jet1})$. The contribution from the leading charged jet is included. The bin size in $p_T(\text{jet1})$ is 2 GeV/c. The uncertainty for the uncorrected data points combines statistical and correlated systematic uncertainties.	173
6.22	J/ψ B data for the average scalar p_T sum of toward, away, and transverse charged particles as a function of $p_T(\text{jet1})$. The contribution from the leading charged jet is included. The bin size in $p_T(\text{jet1})$ is 2 GeV/c. The uncertainty for the uncorrected data points combines statistical and correlated systematic uncertainties.	174
6.23	Comparison of average number of charged particles in the dijet (solid and open boxes) and J/ψ B (crosses) samples as a function of $p_T(\text{jet1})$. The bin size for the dijet and J/ψ B data is 1 and 2 GeV/c, respectively. The uncertainty for the uncorrected data points combines statistical and correlated systematic uncertainties.	176
6.24	Comparison of average number of charged particles in the dijet (solid and open boxes) and J/ψ B (crosses) samples for the transverse region as a function of $p_T(\text{jet1})$. The bin size for the dijet and J/ψ B data is 1 and 2 GeV/c, respectively. The uncertainty for the uncorrected data points combines statistical and correlated systematic uncertainties.	177
6.25	Comparison of average scalar p_T sum in the dijet (solid and open boxes) and J/ψ B (crosses) samples for the transverse region as a function of $p_T(\text{jet1})$. The bin size for the dijet and J/ψ B data is 1 and 2 GeV/c, respectively. The uncertainty for the uncorrected data points combines statistical and correlated systematic uncertainties.	179
6.26	J/ψ B data for the average number of charged particles as a function of $p_T(J/\psi)$. The muons from the J/ψ decay have been removed. The bin size in $p_T(J/\psi)$ is 2 GeV/c. The uncertainty for the uncorrected data points combines statistical and correlated systematic uncertainties.	181

6.27	J/ψ B data for the average number of toward, away, and transverse charged particles as a function of $p_T(J/\psi)$. The muons from the J/ψ decay have been removed. The bin size in $p_T(J/\psi)$ is 2 GeV/c. The uncertainty for the uncorrected data points combines statistical and correlated systematic uncertainties.	182
6.28	J/ψ B data for the average scalar p_T sum of charged particles as a function of $p_T(J/\psi)$. The contribution from the leading charged jet is included. The bin size in $p_T(J/\psi)$ is 2 GeV/c. The uncertainty for the uncorrected data points combines statistical and correlated systematic uncertainties.	183
6.29	J/ψ B data for the average scalar p_T sum of toward, away, and transverse charged particles as a function of $p_T(J/\psi)$. The muons from the J/ψ decay have been removed. The bin size in $p_T(J/\psi)$ is 2 GeV/c. The uncertainty for the uncorrected data points combines statistical and correlated systematic uncertainties.	184
6.30	Comparison of average number of charged particles in the Z boson (solid boxes) sample as a function of $p_T(Z)$ and J/ψ B (crosses) sample as a function of $p_T(J/\psi)$. The bin size for the Z and J/ψ B data is 5 and 2 GeV/c, respectively. The uncertainty for the uncorrected data points combines statistical and correlated systematic uncertainties.	186
6.31	Comparison of average number of charged particles for the transverse region in the Z boson (solid boxes) sample as a function of $p_T(Z)$ and J/ψ B (crosses) sample as a function of $p_T(J/\psi)$. The bin size for the Z and J/ψ B data is 5 and 2 GeV/c, respectively. The uncertainty for the uncorrected data points combines statistical and correlated systematic uncertainties.	187
6.32	Comparison of average scalar p_T sum in the Z boson (solid boxes) sample as a function of $p_T(Z)$ and J/ψ B (crosses) sample as a function of $p_T(J/\psi)$. The bin size for the Z and J/ψ B data is 5 and 2 GeV/c, respectively. The uncertainty for the uncorrected data points combines statistical and correlated systematic uncertainties.	189

6.33	Comparison of average scalar p_T sum for the transverse region in the Z boson (solid boxes) sample as a function of $p_T(Z)$ and J/ψ B (crosses) sample as a function of $p_T(J/\psi)$. The bin size for the Z and J/ψ B data is 5 and 2 GeV/c, respectively. The uncertainty for the uncorrected data points combines statistical and correlated systematic uncertainties.	190
C.1	Systematic uncertainty associated with the overall average charge multiplicity as a function of the leading charged jet for the dijet sample. The solid and open boxes represent the uncertainty from the Min-Bias and Jet20 data with bin size 1 GeV/c in $p_T(\text{jet1})$, respectively. The crosses are systematics in 2 GeV/c bins derived from Monte Carlo and QFL.	206
C.2	Systematic uncertainty associated with the transverse average charge multiplicity as a function of the leading charged jet for the dijet sample. The solid and open boxes represent the uncertainty from the Min-Bias and Jet20 data with bin size 1 GeV/c in $p_T(\text{jet1})$, respectively. The crosses are systematics in 2 GeV/c bins derived from Monte Carlo and QFL.	207

Abstract of Dissertation Presented to the Graduate School
of the University of Florida in Partial Fulfillment of the
Requirements for the Degree of Doctor of Philosophy

THE UNDERLYING EVENT IN HARD SCATTERING COLLISIONS
OF PROTON AND ANTIPROTON AT 1.8 TEV

By

Richard Martin Haas

August 2001

Chairman: Richard Field
Major Department: Physics

The structure of events created from hard scattering $p\bar{p}$ collisions at $\sqrt{s} = 1.8$ TeV is investigated. Among the various sources which produce observable features, the underlying event represents a poorly understood component. The underlying event consists of particles arising from beam beam remnants, initial state radiation, and possible multiple parton interactions. The non-perturbative QCD dynamics which influence the development of the underlying event obfuscate analytic predictions necessitating the use of parameterizations. In order to characterize the underlying event and validate Monte Carlo predictions for QCD hard scattering events, three data samples are formed. Angular regions with respect to objects assumed to arise from hard scattering interactions are defined in the plane transverse to the beam axis allowing specific behavior to be isolated. The toward and away regions contain dominant contributions from outgoing jets and final state gluon radiation. The transverse region is orthogonal to the plane of the hard scattering collision and is particularly sensitive to the underlying event. Min-Bias and

Jet20 data are combined into the dijet sample and leading charged jet employed as a reference. The Z boson sample is derived from inclusive electron data and the Z transverse momentum used to form angular regions. The J/ψ B sample is constructed from dimuon data selected to be compatible with J/ψ decay. Both leading charged jet and J/ψ are used to define the correlations in azimuth. The overall structure in dijet and Z boson events is found to be similar and in approximate agreement with the QCD models of HERWIG, ISAJET, and PYTHIA. For the transverse region, HERWIG and ISAJET do not reproduce the data accurately while PYTHIA provides a faithful description of the observations. Comparisons between J/ψ B data and the dijet and Z boson samples indicate behavior which is consistent. Subtle differences appear between the Z boson and J/ψ B as a function of J/ψ data potentially indicating a dependence of the underlying event on the particle created in the hard scattering collision. In order to obtain reliable predictions for physics backgrounds in Run II environments, the underlying event must be correctly modeled.

CHAPTER 1

PARTICLE PHYSICS

Our understanding of matter in the Universe and its behavior relies on a close interaction between experiment and theory. In experimental particle physics, giant accelerators are employed to hurl particles into each other producing ferociously violent events. As the energies grow, the resolving power of the accelerator “microscopes” increases allowing physicists to peer more deeply into the structure of matter. Experimenters often search for signatures which theorists have publicized as interesting, only to find behavior at odds with any theory. The theorists then use the observations as input to mold new models which incorporate the perceived oddities and make new predictions. Unfortunately, no fundamentally new particles or processes have been discovered in the last decade¹ allowing theorists time to create some seemingly far-fetched ideas. The completion and construction of several new accelerators will allow experimental particle physicists to embark on a new era in which hopefully expected and unexpected particles and interactions will be found. Critical to unearthing new physics is a proper understanding and modeling of the background processes at high energy described by the current model.

This chapter presents a necessarily broad overview of the historical progression and current status of high energy particle physics. Detailed explanations of what is known as the Standard Model of particles and interactions are reserved for

¹Some would say the measurement of the top quark constituted a fundamental discovery. While a significant and important finding, the lack of a top quark would have been far more surprising and radically altered the structure of the Standard Model.

chapter 2. Explanation of the basic phenomenology of high energy collisions at hadron colliders and motivation for the study of the underlying event is provided at the end of this chapter.

1.1 Historical Prelude

The late 19th and 20th centuries were marked by numerous experimental and theoretical achievements which produced the foundation for modern particle physics. While the expansion of human understanding is generally a cumulative experience, the past one hundred years has been a period of unusual activity with several dramatic discoveries and changes in perception. The development of particle accelerators allowed physicists to utilize shorter wavelength probes to resolve smaller scales. As the ranges decreased, the discovery that matter consisted of fundamental particles smaller than atoms described by new physical laws became apparent.

Observations at the turn of the last century inspired several changes in perception, setting in motion the events which would culminate in our present understanding of particle physics. In 1895, Röntgen produced a novel type of high energy radiation in his laboratory and demonstrated that it could penetrate various substances. The stability of naturally occurring elements came into question when Becquerel observed radioactive uranium in 1897. J.J. Thomson's discovery of the electron and measurement of the charge-to-mass ratio indicating a low mass particle in the same year demonstrated that the atoms were not fundamental. In order to explain the inclusion of negatively charged electrons within neutral atoms, Thomson constructed a model in which the positive charges were scattered ran-

domly about the interior of the atom. In 1900, Planck introduced the unsavory assumption that light was quantized to explain data from blackbody radiation experiments, but noted that this effect must be an artifact of the emission process and not truly a property of light. Physicists at the time believed that the corpuscular model of light had been discredited and favored a formulation in terms of waves. Instead of rejecting quantization, Einstein embraced it in 1905 when he explained the photoelectric effect. The successful description of this effect led to the interpretation that the quantization of the electromagnetic field is a property of the field itself.

Compelled by questions raised in the previous decade, the investigation of the structure of the atom and the quantum behavior of nature followed. Rutherford's 1911 experiment in which α particles were focused onto a gold foil and occasionally deflected at large angles indicated the presence of a massive core within the atom. This finding refuted Thomson's atomic model, which Bohr supplanted in 1914 with one in which electrons orbited a positive nucleus. In 1923, Compton observed that Röntgen's radiation could be scattered from particles at rest, the dynamics of which demonstrated the particle behavior of light. Conversely, matter appeared to have an associated wave characteristic seen in diffraction patterns of electrons. Writing electrons in terms of fields with dynamics described by a quantum theory, Dirac developed an equation in 1927 which was applicable to all half-integer spin particles. The equation predicted that for each charged particle, an antiparticle of opposite charge but with the same mass existed. Anderson found Dirac's antiparticle in 1931 in an experiment which detected a positively charged electron, the positron. The production of a negatively charged antiproton

required several additional years, eventually being observed in 1955 at the Berkeley Bevatron.

In the early 1930s, the conflict between an expected discrete and an observed continuous spectra from nuclear beta decay data prompted Pauli to suggest the presence of a light neutral particle which went undetected in the experiments. Pauli's new particle would produce a three body decay with the constituents carrying variable quantities of the interaction energy. The neutron, discovered in 1932 by Chadwick, was too massive to be a viable candidate for the extra particle. The as yet unobserved light neutral particle was named the neutrino by Fermi in his successful theoretical model of beta decay which incorporated many of Pauli's ideas.

The untenable condition of an atomic nucleus composed of protons and neutrons with only an electromagnetic force capable of forming bound states of ample strength was addressed over the following years. Theorists introduced the strong force with an extremely short effective distance in order to bind the nucleons while not affecting the dynamics at larger scales. In 1934, Yukawa created a theory of strong interactions where the short range of the force was due to mediation by a massive particle. In 1937, particles observed in cosmic ray experiments by Anderson and Neddermeyer, as well as Street and Stevenson, apparently provided evidence for the strong force mediator. Once additional information was obtained, it was realized that the lifetime and mass measurements did not match Yukawa's predictions. Instead, the particles represented a new type of electron, the muon, with significantly more mass.

Direct evidence of the neutrinos postulated by Pauli and Fermi was observed 20 years after the particles' introduction. A series of experiments by Reines and Cowan in the middle of the 1950s examined inverse beta decay, the process in which a neutrino strikes a proton producing a neutron and positron [1]. Unambiguous results of the neutrino's existence were provided by a sensitive detector which measured the characteristics of the neutron and positron. While the decay of a muon to an electron and multiple neutrinos had been inferred from 1949 data by Powell, the decay of a muon to an electron and a photon had not been observed. Once the neutrino's existence was established, this apparent dichotomy in the previous results was explained by Pontecorvo as the consequence of more than one neutrino type and the conservation of lepton number in interactions [2]. Using this scheme, the particle in Reines and Cowan's experiment was classified as an electron neutrino. In 1962, a group lead by Schwartz, Lederman, and Steinberger found the muon neutrino [3].

In the early 1960s, accelerators such as the Brookhaven Cosmotron produced a chaotic assortment of apparently unrelated particles. A tempting organizational structure was proposed by Gell-Mann and Ne'eman in 1961 called the Eightfold Way in which the particles were arranged in geometric patterns according to charge and a new quantum number called strangeness [4]. Groups consisting of particles with the same spin and parity defined supermultiplets. The supermultiplets contained several isospin multiplets. While the discovery of the predicted Ω^- in 1964 lent it further credence, the successful phenomenological model lacked an explanation for the observed patterns.

Gell-Mann and Zweig independently proposed that the particle spectrum could be described by arrangements of three types of constituents denoted as quarks [5, 6]. Unfortunately, identifying certain particles as quark conglomerates appeared to violate the Pauli exclusion principle which prohibits two quarks from occupying the same state. This apparent conflict was ameliorated when Greenberg assigned a new quantum number, color, to each of the quarks [7]. To explain the apparent lack of free quarks and particles carrying color, the quarks were required to bind into composite objects which were color neutral. These seemingly *ad hoc* constraints engendered an aversion to the quark model, compelling the substructure of protons observed in a 1968 Stanford Linear Accelerator experiment reminiscent of Rutherford scattering to be called partons [8]. Unperturbed by the scepticism surrounding quarks, Glashow, Iliopoulos, and Maiani in 1970 predicted the existence of a fourth quark to explain the suppression of neutral kaon decays to muon pairs.

Acceptance of the quark model arose from a series of experimental results which confirmed several predictions. The J/ψ was observed in 1974 by two collaborations and subsequently interpreted as a bound state of the quarks needed to accurately predict neutral kaon decay [9, 10]. This discovery, later known as the November Revolution, prompted wide scale adoption of the quark model. A symmetry between the mathematical organization of the quarks and leptons was now believed to exist. The τ , a new particle with properties similar to those of an electron, was observed in 1975 [11]. This lepton was seen as an indicator of a new family of leptons and quarks. In 1977, the fifth quark was discovered in a bound state called $\Upsilon(1S)$ [12].

Theories concerning the nature of the particle interactions were being developed concurrently with the discoveries of the 1960s and 1970s. The unification of electromagnetic and weak nuclear forces into a single theoretical construct was possible if fundamental symmetries existed between the two forces. When the symmetry was spontaneously broken, the forces appeared as different manifestations of one fundamental interaction. This symmetry breaking was achieved through the introduction of a scalar field which had a non-vanishing vacuum expectation value. Glashow, Weinberg, and Salam incorporated these ideas into their models of electroweak theory [13, 14, 15]. Three massive carriers of the weak force (W^\pm and Z) and a massless carrier of the electromagnetic force (the photon) were predicted. In 1983, the W and Z were observed [16, 17].

Experiments performed since the observations of the electroweak gauge bosons have primarily served to either validate expected phenomena or restrict more fanciful theories. Machines designed to measure the characteristics of the Z , the production and decays of heavy hadrons, and the presence of charge-parity violation were constructed. Immense accelerator complexes were planned which raised the boundaries of energetic collisions at laboratories even higher. Of these, the Tevatron at Fermilab focused protons onto antiprotons and produced the highest center of mass energies. This ability along with sustained periods of data collection allowed the CDF and DØ detectors to observe the long anticipated top quark in 1995 [18, 19]. The remaining absent particle in the third family of fermions, the ν_τ , was found at a fixed target experiment at Fermilab in 2000 [20].

Some results from other investigations may require either a minor extension of the theory describing particle interactions or could be the harbingers of funda-

mentally new physics. Recent data from experiments consisting of large tanks of highly purified water surrounded by photomultiplier tubes looking for Čerenkov light report an apparent mixing between neutrino types, Δm^2 [21]. Whether this effect can be explained by the Standard Model or not remains a subject of controversy and will require further study. Undoubtedly the next decade of particle physics will be exciting with many new machines under development with vastly improved capabilities.

1.2 Particles and Forces

The fundamental particle content of the Standard Model consists of six quarks, six leptons, and four bosons. The quarks and leptons are part of a more general classification of spin 1/2 particles called fermions. These elementary fermions interact through the exchange of integer spin bosons. All observed matter is described to a remarkable degree of precision as being comprised of these components. Whether a substructure to the fundamental particles will be found in Rutherford-like experiments is a subject of ongoing research.

The quarks and leptons constitute the basic fermions in the Standard Model. They are each arranged into three generations of doublets as shown in table 1.1. The specific type of quark or lepton is commonly referred to as flavor. There are six flavors of quarks and six flavors of leptons.

Several properties unique to the quarks are essential in a description of their dynamics. Each quark carries a degree of freedom called color, commonly denoted as red, green, or blue. The quarks exist as fractionally charged particles with u , c , and t having charge $+2/3$ and d , s , and b having charge $-1/3$. Fla-

Table 1.1: The fundamental fermions in the Standard Model.

$$\begin{array}{lll}
\text{quarks:} & \begin{pmatrix} u \\ d \end{pmatrix} & \begin{pmatrix} c \\ s \end{pmatrix} & \begin{pmatrix} t \\ b \end{pmatrix} \\
\text{leptons:} & \begin{pmatrix} \nu_e \\ e \end{pmatrix} & \begin{pmatrix} \nu_\mu \\ \mu \end{pmatrix} & \begin{pmatrix} \nu_\tau \\ \tau \end{pmatrix}
\end{array}$$

For specific quantum numbers are assigned to each quark with the negative of the quantum numbers given to the antiquarks. The s quark carries the parameter of strangeness, defined as $S = -1$. Similarly, the c , b , and t quarks are endowed with charm ($C = 1$), bottom ($B = 1$), and top ($T = 1$), respectively. Specifying quark masses is dependent upon the calculational techniques employed to extract the information from experimental measurements. A current algebra approach produces $m(u) \approx \frac{1}{2}m(d) \approx 5 \text{ MeV}/c^2$ and $m(s) \approx 200 \text{ MeV}/c^2$ [22]. Estimating from charmonium, bottomonium, D meson, and B meson masses, $m(c) \approx 1.2 \text{ GeV}/c^2$ and $m(b) \approx 4.2 \text{ GeV}/c^2$ [22]. Events with t candidates can be reconstructed and a constrained fitting technique used to find $m(t) \approx 175 \text{ GeV}/c^2$ [23]. The reason for such disparate masses is not understood and constitutes one of the major challenges facing theories beyond the Standard Model. The Standard Model does not address the issue itself, treating all fermion masses as free parameters which must be experimentally determined.

The leptons comprise the remaining fundamental fermions, mirroring the structure of the quarks. Charged and neutral leptons exist. The leptons with charge $Q = -1$ are the electron (e), muon (μ), and tau (τ). The neutrinos constitute the neutral leptons and are associated with a corresponding charged lepton to form the electron neutrino (ν_e), muon neutrino (ν_μ), and tau neutrino (ν_τ). Experimentally,

only neutrinos with left-handed polarizations and antineutrinos with right-handed polarizations are found [24, 25]. Generation specific quantum numbers L_e , L_μ , and L_τ are assigned to each lepton with a value of +1 for particles and -1 for antiparticles. Interactions involving leptons conserve these quantum numbers for each generation. The masses of the leptons vary even more radically than those of the quarks. The charged leptons have masses of $m(e) = 0.511 \text{ MeV}/c^2$, $m(\mu) = 105.7 \text{ MeV}/c^2$, and $m(\tau) = 1.777 \text{ GeV}/c^2$ [22]. The masses of the neutrinos are constrained to be extremely small by upper bounds from precision experiments such as tritium double beta decay. The observation of only one helicity for neutrinos further suggests that the neutrino is massless. However, recent experimental evidence indicating oscillations between different neutrino flavors may necessitate non-zero masses [21].

The fermions in table 1.1 interact through gravitational, electromagnetic, weak nuclear, and strong nuclear forces. Since gravitational interactions typically are only of consequence on macroscopic scales and represent the weakest force, they can be ignored between particles at accelerator energies. The electromagnetic force mediates interactions between charged particles. Nuclei and electrons are bound together by the electromagnetic force. The physical and chemical properties of bulk matter are largely determined by electromagnetic interactions. The weak nuclear force can affect all leptons and quarks. It is the only known interaction to alter the flavor of the fermions. Radioactive beta decay represented the first experimental evidence of weak processes in which a neutron decays to a proton, charged lepton, and neutral antilepton. Strong nuclear forces affect only those particles which carry color. Nuclear binding and the interactions among the constituents of nuclei

Table 1.2: Standard Model gauge boson properties and mediated forces.

Particle	Mass (GeV/c ²)	Charge	Spin	Mediates
photon (γ)	0	0	1	Electromagnetism
W^\pm	80.33	± 1	1	Weak
Z	91.187	0	1	Weak
gluon (g)	0	0	1	Strong

are governed by the strong force. The electromagnetic, weak nuclear, and strong nuclear forces are mediated by the exchange of vector bosons between the fermions.

Four gauge bosons exist which carry the fields in the Standard Model. Bosons are integer spin particles with vector, or spin 1, type describing the electromagnetic, weak, and strong fields. The photon (γ) mediates electromagnetic interactions between charged particles and has no mass. The weak force is communicated by massive bosons which are both charged and neutral. The charged weak bosons (W^\pm) have a mass of 80.33 GeV/c² and interact with particles differing by one unit of charge. The Z likewise mediates weak interactions, but is neutral and has a mass of 90.187 GeV/c². Gluons convey the strong force, interacting with particles possessing color. Gluons are massless. In this language, nuclear beta decay is the consequence of W^- emission from a d quark within a neutron. The W^- decays to an electron and electron antineutrino, while the d is transformed into a u quark. The boson characteristics are summarized in table 1.2.

Quarks and gluons bind to form strongly interacting particles called hadrons. Since they carry the quantum number of color, the quarks and gluons cannot be isolated as free particles. Color confinement requires that the quarks combine to create color singlet states. Mesons are color neutral and are composed of two

quarks, $q_\alpha q'_\beta$ with α explicitly representing color. Due to the intrinsic properties of the quarks, the mesons exist as either spin 0 or spin 1 particles with odd parity. Pions and kaons are commonly observed mesons in accelerator collisions. Three quarks can combine to form $q_\alpha q'_\beta q''_\gamma$ with α , β , and γ arranged in such a fashion to create a color singlet state. These particles are referred to as baryons and have half-integer spins. The proton and neutron are both baryons.

Most of the matter in the universe is composed of the fermions found in the first generation of table 1.1. The heavier quarks c , s , t , and b are found only in unstable particles which eventually decay to quarks and leptons of the first generation. The heavier leptons μ and τ also decay to lighter quarks and leptons (discussion of neutrino decay in this context is omitted since it is not known what the neutrino masses are). Analytic descriptions of collision events and decays of states involving color cannot be fully formulated using the perturbative techniques that prove extremely useful for weak and electromagnetic interactions.

1.3 Particle Theories

The evolution of particle theories over the previous decades has culminated in the Standard Model. This model has withstood many exacting experimental results, having been tested repeatedly in extreme detail [26]. Formulated in terms of quantum fields, the theory describes the dynamics of particles interacting via the electromagnetic, weak nuclear, and strong nuclear forces. The development of the Standard Model is reflected in the various components which are individually endowed with specific characteristics of the fields. The equations of quantum electrodynamics (QED) encompass the behavior of charged objects and the force

mediator of the fields, the photon. Quantum chromodynamics (QCD) describe the interactions among particles carrying color with gluons participating as field quanta. Due to the increasing strength of the associated force as distance between particles with color increases, QCD perturbative techniques are limited to certain momenta regimes. This feature of QCD coupling strengths obscures reliable analytic calculations of the underlying event relegating it to the more poorly understood aspects of Standard Model processes at colliders.

QCD, like QED, is a local gauge field theory. Instead of QED's $U(1)$ symmetry, QCD is based on a color $SU(3)$ gauge invariance. Since they are color triplets, quarks and antiquarks transform according to $\mathbf{3}$ and $\bar{\mathbf{3}}$ representations, respectively, of the gauge group $SU(3)$. The quarks interact via the strong force regardless of flavor. Gluons belong to a color octet and transform under a $\mathbf{8}$ representation of $SU(3)$. The gluons couple not only to quarks, but also to other gluons forming three and four point interaction vertices.

The strength of the interaction between quarks and gluons and between gluons themselves is given by the strong coupling constant α_s . Far from being a true constant, the value of α_s changes with differing energy scales. If the energy is below 1 GeV, applying perturbation theory to QCD is unreliable as the coupling becomes very strong. Fortunately, α_s decreases with increasing energy allowing perturbation theory to be employed for QCD calculations in high energy regimes. At sufficiently high energy, asymptotic freedom prescribes that the quarks and gluons be treated as free particles since α_s becomes negligible.

The behavior of α_s for low energies requires that particles carrying color are bound into color singlet objects. As the energy scales decrease, α_s increases re-

sulting in an extremely strong force between quarks, antiquarks, and gluons. The strong force between hadrons differs from that between its constituents because the hadrons are colorless. The hadrons interact via a residual strong force through the interchange of colorless mesons. The quarks and gluons within the hadrons are distributed according to parton distribution functions. The parton distribution functions depend on the structure of the hadron and must be measured. Once a measurement is recorded, the functions are evolved using the Altarelli-Parisi equations resulting in an explicit energy scale dependence.

While predictions from QCD and the other elements of the Standard Model have demonstrated a remarkable concordance with experimental results, several open questions exist. The Higgs particle indicative of the field responsible for the creation of particle masses in the Standard Model has eluded detection. More fundamentally, many topics outside the purview of the Standard Model have generated increasing interest. Preeminent among the unanswered questions is the nature of electroweak symmetry breaking. The vast difference between quark and lepton masses (more than 11 decades!) also remains a mystery, relegated to free parameters within the current theory. In addition, the apparent symmetry between quark and lepton families that is necessary for the Standard Model to be renormalizable must either be due to a fundamental cause or left as a fortuitous coincidence. While three of the forces are successfully incorporated into a single paradigm, the gravitational interactions are conspicuously excluded. Many theories beyond the Standard Model attempt to address these questions.

Obviating the need for elementary scalar bosons, technicolor theories present a dynamical explanation for electroweak symmetry breaking in which chiral symme-

tries are explicitly broken by new gauge interactions [27, 28, 29]. As many models suffer from profound problems or a plethora of arbitrary new parameters, the virtue of technicolor and its progeny (extended technicolor, walking technicolor, top-color assisted technicolor) stems from the desire to create a framework based on well accepted ideas. A technicolor theory established using a complete family of technifermions provides for an extension of the structure of QCD and incorporates an additional technicolor quantum number. Unlike the Standard Model in which quark and lepton masses stem from Yukawa couplings to the Higgs boson, technicolor theories produce quark and lepton masses from explicitly breaking chiral symmetries through gauge interactions alone and therefore are called dynamical.

Supersymmetry (SUSY) introduces a method which can address the problems arising from the inclusion of a Higgs boson within the Standard Model [30]. Precise fine tuning of parameters at each stage of perturbation theory is necessary to cancel the quadratic divergences which appear from the radiative corrections to the Higgs boson for a Standard Model valid to an energy cutoff of the Planck mass. The gauge hierarchy or fine tuning problem refers to this unsettling manner in which a renormalizable theory is obtained. SUSY resolves the problem by providing a symmetry between bosons and fermions. An operator is introduced which changes the angular momentum of particles by $1/2$ without altering mass and other quantum numbers. Since the radiative effects of bosons and fermions enter the equations with opposite sign, SUSY requires no counterterms to cancel quadratic divergences. Therefore, SUSY naturally avoids the fine tuning problem.

The associations between quarks and leptons exemplified by the cancelation of triangle anomalies preserving the renormalizability of the Standard Model pro-

vide inviting hints at potential, fundamental connections. Theories incorporating leptoquarks furnish a mechanism whereby quarks and leptons can couple directly through a Yukawa interaction [31, 32, 33]. Leptoquarks are color triplet bosons with spin 0 or 1. The interactions of scalar leptoquarks are designated parameter free since additional couplings beyond the Yukawa and strong types do not appear. In contrast, vector leptoquark interactions are model dependent with anomalous magnetic and electric quadrupole moments in the color field. Recognizing that they carry the same quantum numbers, color triplet technipions can be identified as scalar leptoquarks. This allows technicolor to provide another source of leptoquark production [34]. Recent experimental limits for second and third generation leptoquarks including technicolor enhancements tightly constrain the potential masses for these particles [35].

The introduction of extra dimensions acting at small characteristic distances eliminates the difference between electroweak and Planck scales effectively solving the hierarchy problem [36]. The large extra dimensional models are inspired by string theory in which gravity is a natural constituent and accommodate both the Standard Model and SUSY. Kaluza-Klein towers of massive gravitons exist which alter the Standard Model processes. A cartoon representation of the extra dimensional models can be visualized by a sheet called a brane to which the Standard Model particles and forces are affixed with the gravitons allowed to propagate in the extra dimensions off of the brane.

Clearly, experimental results will show the first indications of physics beyond the Standard Model. Nothing will focus the attention of experimenters and theorists like new results.

CHAPTER 2 STANDARD MODEL DYNAMICS

2.1 Quantum Chromodynamics

The theory of quantum chromodynamics (QCD) is constructed from a $SU(3)$ non-Abelian gauge group of color describing the strong force. Unlike the one charge associated with QED, QCD incorporates three charges which are mediated by vector particles obeying the $SU(3)$ color symmetry. Color charges are typically denoted as red (R), green (G), and blue (B). This provides a helpful representation for color confinement where equal proportions of color or color, anti-color states exist to create color neutral particles. In addition to the fractional electric charge, quarks carry a color charge. The electrically neutral gluons mediate color exchange and carry two color indices. As a consequence of the non-Abelian nature of QCD, the gluons are capable of self-interactions. Gluons are massless and in principle nine types corresponding to their coupling between initial and final color states exist. A color octet consisting of eight gluons,

$$\begin{aligned}
 g_1 &= R\bar{G} \ , & g_2 &= R\bar{B} \ , \\
 g_3 &= G\bar{R} \ , & g_4 &= G\bar{B} \ , \\
 g_5 &= B\bar{R} \ , & g_6 &= B\bar{G} \ , \\
 g_7 &= \frac{1}{\sqrt{2}} (R\bar{R} - G\bar{G}) \ , \\
 g_8 &= \frac{1}{\sqrt{6}} (R\bar{R} + G\bar{G} - 2B\bar{B}) \ ,
 \end{aligned} \tag{2.1}$$

and a color singlet with one gluon,

$$g_0 = \frac{1}{\sqrt{3}} (R\bar{R} + G\bar{G} + B\bar{B}) , \quad (2.2)$$

comprise the possible varieties. The inclusion of the singlet state which is unaffected by color confinement would entail the possibility of gluons existing as free particles. Worse yet, the color singlet gluon could be exchanged between any two color singlets producing a long range strong force. Since $SU(3)$ only requires eight gluons, the color singlet can be rejected. Therefore, QCD describes a color $SU(3)$ symmetry applicable to an octet of gluons and three colors for each quark.

The color $SU(3)$ group is constructed from 8 generators \mathbf{T}_a where $a = 1, \dots, 8$. These generators satisfy the commutation relation

$$[\mathbf{T}_a, \mathbf{T}_b] = if_{abc}\mathbf{T}_c , \quad (2.3)$$

where the structure functions f_{abc} are real constants which are antisymmetric in a , b , and c . Written in terms of 3×3 Hermitian matrices in the $\mathbf{3}$ representation, the generators are related to the Gell-Mann matrices λ_a by

$$T_a = \frac{1}{2}\lambda_a . \quad (2.4)$$

Utilizing the Gell-Mann matrices and solving equation 2.3, values of the structure functions valid for any representation of the group can be determined. The explicit forms of the Gell-Mann matrices and the values of f_{abc} can be found in appendix B.2.

The strength of the interaction between colored particles is determined by the strong coupling constant g_s . Since it appears in the QCD Lagrangian, g_s is also referred to as the $SU(3)$ coupling parameter. Observable quantities such as the differential cross sections are calculated from squares of scattering amplitudes for QCD processes. The appearance of g_s^2 motivates a definition similar to the fine structure constant in QED for QCD, written as

$$\alpha_s = \frac{g_s^2}{4\pi}. \quad (2.5)$$

Commonly, both g_s and α_s are referred to in the literature as the QCD coupling constant with the meaning clear from the context.

The dynamics of QCD are specified by a Lagrangian involving fermion and gauge fields with the colors taken into account. The fermion fields representing the quarks are denoted as $\psi_i^{(\alpha)}$ with possible values 1, 2, and 3 for the color index i and $u, d, c, s, t,$ and b for the flavor label α . The color index can be suppressed and the fermion field written as a vector

$$\psi = \begin{pmatrix} \psi_1 \\ \psi_2 \\ \psi_3 \end{pmatrix} \quad (2.6)$$

where the terms ψ_i are each 4-component Dirac spinors. The gauge fields describing the gluons are given by G_a^μ . Vector particles associated with the gauge fields are assured by the use of a Lorentz index μ allowing G_a^μ to transform under spatial rotations in the same manner as ∂^μ . The index a ranges from 1 to 8 reflecting

the eight generators of color $SU(3)$ given in the fundamental representation by the Gell-Mann matrices. The QCD Lagrangian in terms of these fermion and gauge fields is

$$\mathcal{L}_{\text{QCD}} = -\frac{1}{4}F_{\mu\nu}^a F_a^{\mu\nu} + \sum_{\alpha} \bar{\psi}^{(\alpha)} (i\not{D} - m^{(\alpha)}) \psi^{(\alpha)} \quad (2.7)$$

where the gluon field strength tensor is given by

$$F_{\mu\nu}^a = \partial_{\mu}G_{\nu}^a - \partial_{\nu}G_{\mu}^a - g_s f^{abc} G_{\mu}^b G_{\nu}^c \quad (2.8)$$

and the covariant derivative acting on the quark field is

$$D_{\mu}\psi = \left(\partial_{\mu} + \frac{i}{2}g_s\lambda_a G_{\mu}^a \right) \psi . \quad (2.9)$$

Equation 2.7 contains explicit mass terms for the quarks but none for the gluons.

The Lagrangian in equation 2.7 is locally $SU(3)$ gauge invariant. This property can be demonstrated by considering a general transformation of the fermion field

$$\psi' = \mathbf{U}(x)\psi \quad (2.10)$$

where $\mathbf{U}(x)$ is a unitary operator ($U^{\dagger} = U^{-1}$). All unitary operators can be written in terms of Hermitian matrices ($H^{\dagger} = H$),

$$\mathbf{U}(x) = \exp(i\mathbf{H}) . \quad (2.11)$$

For a 3×3 matrix, \mathbf{H} can be decomposed into a linear combination involving the unit and Gell-Mann matrices,

$$\mathbf{H} = \theta(x)\mathbf{I} + \frac{1}{2} \mathbf{a}(x) \cdot \boldsymbol{\lambda} \quad (2.12)$$

with $\theta(x)$ and $\mathbf{a}(x)$ real constants. The term $\theta(x)\mathbf{I}$ corresponds to a $U(1)$ phase rotation. Since $U(3) = U(1) \times SU(3)$, the $SU(3)$ components can be isolated and the transformation written as

$$\mathbf{U}(x) = \exp \left(\frac{i}{2} \mathbf{a}(x) \cdot \boldsymbol{\lambda} \right) . \quad (2.13)$$

Selecting the covariant derivative as in equation 2.9 and requiring that

$$(\mathbf{D}_\mu \psi)' = \mathbf{U}(x) (\mathbf{D}_\mu \psi) , \quad (2.14)$$

the gluon field component is found to transform as

$$(\lambda_a G_\mu^a)' = \mathbf{U}(x) [\lambda_a G_\mu^a] \mathbf{U}^{-1}(x) + 2 \frac{i}{g_s} \partial_\mu \mathbf{U}(x) \cdot \mathbf{U}^{-1}(x) . \quad (2.15)$$

The gluon field strength tensor is determined from

$$[\mathbf{D}_\mu, \mathbf{D}_\nu] \psi = i g_s \mathbf{F}_{\mu\nu} \psi \quad (2.16)$$

to be

$$\mathbf{F}_{\mu\nu} = \frac{\lambda_a}{2} \partial_\mu G_\nu^a - \frac{\lambda_a}{2} \partial_\nu G_\mu^a + \frac{i}{4} g_s [\lambda_a G_\mu^a, \lambda_b G_\nu^b] \quad (2.17)$$

with gauge transformation

$$\mathbf{F}'_{\mu\nu} = \mathbf{U}(x)\mathbf{F}_{\mu\nu}\mathbf{U}^{-1}(x) . \quad (2.18)$$

Applying

$$F_{\mu\nu}^a = \text{tr} \left[\frac{\lambda^a}{2} \mathbf{F}_{\mu\nu} \right] , \quad (2.19)$$

the gluon field strength tensor reproduces equation 2.8. Under the local $SU(3)$ gauge transformation of the fermion fields, the QCD Lagrangian remains invariant due to the commensurate transformations of the gluon fields.

The equations of motion are determined from equation 2.7 according to the Euler-Lagrange prescription,

$$\frac{\partial \mathcal{L}}{\partial \phi} - \partial_\mu \frac{\partial \mathcal{L}}{\partial (\partial_\mu \phi)} = 0 . \quad (2.20)$$

Replacing ϕ with $\psi^{(\alpha)}$ in equation 2.20 and employing the QCD Lagrangian, the equations of motion for the quark fields are determined to be

$$(i\not{D} - m^{(\alpha)}) \psi^{(\alpha)} = 0 . \quad (2.21)$$

Similarly, the equations of motion for the gluon fields are found by substituting G_μ^a for ϕ to obtain

$$D^\mu F_{\mu\nu}^a - \frac{g_s}{2} \sum_\alpha \bar{\psi}^{(\alpha)} \lambda_a \gamma_\nu \psi^{(\alpha)} = 0 . \quad (2.22)$$

The second term in equation 2.22 represents the current of the matter fields alone.

The QCD Lagrangian specifies the interactions of the quarks and leptons. Correlation functions in terms of functional integrals of actions utilizing the Lagrangian in equation 2.7 allow for the calculation of propagators and vertices. The Feynman diagrams describing the quarks and leptons and rules for their use are treated thoroughly in other texts (see, for example, reference [37]). The theoretical predictions of observable quantities from Feynman diagram calculations can be computed and compared to experimental results.

2.1.1 Asymptotic Freedom

The presence of divergent structures arising from higher order corrections to the first terms in a perturbative expansion of correlation functions produce effects which must be treated in order to calculate observable quantities. Renormalization of the theory removes the unphysical infinities arising from the computation of Feynman diagrams. Although the theory may incorporate infinite quantities, predictions of observable effects must be finite. Loop corrections to tree-level Feynman diagrams introduce an unknown momenta k of the virtual particles into the calculation for scattering amplitudes. The four momenta at each vertex is required to be conserved with an unrestricted momentum assigned to the loop. An integral expression in terms of $\int d^4k$ must be evaluated in order to sum over all possibilities of the unobservable momentum k . In typical one-loop corrections to a generic form for a propagator, factors involving

$$\sim \int \frac{d^4k}{(2\pi)^4} \frac{1}{(k-p)^2 + i\epsilon} \frac{\not{k} + m}{k^2 - m^2 + i\epsilon} \cdots \quad (2.23)$$

can exist with p the momentum for an incoming or outgoing particle and m the mass of a particle with momentum k . The $i\epsilon$ term reflects the choice of contour over which the integration will occur, removing the poles from the real axis. The integration path of k^0 is along the real axis with the poles approaching the real axis in the limit $\epsilon \rightarrow 0$. The naive definition of the coupling parameters found in association with equation 2.23 can be regarded as responsible for the infinities in the calculation of the loop diagrams. In a reparameterization of the coupling parameters to absorb the detractive effects, the bare coupling is redefined as a physical coupling and calculation of higher order loops leads to measurable effects.

Two methods are utilized to avoid the divergences associated with the Feynman diagram calculations. In Pauli-Villars regularization, a parameter with units of mass is incorporated into the propagator which is primarily responsible for the existence of the divergence in the evaluated scattering amplitude. This method allows one to evaluate the divergent integrals by effectively introducing a fictitious particle which has no physical meaning. All observable quantities described by the theoretical calculations must be independent of this parameter. Dimensional regularization provides a method to evaluate the divergent integrals in a more transparent and general fashion than the Pauli-Villars scheme. Instead of modifying the propagators, the dimensionality of the integral is altered. The dimensions of the integral are replaced with one time and $(d - 1)$ spatial dimensions mimicking the substitution

$$\int \frac{d^4 k}{(2\pi)^4} \rightarrow \int \frac{d^d k}{(2\pi)^d} .$$

The diagrams are computed as analytic functions of space-time dimension d . In the limit $d \rightarrow 4$, all observable predictions are required to behave in a non-pathological manner. Integrals involving terms such as $d^4k/(k^2 + m^2)^2$ will contain singularities at $d = 4$. These poles are absorbed into theory parameters at a scale μ where the divergences are removed.

Evaluation of scattering amplitudes using dimensional regularization often involves an approximation of the gamma function. With the definition $\epsilon = 4 - d$, a commonly found term in many calculations can be written to order ϵ as

$$\frac{\Gamma(2 - \frac{d}{2})}{(4\pi)^{d/2}} \left(\frac{1}{\varphi}\right)^{2 - \frac{d}{2}} = \frac{2}{\epsilon} + \ln(4\pi) - \gamma_E - \ln \varphi + \mathcal{O}(\epsilon) \quad (2.24)$$

where γ_E is the Euler-Mascheroni constant. The divergence in the scattering amplitude arising from the $d \rightarrow 4$ requirement is often eliminated by simply subtracting the divergent components. In minimal subtraction (MS), terms with $1/\epsilon$ poles are subtracted and an arbitrary logarithmic term added to create a renormalized equation with proper dimensions. The procedure of modified minimal subtraction ($\overline{\text{MS}}$) differs slightly from the MS technique by also absorbing the constant terms found in equation 2.24 into the effective coupling. Employing the $\overline{\text{MS}}$ prescription, the constant terms and the pole term are subtracted from equation 2.24 yielding to order ϵ

$$\frac{\Gamma(2 - \frac{d}{2})}{(4\pi)^{d/2}} \left(\frac{1}{\varphi}\right)^{2 - \frac{d}{2}} = -\ln\left(\frac{\varphi}{\mu}\right)$$

with μ an arbitrary parameter with the same units as φ .

The unrenormalized gluon propagator can be written in a general form as

$$D_{ab}^{\mu\nu} = \frac{\delta_{ab}}{iq^2} \left(g^{\mu\nu} - \frac{q^\mu q^\nu}{q^2} \right) f \left(\frac{q^2}{\chi^2}, \alpha(\xi^2) \right)$$

where f is a function containing the vacuum polarization tensor with logarithmic divergence. The renormalization of the function f removes the divergences through a redefinition of the coupling. Defining the running coupling constant with a parameter δ_f at a renormalization point λ to be

$$\alpha(\lambda^2) \equiv \delta_f \alpha(\xi^2) , \quad (2.25)$$

the function f can be written as

$$f \left(\frac{q^2}{\chi^2}, \alpha(\xi^2) \right) = \delta_f g \left(\frac{q^2}{\lambda^2}, \alpha(\lambda^2) \right)$$

with g a finite function. A dimensionless parameter β arising from the determination of the Callan-Symanzik equation is given by the Gell-Mann-Low equation

$$\beta(\alpha(\lambda^2)) = \frac{d\alpha(\lambda^2)}{d\ln(\lambda^2)} . \quad (2.26)$$

Recognizing that $\beta(\alpha)$ represents corrections at one loop and higher, a power series expansion with first term α^2 can be performed,

$$\beta(\alpha) = \alpha^2 (\beta_0 + \beta_1 \alpha + \mathcal{O}(\alpha^2)) . \quad (2.27)$$

Solving equation 2.26 using the expansion of β to lowest order in α and integrating from a momentum scale μ to q , the coupling constant is determined to be

$$\alpha(q^2) = \frac{\alpha(\mu^2)}{1 - \alpha(\mu^2)\beta_0 \ln\left(\frac{q^2}{\mu^2}\right)} . \quad (2.28)$$

The corresponding one loop corrections to the gluon propagator establish that

$$\beta_0 = -\frac{1}{12\pi} (33 - 2n_f) \quad (2.29)$$

where n_f is the number of flavors. Similarly, higher loop corrections produce [38]

$$\beta_1 = -\frac{1}{24\pi^2} (153 - 19n_f) .$$

The parameter β_0 is eliminated from equation 2.28 by using the results in equation 2.29 to find

$$\alpha(q^2) = \frac{\alpha(\mu^2)}{1 + (\alpha(\mu^2)/12\pi) (33 - 2n_f) \ln\left(\frac{q^2}{\mu^2}\right)} . \quad (2.30)$$

This equation provides an expression for the behavior of the coupling constant at different q^2 with respect to the momentum scale μ .

The value of μ utilized to define α was chosen essentially as an arbitrary parameter which supplied a renormalized coupling constant. In quantum electrodynamics (QED), the analogous coupling parameter is the electromagnetic fine structure

constant,

$$\alpha_{\text{em}}(q^2) = \frac{g_{\text{em}}^2}{4\pi} .$$

In the limit $q^2 \rightarrow 0$, the term g_{em}^2 gives the experimentally measured charge e^2 . Perturbation theory is applicable for such processes since $\alpha_{\text{em}} = 1/137$. Unfortunately, the same procedure cannot be performed for the QCD coupling constant. When $q^2 \rightarrow 0$, α increases violating the applicability of a perturbative expansion. To alleviate this condition, α was defined at the renormalization point $q^2 = \mu^2$ producing an effective coupling $\alpha(\mu^2)$. In the asymptotic limit, the physical quantities depend on q/μ . However, the parameter μ was selected for convenience, with alternate values equally acceptable. To eliminate the renormalization effects induced by μ , a mass scale Λ is defined,

$$\Lambda^2 \equiv \mu^2 \exp \left[\frac{-12\pi}{(33 - 2n_f)\alpha(\mu^2)} \right] . \quad (2.31)$$

In principle, Λ should be a measurable quantity which can be extracted from data. Substituting equation 2.31 into equation 2.30, the running coupling constant can be expressed in terms of a single unknown parameter,

$$\alpha(q^2) = \frac{12\pi}{(33 - 2n_f) \ln \left(\frac{q^2}{\Lambda^2} \right)} . \quad (2.32)$$

The parameter Λ can be envisioned as the scale separating the regions inhabited by quarks and gluons from those populated by baryons and mesons. In essence, Λ reveals the energy scale at which strong interactions dominate and confining

forces prevail. Experimental measurements limit Λ to a range of 100 to 300 MeV, with $\Lambda \approx 200$ MeV commonly quoted [22]. A value of $\Lambda \approx 200$ MeV suggests a confining region for the strong forces of approximately 1 fm. The applicability of a perturbative expansion in terms of weakly interacting quarks and gluons is governed by the strength of the coupling constant. A small coupling constant is obtained from equation 2.32 for $q^2 \gg \Lambda^2$.

Theories in which the coupling strength decreases with increasing momentum transfer scale are designated as asymptotically free. Asymptotic freedom pertains only to those renormalizable quantum gauge field theories in four spacetime dimensions which are non-Abelian [39]. QCD and its associated running coupling constant replicate this behavior. For $q^2 = 4 \text{ GeV}^2$ and 100 GeV^2 the values for α computed from equation 2.32 are approximately 0.32 and 0.19, respectively. In the limit $q^2 \rightarrow \infty$, α tends to zero. This effect can be interpreted as the converse of charge screening in electrodynamics. The QCD vacuum contains virtual $q\bar{q}$ pairs as well as virtual gluons. The virtual gluons overwhelm the contribution from the $q\bar{q}$ pairs enabling antiscreening to dominate. The color charge of an object is diffused due to the emission and absorption of virtual gluons. As the momentum of the particle used to probe the colored object increases, less of the color charge is observed reducing the strength of the coupling constant.

The strong forces are weak at small distances allowing application of perturbative approximations. Since QCD is an asymptotically free theory, Feynman diagrams can be reliably computed to give quantitative predictions about the interactions between quarks and gluons in the high q^2 regime. High momentum transfer collisions allow for the examination of individual quarks and antiquarks.

sea quarks and antiquarks, and gluons within hadrons. The predictions for high momentum collision events involving hadrons are obtained by assuming the hadron is a loose conglomerate of partons and the strength of the strong force increases with distance.

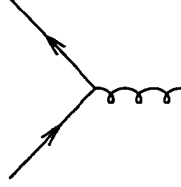


Figure 2.1: Feynman diagram for the tree level quark-gluon vertex.

An expansion in terms of Feynman diagrams assumes that the coupling constant is small. When the coupling strength grows, an increasing number of diagrams is necessary in order to accurately calculate the scattering amplitudes. The tree-level process of two quarks interacting with a gluon is shown in figure 2.1. The qqg vertex has the value $-ig_s T_{ij}^a \gamma^\mu$ with i and j indicating quark colors and a a gluon color states. Figure 2.2 shows the dominant production mechanisms for $q\bar{q}$ production at hadron colliders. The leading order terms contributing to the cross section are

$$q + \bar{q} \rightarrow q + \bar{q}$$

for the Feynman diagram to the left in figure 2.2 and

$$g + g \rightarrow q + \bar{q}$$

for the remaining diagrams. Of these processes, the dominant source for $q\bar{q}$ production at the Tevatron is gluon fusion. More complicated graphs can be written, but the complexity of the calculations rapidly increases.

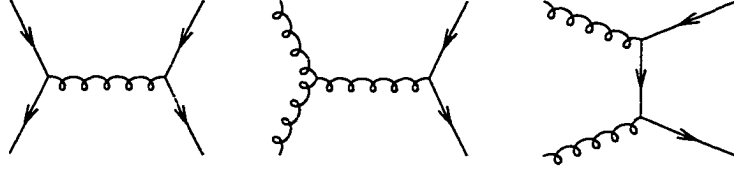


Figure 2.2: Feynman diagrams for tree level $q\bar{q}$ production from $q\bar{q}$ and gluon pairs.

2.1.2 Parton Densities

The inherently composite nature of hadrons allows for the constituents to have momenta which may differ greatly from that of the parent hadron. Calculations of cross sections for colliding hadrons in which the constituents interact must incorporate distribution functions describing the momenta of the partons. These parton distribution functions (PDFs) are included in theoretical predictions of hadron collisions where the partonic processes $qq \rightarrow qq$, $qg \rightarrow qg$, and $gg \rightarrow gg$ have occurred. Since they represent low energy scale behavior and therefore cannot be determined *a priori* from perturbative QCD, the PDFs must be parameterized and measured from experiment. Hadrons with large transverse momentum produced in proton anti-proton collision events provide a probe of quark and gluon scattering. The PDFs are more frequently determined from deep inelastic scattering in which a high energy photon interacts with a single quark. Both valence and sea quarks¹

¹The valence quarks are the quarks which are responsible for the spectroscopic characteristics of the hadron. Sea quarks represent the virtual $q\bar{q}$ particles which populate the vacuum.

participate in the photon interactions. For lower energy collisions with a charged hadron, the photon treats the hadron as a point particle and is described by Mott scattering.

The differential scattering cross sections for various hadronic targets are measured and theoretical arguments regarding isospin symmetry employed to extract information about individual structure functions. The unknown dynamics are parameterized by the structure functions F_1 and F_2 in a differential cross section formula akin to that found for Rutherford scattering. To lowest order in α , the structure functions exhibit Bjorken scaling in which F_1 and F_2 are described by

$$x \equiv -\frac{q^2}{2q \cdot p}$$

alone, where p is the momentum of the parent hadron. The parton model of hadrons allows the measured structure functions $F_i(x, q^2)$ to be related to the parton distribution functions $f_i^h(x, q^2)$. The PDF $f_i^h(x, q^2)$ represents the probability that the parton of flavor i in the hadron of type h carries a fraction x of the hadron's momentum when the parton is probed by a particle at scale q^2 . In terms of Bjorken scaled parameters which eliminate any q^2 dependence, the probability is $dP_i = f_i^h(x)dx$. The general tendency of the distribution functions is for the value to be large at small x , and, conversely, small at large x . The momentum weighted PDF, $xf_i^h(x, q^2)$, is normalized by

$$\sum_i \int_0^1 dx x f_i^h(x, q^2) = 1$$

where the sum i is over all partons.

The Altarelli-Parisi equations are used to extend a parton distribution function determined at a specific value of q^2 to other momentum scales. The inelastic structure functions obey Bjorken scaling at very high energies in that they are only dependent on x and do not include q^2 . The PDFs pertaining to quarks of flavor i are written as q_i . The parton distribution functions are arranged into non-singlet quark distributions

$$f^{ns} \equiv f_i - f_j ,$$

singlet quark distributions

$$f^s \equiv \sum_i (f_i + \bar{f}_i) ,$$

and gluon distributions g . These redefinitions lead to a more tractable analysis of the Altarelli-Parisi equations providing useful cancelations and separation of coupled differential equations. The singlet quark and gluon distributions can be combined in the column matrix

$$\mathbf{f} \equiv \begin{pmatrix} f^s \\ g \end{pmatrix} .$$

Momentum dependence is introduced through the evolution equations which will produce a violation of Bjorken scaling. The PDFs become functions of both x and

q^2 . The Altarelli-Parisi equation for the non-singlet quark distribution is

$$q^2 \frac{\partial f^{ns}}{\partial q^2} = \frac{\alpha(q^2)}{2\pi} P_{q \rightarrow qg} * f^{ns} . \quad (2.33)$$

For the singlet quark and gluon distributions, the Altarelli-Parisi equations are

$$q^2 \frac{\partial \mathbf{f}}{\partial q^2} = \frac{\alpha(q^2)}{2\pi} \begin{pmatrix} P_{q \rightarrow qg} & 2n_f P_{g \rightarrow q\bar{q}} \\ P_{q \rightarrow gq} & P_{g \rightarrow gg} \end{pmatrix} * \mathbf{f} . \quad (2.34)$$

Both equation 2.33 and 2.34 contain convolution integrals defined by

$$f * g \equiv \int_x^1 \frac{dy}{y} f(y) g\left(\frac{x}{y}\right) .$$

The parton distribution functions are extended by the Altarelli-Parisi equations over a broad range of momentum scales up to order α corrections that are not enhanced by large logarithms. The evolution equations 2.33 and 2.34 are governed by the splitting functions $P_{q \rightarrow qg}$, $P_{q \rightarrow gq}$, $P_{g \rightarrow q\bar{q}}$, and $P_{g \rightarrow gg}$.

The splitting functions indicate the probability that a parton has been altered either by radiation or pair creation of other partons. For a quark which radiated a gluon to retain a fraction z of its original momentum, the probability is intimated in the expression for $P_{q \rightarrow qg}$ written as

$$P_{q \rightarrow qg}(z) = \frac{4}{3} \left[\frac{1+z^2}{(1-z)_+} \right] + 2\delta(1-z) . \quad (2.35)$$

To represent the probability that the radiated gluon carries momentum fraction z , $P_{q \rightarrow gq}$ is determined by $P_{q \rightarrow gq}(z) = P_{q \rightarrow qg}(1 - z)$ to find

$$P_{q \rightarrow gq}(z) = \frac{4}{3} \left[\frac{1 + (1 - z)^2}{z} \right]. \quad (2.36)$$

The probability for a gluon decaying into a quark with momentum fraction z and an antiquark with fraction $1 - z$ is deduced from

$$P_{g \rightarrow q\bar{q}}(z) = \frac{1}{2} [z^2 + (1 - z)^2]. \quad (2.37)$$

Since QCD contains gauge particles capable of self interaction, a gluon can decay into two gluons. The occurrence of a gluon producing additional gluons transpires with a probability related to

$$P_{g \rightarrow gg}(z) = 6 \left[\frac{1 - z}{z} + z(1 - z) + \frac{z}{(1 - z)_+} \right] + \left(\frac{11}{2} - \frac{n_f}{3} \right) \delta(1 - z). \quad (2.38)$$

The $+$ function in equations 2.35 and 2.38 is defined as

$$\frac{1}{(1 - z)_+} \equiv \lim_{\beta \rightarrow 0} \left[\frac{1}{1 - z} \theta(1 - z - \beta) + \ln \beta \delta(1 - z - \beta) \right] \quad (2.39)$$

where θ is the Heaviside step function.² The singularity at $z = 1$ arises from the infrared divergence identified with soft gluon emission. Equations 2.35 and 2.36 suggest that quarks with high momentum fractions will lose energy predominantly by radiating gluons.

²For $z \leq 0$, $\theta(z) = 0$ and for $z > 0$, $\theta(z) = 1$.

The products of hadron collisions observed by particle detectors originate from soft and hard scattering events. Low momentum interactions primarily via a plethora of virtual gluons among the constituents of the hadrons characterize soft events.³ The associated large strong couplings indicate that predictions for such processes cannot be calculated from perturbative QCD. Occasionally, hard scattering events occur in which two quarks or gluons interact and exchange large momentum to produce large momenta resultant particles. The hard scattering cross section for the collision of a hadron h with its antiparticle both with momentum p is constructed from the subprocess cross section and the parton distribution functions. A collision involving the direct interaction of partons producing the hadronic final state Y in conjunction with any hadrons X can be written as

$$\sigma(h(p) + \bar{h}(p) \rightarrow Y + X) = \sum_a \int_0^1 dx_1 dx_2 f_a(x_1) f_{\bar{a}}(x_2) \cdot \hat{\sigma}(a(x_1 p) + \bar{a}(x_2 p) \rightarrow Y) \quad (2.40)$$

with a representing the species of quarks, antiquarks, and gluons. QCD perturbation theory is employed to calculate the cross section for the partonic process represented by $\hat{\sigma}$. The functional dependencies of $\hat{\sigma}$ are

$$\hat{\sigma} = \hat{\sigma}(x_1 p, x_2 p, p_Y, m_Y, \Lambda) \quad (2.41)$$

³In a strict sense, the use of Feynman diagrammatics is no longer valid. Visualizing the interactions as complicated structures of gluon emission and absorption does serve as a helpful tool, but should not be considered too seriously.

where p_Y and m_Y are the momentum and mass of Y , respectively. The cross section to produce X from a proton anti-proton collision is determined from the convolution of $\hat{\sigma}$ with the distribution functions.

The distribution functions are determined by comparing equations derived to specific orders in α with experimental observations. The functional form of the distributions are provided by calculations performed to leading and next-to-leading order. The PDFs are created in an iterative process with initial conditions set experimentally. Measurements of the deep inelastic scattering cross section at a specific value of q^2 are often utilized to determine the distribution. Once constructed for all x at a value of q^2 , the structure functions are evolved to different momentum transfer scales according to the Altarelli-Parisi equations. The resultant PDF is then used as the seed to generate the next PDF. Repeated cycles of this procedure produce PDFs with q^2 dependence applicable in a broad range of calculations. The parton distribution functions constructed by various groups since the late 1970s have been collected and tabulated in a software library available from the CERN laboratory [40].

2.1.3 QCD Questions

While QCD is a sophisticated and useful theory capable of accurately predicting experimental observations, several puzzling, if not troubling, fundamental issues remain in a complete description of the hadronic event structures. Most collisions which produce hadrons in the final state involve both high and low energy aspects. Typically, the two regimes are separated and treated independently. For the high energy portion, the value of the coupling is sufficiently small allowing a pertur-

bative expansion to be performed and the machinery of QCD is applicable. The behavior of the coupling constant in equation 2.32 when the energy approaches order Λ demonstrates an increasing strong force which invalidates the analysis of the dynamics in terms of an expansion about the coupling. The process of binding the partons carrying color into color neutral particles called hadronization is exactly a low energy phenomena. The non-perturbative parts of a collision event are typically parameterized, duplicated from experimental data, or described by a phenomenological model to characterize the low q^2 effects.

Comparisons between predictions from QCD and observations often do not verify that perturbation theory in QCD is an accurate description of fundamental interactions in collision events. Instead of an examination of the theory, the ingenuity used to parameterize the non-perturbative effects is frequently tested in such comparisons. The dependence of the theoretical predictions on the incalculable component can be determined only by carefully isolating the sensitivities of various contributions. The ability of QCD to correctly describe the approximate behavior of a large number of experiments engenders the conviction that the interactions among quarks and gluons are properly represented.

2.2 Hadron Collisions

The asymptotic freedom of quantum chromodynamics (QCD) allows the usual calculational techniques of perturbative expansions in terms of Feynman diagrams when in a regime of large Q^2 (small distances). Unfortunately, $p\bar{p}$ collider events necessarily involve both low and high Q^2 behavior. As perturbative methods are no longer valid for low Q^2 , the long-distance non-perturbative features are parame-

terized either directly from data or through the use of a model. QCD Monte-Carlo generators, which consist of perturbative QCD calculations and phenomenology and model building, are used to simulate high energy particle collisions. These simulations attain their legitimacy through detailed comparison with a wide variety of data.

At the Tevatron, the majority of $p\bar{p}$ collisions produce particles at all values of rapidity with low transverse momentum. Occasionally a “hard” scattering event occurs characterized by outgoing hadrons with large transverse momentum which originate from large transverse momentum partons, as illustrated in Figure 2.3. In addition, hard scattering events will contain contributions from the breakup of the proton and antiproton constituting the “beam-beam remnants”. Interactions between more than one pair of partons may occur in multiple parton scattering as shown in Figure 2.4. The underlying event structure contains the fragments of the original $p\bar{p}$ system, hadrons arising from initial state gluon radiation, and possibly hadrons resulting from multiple parton scattering.

The composition of large transverse momentum Z boson events is displayed in Figure 2.5. In addition to the Z boson, the event contains large transverse momentum outgoing particles that originate from the “away-side” parton (eventually becoming the away-side jet) and beam-beam remnants. As in the dijet case, the underlying event consists of beam-beam remnants, initial-state radiation, and possibly multiple parton interactions. Naively, one would expect the underlying event to be roughly the same for dijet and Z boson production. However, the Z boson is a color singlet, while in dijet production the outgoing partons are $SU(3)_c$ objects, resulting in a different color separation between the two processes. Con-

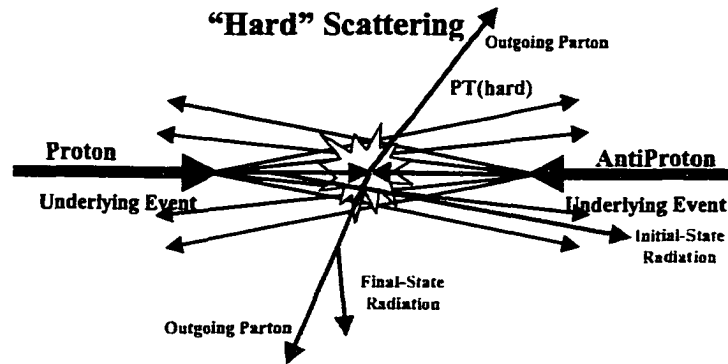


Figure 2.3: Illustration of a $p\bar{p}$ collision in which a “hard” 2-to-2 parton scattering with transverse momentum, p_T^{hard} , has occurred. The resulting “dijet” event contains particles that originate from the two outgoing partons (plus final-state radiation) and particles that come from the breakup of the proton and antiproton (i.e. “beam-beam remnants”).

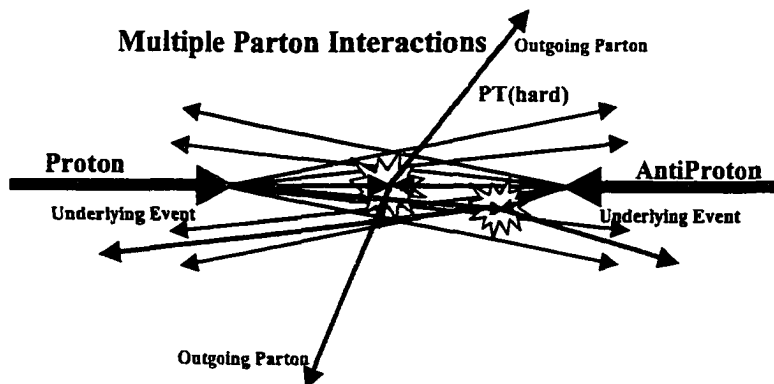


Figure 2.4: Illustration of a $p\bar{p}$ collision in which multiple parton interactions have occurred. In addition to the “hard” 2-to-2 parton scattering with transverse momentum p_T^{hard} , there is an additional “semi-hard” parton-parton scattering that contributes particles to the underlying event. For PYTHIA, we include the contributions from multiple parton scattering in the beam-beam remnant component.

sequently, these “color string” effects may produce differences in the underlying event structure.

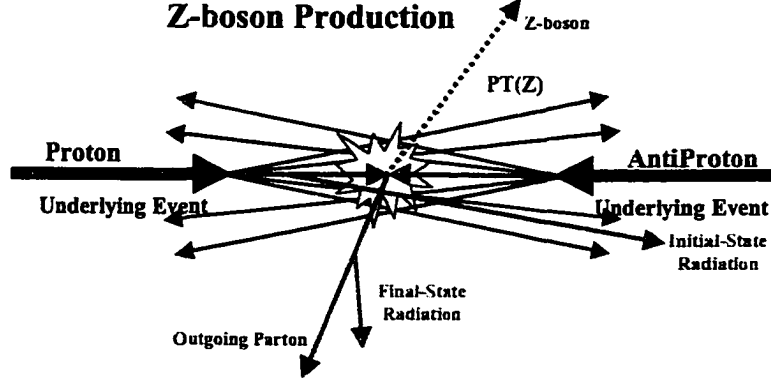


Figure 2.5: Illustration of a $p\bar{p}$ collision in which a Z boson with large transverse momentum, $p_T(Z)$, has been produced. The resulting event contains particles that originate from the “away-side” outgoing parton (plus final-state radiation) and particles that come from the breakup of the proton and antiproton (i.e. “beam-beam remnants”).

The reliance on effective phenomenological models due to the limited theoretical understanding of the underlying event necessitates a detailed examination of its behavior. The underlying event is typically treated as an unwelcome background in most analyses, an unfortunate consequence of colliding composite particles such as hadrons. Since the center of mass energies and interaction rates per beam crossing increase at Run II of the Tevatron and the Large Hadron Collider (LHC), the contribution of the underlying event to all analyses gains in significance. Accurate predictions of various backgrounds to a particular process are vital if new physics is to be discovered.

In the present analysis, the high energy and luminosity attained by the Collider Detector at Fermilab (CDF) during Run I is exploited to investigate the underlying

event. To facilitate optimization of the models used to predict the results of particle collisions, the behavior of the underlying event is examined and documented. The overall event structure of dijet, Z boson, and J/ψ from B decay events is examined with emphasis on observations of the underlying event. For the dijet data, the underlying event is isolated by employing the techniques of a recent CDF analysis [41] in which azimuthal regions are defined with respect to the leading charged jet. Similarly, events containing Z bosons are probed as a function of the transverse momentum of the Z by creating azimuthal regions about the Z direction in order to observe the behavior of the underlying event [42]. The transverse momentum direction of both the leading charged jet and the J/ψ can be utilized to study the underlying event in the J/ψ from B decay data [43]. While the motivation is to characterize the underlying event, it is hoped that this analysis can provide insight into non-perturbative QCD processes which may aid further theoretical developments.

2.3 Modeling Collision Events

2.3.1 Monte-Carlo Models

Numerical evaluation and prediction of collision events at particle accelerators are performed by Monte-Carlo (MC) generators. The characteristics of the calculated particles with explicit momentum distributions can be compared to experimental data. In an overly simplistic view of the methodology, MC generators segregate an event into two regimes according to momentum scale. For large q^2 , the QCD coupling constant given in equation 2.32 is small. A perturbative expan-

sion in terms of Feynman diagrams can be performed and scattering amplitudes determined for hard scattering collisions. In the low q^2 regime, the large coupling constant invalidates the use of perturbation theory. Instead, phenomenological models involving many parameters which are tuned from data are employed.

The standard treatment of hard scattering events in theoretical models combines perturbative and non-perturbative domains by assuming a superposition of a parton-parton hard interaction and a soft collision. The differential cross section for the process calculated from amplitudes obtained using Feynman diagrams diverges when the transverse momentum of the hard scattering among the partons, p_T^{hard} , approaches zero. To insure that perturbative QCD is applicable, the hard transverse momentum is required to satisfy $p_T^{hard} \geq 3 \text{ GeV}/c$ for all simulations performed in this analysis. Showering processes are typically produced in MC generators by evolving the partons down to their mass shell through the radiation of additional partons. A tree-like structure is formed from the successive branchings of one parton to two partons. The differential probability describing a parton i branching to partons j and k is given by

$$\frac{d\mathcal{P}_a}{dt} = \mathcal{K}(t) \exp \left(- \int^t dt' \mathcal{K}(t') \right) \quad (2.42)$$

where

$$\mathcal{K}(t) = \frac{\alpha}{2\pi} \sum_{j,k} \int_{z_-(t)}^{z_+(t)} dz P_{i \rightarrow jk}(z) \quad (2.43)$$

and $t = \ln(q^2/\Lambda^2)$. The term $P_{i \rightarrow jk}$ represents the splitting functions described in equations 2.35, 2.36, 2.37, and 2.38. Equation 2.42 contains the Sudakov form

factor [44],

$$S(t) = \exp \left(- \int^t dt' \mathcal{K}(t') \right) . \quad (2.44)$$

The naïve probability for a parton to decay is properly normalized by the Sudakov form factor. The resulting branching distributions described by equation 2.42 provide a probabilistic interpretation suitable for MC simulation. As the partons branch, the value of t decreases for successive stages. When t is less than a perturbative cutoff, q_0^2 , the branching ceases. The strong forces between the colored partons increase and eventually reach a scale at which the partons are confined into color singlet hadrons. The non-perturbative process of parton to hadron conversion is described by models specific to the MC generator employed. Fragmentation refers to this transformation. Generally, a fragmentation function $D_h^i(z)$ representing the probability that a hadron h with momentum fraction z appears in conjunction with a parton i is associated with each parton. The beam-beam remnants produced from the dissolution of the collided hadrons typically describe interactions which are distinctly soft. Each MC generator employs different models to simulate the beam-beam remnants.

Many important details specific to the MC generators themselves produce significant effects which can be isolated and analyzed. Comparing with the general behavior observed in experimental data, the theoretical components predict certain event characteristics which can be verified. Of the several MC software packages available, the three most widely utilized general purpose event generators are selected for investigating high energy hadronic processes. The intention of the fol-

lowing sections which describe the MC generators is to explain differences among the various theoretical models. Unabridged accounts of the simulation mechanisms can be found in the manuals for HERWIG [45, 46], ISAJET [47], and PYTHIA [44, 48].

2.3.1.1 HERWIG

The distinctive attributes of the theoretical model employed by HERWIG are a cluster parameterization from which hadrons form and an angle ordering requirement for the parton shower. The hadronization scheme is local in color and independent of both the specific hard process and the energy. This allows the structure established in the parton shower to be largely reproduced in the event. The effects of soft gluon emission suggest that the partons in a shower should be ordered according to angle. Since several versions of HERWIG exist each with slight alterations, the predictions for the event may change. For a consistent analysis, this work uses HERWIG 5.9.

Hard scattering events are simulated by HERWIG in the three progressive stages of elementary parton interactions, initial and final state parton showering, and hadronization. The QCD $2 \rightarrow 2$ hard parton scattering subprocess is implemented to generate theoretical predictions which will be compared to data. The momentum transfer scale q^2 and the color flow assigned to the subprocess determine the boundary conditions used for the generation of initial and final state parton showers. The parton shower evolution is performed to leading-log order

using the parton energy fraction z and an angular variable, ξ , defined as

$$\xi_{jk} \equiv \frac{p_j \cdot p_k}{E_j E_k}$$

where j and k are the daughter partons of i . The momentum fractions z are selected according to equations 2.35, 2.36, 2.37, and 2.38. The Sudakov form factors determine the distribution for the angular variables ξ . The parton showers are terminated when the momentum transfer of the parton reaches a cutoff $Q_i = m_i + Q_0$ where $i = 1$ to 6 representing quark flavors and Q_0 is a hadronization scale. A cluster model is used by HERWIG to transform the partons into hadrons.

The underlying event is simulated by separating the hard scattering component from the remainder of the partons in colliding hadrons. Beam clusters are formed from those partons which did not undergo a hard scattering. The two beam clusters interact via a soft collision producing the underlying event. The model used to generate the underlying event is from a minimum-bias generator used by the UA5 Collaboration [49] and modified to incorporate the cluster hadronization scheme.

A cluster model derived from non-perturbative gluon splitting is used by HERWIG for all soft events. When the parton shower process is terminated, the concept of preconfinement in perturbative QCD [50, 51, 52] is invoked to create color-neutral clusters [53]. The gluons are forcibly decayed to $q\bar{q}$ pairs in a non-perturbative process. All particles at this stage consist of either quarks or antiquarks. Color singlet clusters are created by connecting color lines from final state quarks to antiquarks. The clusters undergo hadronization and observable particles are produced. This procedure can be illustrated for the basic situation

when a cluster is composed of two quarks q_1 and q_2 . A quark q and antiquark \bar{q} pair of the first four flavors are randomly generated. The cluster is hadronized by matching the components with the generated fermions such that color singlet particles $q_1 q$ and $q_2 \bar{q}$ are created. A low energy cluster unable to create two hadrons is enhanced by interacting with a neighboring cluster through the exchange of transverse momentum after which the decay is possible.

Within the showering process, the partons are required to satisfy an angle ordering criteria. The coherence of soft gluon emission affects the subsequent decays by constraining the opening angle between the daughters [54]. At each successive vertex in the shower signifying a branching, the opening angle decreases. Angle ordering is a consequence of the interference among soft gluons. The Sudakov form factor given in equation 2.44 describing the sum of virtual corrections and unresolved real emissions determine the distributions for the emission angles.

2.3.1.2 ISAJET

Hadronization by independent fragmentation and simulation of the underlying event by a modified cut pomeron model are two features differentiating ISAJET from most other MC generators. Independent fragmentation allows various predicted characteristics to be investigated since the process in which the hadrons are created preserves the information of the partonic source. Unlike HERWIG, ISAJET does not constrain the partons within a shower to obey an angle ordering requirement. Standardizing on one version, ISAJET 7.32 was consistently used for this study.

ISAJET generates hard scattering events in four stages. The elementary parton interactions which produce the hard scattering are calculated using perturbative QCD. The subprocess cross sections are derived from theory and therefore only the order in α to which the scattering amplitudes are calculated can differ. Following the hard scattering, the partons are allowed to radiate in both the initial and final states. As in HERWIG, the successive decays are described by a leading-log approximation and form a tree-like topology. Once the energy of the partons is degraded to a level specified by a predetermined cutoff, the partons are converted into hadrons using an independent fragmentation model. If they have lifetimes less than 10^{-12} seconds, the generated hadrons are forced to decay. In the last step of simulation, the underlying event is calculated using a cut pomeron approach from the beam remnants and consolidated with the rest of the event.

The underlying event is created from the same model used to generate soft minimum bias events with parameters selected to reproduce behavior observed in data. Generators where hadronization occurs strictly via production of quark and antiquark pairs from the vacuum under the action of strong forces predict short range rapidity correlations and approximately Poisson distributed multiplicity fluctuations. Since experimental data suggests long range rapidity correlations are present, particles mediating interactions in a non-perturbative QCD scale are utilized by ISAJET to explain this behavior. A modified theory of cut pomerons developed by Abramowskii, Kanchelli, and Gribov is employed for both underlying event and soft minimum bias predictions in ISAJET [55]. Unitarity conditions imposed on the basic theory lead to a model in which K cut Pomerons exist.

Pomerons describe color singlet objects which are exchanged between particles in a non-perturbative regime. The concept of pomeron originated in Regge theory before the establishment of QCD [56]. With the advent of QCD, the exchange of soft pomerons between partons was generally considered to describe the non-perturbative interaction of multiple gluons and partons. Coupling between quarks and pomerons should not be point-like. The large distance behavior of the strong force is non-perturbative and can be parameterized by a phenomenological model incorporating the exchange of pomerons. ISAJET uses pomerons to explain the long range correlations observed in minimum bias data. The multiplicity distribution of cut pomerons is created by fitting to data. The distribution for minimum bias event generation is

$$\mathfrak{N}^P(K) = (1 + 4K^2) e^{-1.8K} .$$

In hard scattering events, the associations

$$\mathfrak{N}^P(1) \rightarrow 0.1\mathfrak{N}^P(1) ,$$

$$\mathfrak{N}^P(2) \rightarrow 0.2\mathfrak{N}^P(2) , \text{ and}$$

$$\mathfrak{N}^P(3) \rightarrow 0.5\mathfrak{N}^P(3)$$

are utilized by ISAJET.

The fragmentation model employed by ISAJET is similar in philosophy to that used by Field and Feynman to hadronize quarks and gluons via a parameterization which treats the partons independently [57]. A gluon undergoing fragmentation in ISAJET is regarded as a randomly selected u , d , or s quark or antiquark. The

process begins by selecting a quark q_1 to be hadronized and generating a quark q and antiquark \bar{q} with the probability of a particular flavor distributed in the proportions

$$u : d : s = 0.43 : 0.43 : 0.14 .$$

A meson with mean transverse momentum $\langle p_T \rangle = 0.35$ GeV/c is created from the composition $q_1 \bar{q}$. Production of baryons occurs by substituting a diquark qq' for the generated quark. Diquarks rarely appear since they are suppressed by a low creation probability and are not permitted to exist in the proximity of other diquarks eliminating the possibility that this mechanism forms exotic matter. Hadronization of the cut pomeron occurs in the pomeron's center-of-mass frame through a modification to independent fragmentation in which the splitting function is dependent on the energy. While independent fragmentation provides several accurate predictions for behavior observed in collision events, the occurrence of energy and flavor non-conservation is disconcerting. This issue is remedied by imposing energy conservation once the event has been generated. Individual hadrons are modified and the energies of all event constituents is recalculated. Those hadrons found to have negative momentum are discarded.

The independent fragmentation of partons allows the generated hadrons to be identified with specific partons from the showering process. The origins of the observable quantities within the model used by ISAJET can be isolated and studied. Hadron production within ISAJET is categorized according to three potential sources,

1. beam beam remnants,
2. initial state radiation, and
3. outgoing hard scattering jets including final state radiation.

While experimentally these divisions cannot easily, if at all, be distinguished, the origin of hadrons within the model can be examined to determine the effect of particular mechanisms on the theoretical predications which are compared to data.

2.3.1.3 PYTHIA

The procedure employed to hadronize the partons and the inclusion of multiple parton interactions are unique to PYTHIA. PYTHIA incorporates the Lund string model in the fragmentation scheme of partons [58]. The possibility of more than one scattering between the constituents of two colliding hadrons is accounted for by allowing several parton interactions. The specific versions of PYTHIA used for this study are PYTHIA 6.115 and 6.125.

The generation of a hard scattering event by PYTHIA utilizes a similar model as that found in HERWIG. The hard scattering event is calculated from analytic evaluation of Feynman diagrams representing a perturbative QCD expansion. Partons in the initial and final state are allowed to form cascades in which individual partons branch into two partons described by a leading-log order approximation of the shower evolution. Corrections to parton showering produce coherence effects which suggest that the emission angles in a shower should decrease for subsequent decays. Instead of HERWIG's cluster formation, PYTHIA employs color strings

to convert the partons into hadrons. The treatment of the underlying event which is superposed on the hard scattering also presents certain novel nuances.

The underlying event is constructed according to a model in which the colliding hadrons directly produce the generated structure. Beam remnants originate from the constituents of the colliding hadrons that did not undergo a hard scattering. Initial state radiation from the beam remnants is suppressed. While color connected to the hard interaction, the beam remnants are unaffected by the detailed characteristics of the hard scattering processes.

Several partons within the colliding hadrons may interact prompting multiple parton scattering to occur. All MC generators should consider the non-negligible possibility that several interactions transpire during one event. PYTHIA includes a method for multiple parton scattering which increases the activity of the underlying event. The interactions are generated as separate $2 \rightarrow 2$ scatterings where the initiating partons are from the colliding hadrons.

Fragmentation of partons into hadrons primarily occurs in PYTHIA using a color string model. Color strings can be envisioned as connections between two partons of the same color with an associated tension. As the tension increases, the string may break and additional partons form at the new ends of the strings. The simplified system of two quarks q_1 and q_2 connected by a color string demonstrates the mechanism of hadronization. When q_1 and q_2 move apart, the string becomes increasingly stretched. The string will eventually break under these conditions and produce a q and \bar{q} . The newly created quarks can combine with the original quarks to form color singlet mesons $q_1\bar{q}$ and q_2q . Baryons are formed in a similar manner by replacing the q and \bar{q} with diquark and antidiquark. Since gluons are color

octet particles, two color strings are attached to the gluon. The strings connecting the gluon break along their length forming $q\bar{q}$ pairs. Fragmentation ceases when the energy of the partons is reduced to a specified cutoff.

Unlike ISAJET, the initial state radiation source cannot be separated from the final state radiation source in PYTHIA. PYTHIA also includes multiple parton interactions which cannot be identified with the production of particular hadrons in the final state. Since the determination of events to contain hard scattering collisions does not allow for the ability to discern the number of interactions which occurred, the multiple parton interaction component is included in the beam beam category. The predictions from PYTHIA for the simulation of hadron collisions can be separated into particles arising from

1. beam beam remnants including multiple parton scattering and
2. outgoing hard scattering jets including initial and final state radiation.

CHAPTER 3 THE TEVATRON AND CDF

The capabilities of the Tevatron enable the production of proton antiproton collisions with the world's highest particle accelerator energies. For the experiments performed between 1992 and 1995 known as Run 1, the typical center of mass energy, \sqrt{s} , attained was 1.8 TeV. Significant improvements made to the accelerator complex since 1995 will extend the energy horizon to 2 TeV when Run 2 begins operation in March 2001. Until 200 n (where n has a nominal value of 6 but a potential value as high as 9), when the Large Hadron Collider (LHC) begins operation, the Tevatron will continue to be the highest energy particle accelerator.

The Collider Detector at Fermilab (CDF) records the characteristics of the particles produced from the proton antiproton collisions. CDF is composed of many elements designed to precisely measure a particle's position, momentum, and energy. Instead of a highly specialized detector, CDF has a broad capability allowing the data to be used for a large number of different studies. Concurrent with the Tevatron enhancements, the detector was upgraded for Run 2.

The high energy and luminosity provided by the Tevatron and recorded by CDF are exploited to investigate the event structure of hard scattering collisions at 1.8 TeV. This environment offers the unique opportunity to examine the underlying event for a wide range of parameters. The following sections describe the various accelerators used to achieve collisions at $\sqrt{s} = 1.8$ TeV and the detector components of CDF.

3.1 The Fermilab Accelerators

The high energy proton antiproton interactions achieved at Fermilab are the result of several accelerators working in conjunction. While the Tevatron is responsible for the final beam energies, six other accelerators are employed to supply the Tevatron with protons and antiprotons of the appropriate characteristics. These accelerators include the Cockroft-Walton generator, the Linac (linear accelerator), the Booster, the Main Ring, the Debuncher, and the Accumulator. All seven accelerators are necessary for the production of collisions at $\sqrt{s} = 1.8$ TeV [59, 60]. The layout of Fermilab is shown in figure 3.1.

Except for the Cockroft-Walton and the Linac, the accelerators used are synchrotrons. Synchrotrons accelerate charged particles by employing radio frequency (RF) cavities. Dipole magnets provide a confining force to constrain the charged particles to a circular path of constant radius. The radius is maintained by manipulating the strength of the dipole magnets' fields as the particle's momentum changes. The momentum to which a particle is accelerated in a synchrotron is limited by the strength of the dipole magnet and the oscillations of the RF cavity. In general, the particle momentum, p , which an accelerator can produce is related to the magnetic field strength, B , by [61]

$$p = 0.3Br , \tag{3.1}$$

where r is the synchrotron's radius.

The world's highest energy collisions have a humble origin as hydrogen gas stored in a steel container. Inside the Cockroft-Walton generator, the neutral

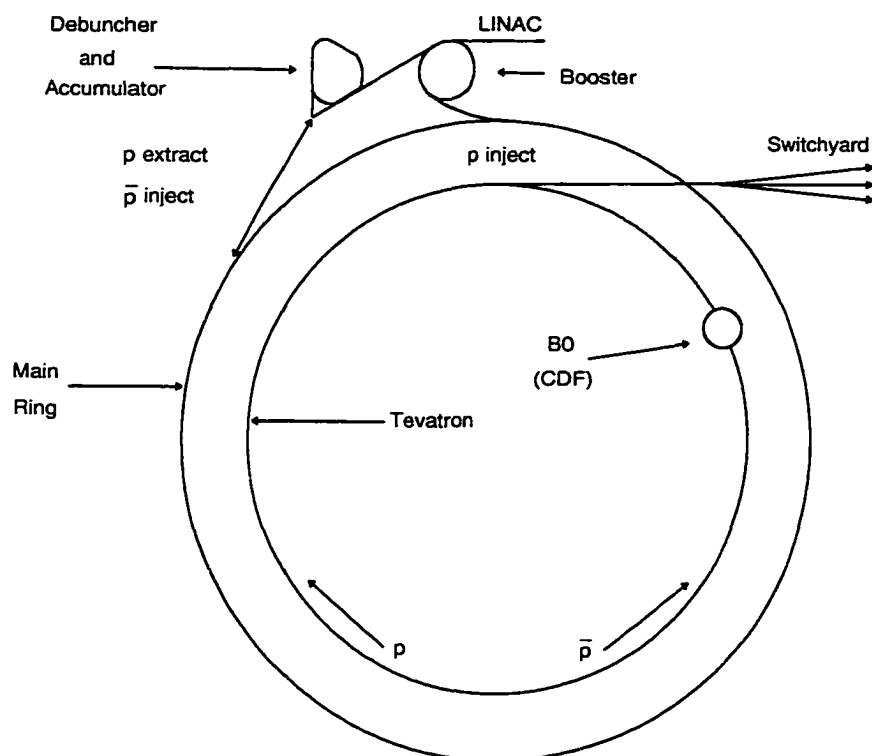


Figure 3.1: The ensemble of accelerators used for Run I of the Tevatron. The experiment begins in the Cockcroft-Walton generator (not shown in the figure) located before the linear accelerator. The Main Ring and Tevatron physically share the same tunnel.

hydrogen is converted into hydrogen ions. The dome of the generator is charged to -750 kV. The hydrogen ions are attracted towards electrical ground, passing through an electrostatic accelerating column. The average energy of the hydrogen ions at the end of the column is 750 keV. A transport line then injects the hydrogen ions into the Linac. This phase of beam preparation is often referred to as the pre-accelerator (preacc) stage.

The Linac is a 150 meter long linear accelerator. A metal drift tube attached to either side of a RF cavity constitutes the fundamental component. The beam energy produced by the Linac is primarily dependent on the voltage across each RF cavity and the accelerator length. In order to accelerate the negatively charged hydrogen ions to 200 MeV, 14 RF cavities are employed. While indiscriminately accepting all ions from the preacc, the Linac utilizes only those within a certain time period. The Linac in conjunction with the Cockroft-Walton can accelerate a beam of hydrogen ions once every 66 msec. A detailed description of the Cockroft-Walton and Linac can be found elsewhere [62].

Once the electrons of the hydrogen ions are removed by focusing the Linac's beam onto a carbon foil, the resulting protons are accelerated by the Booster. If present, hydrogen ions or atoms are directed to a dump in order to eliminate non-proton beam constituents. The Booster is a fast cycling synchrotron with a radius of 75.5 meters and 17 RF cavities. To fill the Booster, 3×10^{12} protons are required. When filled, the RF cavities are adjusted to accelerate the protons to 8 GeV. As with the previous stages, the Booster can accelerate a beam every 66 msec. Cycling twelve times in succession, the Booster can deliver twelve proton bunches to the Main Ring.

The Main Ring is a circular synchrotron with a 1 km radius. It is composed of 774 dipole and 240 quadrupole magnets to steer and focus the beam, respectively. There are 18 accelerating cavities which are employed to either accelerate the protons to 120 or 150 GeV. These two energies correspond to different modes of operation. The 120 GeV protons are sent to the antiproton source, where they collide with various targets in order to produce antiprotons for later use. The 150 GeV protons are injected into the Tevatron. The Main Ring can accelerate a beam every 2.4 sec.

The Tevatron accelerates the 150 GeV protons from the Main Ring to 900 GeV. It is a circular synchrotron located directly below the Main Ring and occupying the same tunnel. Since both accelerators have the same radius yet the Tevatron achieves higher energies, equation 3.1 mandates that the magnetic field of the dipoles must be greater. To attain the necessary field strengths, the Tevatron employs superconducting dipole magnets which provide a 4.4 Tesla magnetic field. Acceleration occurs through 8 RF cavities. A beam can be accelerated approximately every 2 minutes. When operating in collider mode, the Tevatron stores beam for several hours.

The production of antiprotons and their collision with 900 GeV protons requires additional processes [63]. Antiprotons are created by using a portion of the 120 GeV proton beam from the Main Ring. The proton beam is directed towards the antiproton source shown in figure 3.2. At the antiproton source, the 120 GeV protons collide with a target consisting of either nickel or tungsten (several targets have been used throughout the operation of the antiproton source). The resulting secondary products consist of many different particle types. To select the

antiprotons, a pulsed dipole magnet is used to steer the antiprotons to a collection facility. The production efficiency is low, with one million protons needed to provide approximately 20 antiprotons.

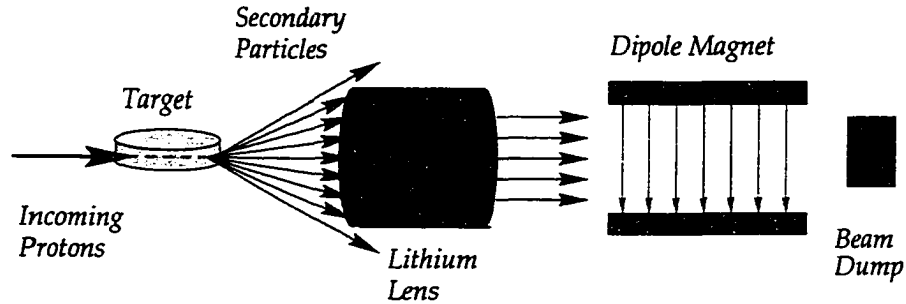


Figure 3.2: Mechanism to produce antiprotons. Protons collide with a target which gives rise to a broad spectrum of secondary particles. The secondary particles are focused by a lithium lens. A pulsed dipole magnet selects antiprotons, while the remaining particles are directed towards a beam dump.

Since the momenta of the antiprotons from the target are not uniform, the antiprotons need to be manipulated to produce high intensity beams with well defined characteristics. Stochastic cooling is employed to create the requisite beam [64]. The cooling occurs by correcting the beam along its path once imperfections have been detected. As the antiprotons pass a point on the synchrotron's ring, a sensor determines whether the beam satisfies certain criteria. If corrections are to be made, a signal is sent across a chord of the ring and applied to the deficient antiproton beam. In this fashion, a sensor-kicker system corrects the phase of each particle to the ideal revolution frequency. The spread in energy and time of the beam is denoted as the longitudinal component. Transverse emittance describes the beam's spread in the momenta p_x and p_y . Various cooling systems are employed to control the behavior of both the longitudinal component and the transverse

emittance. A beam energy profile with constant mean and acceptable width is achieved by reducing the longitudinal component through longitudinal cooling. The luminosity of the beam can be increased by suppressing the transverse motion of the antiprotons in a process called betatron cooling. The antiproton facility uses both cooling methods in sensor-kicker systems.

The antiproton facility consists of two synchrotrons called the Debuncher [65] and Accumulator. The Debuncher is a triangular shaped synchrotron which accepts 8 GeV antiprotons from the antiproton source. The Debuncher does not accelerate the beam, but maintains it at an energy of 8 GeV. Its primary purpose is to reduce the antiprotons' momentum spread and energy distribution through bunch rotation and stochastic cooling [66]. Instead of a discrete set of bunches, the Debuncher attempts to confine a smooth distribution of antiprotons (hence the term Debuncher). Betatron cooling reduces the beam's transverse emittance. The Debuncher employs three RF systems used for maintaining a constant beam energy, rotating the antiproton bunches to cool the beam, and studying beam properties.

Once the characteristics of the beam are appropriate for storage, the antiprotons are injected into the Accumulator. The Accumulator is a synchrotron sharing the same tunnel as the Debuncher designed to cool and store large numbers of antiprotons. The antiprotons in the Accumulator are characterized by a core energy and narrow energy spread. In the stacking process, new antiprotons which enter the Accumulator from the Debuncher are cooled to the core energy. The stacking rate is approximately 4×10^{10} antiprotons per hour. Typically, stacking proceeds until 10^{12} antiprotons are accumulated. When a sufficient number of antiprotons

has been collected, a portion of the beam is accelerated into an injection orbit and transformed into discrete bunches. Three RF systems are necessary in order to accomplish these processes. The Accumulator then sends the 8 GeV antiprotons to the Main Ring.

With the protons stored in the Tevatron, the antiprotons are transferred to the Main Ring in a process called a shot. The same synchrotron can be employed to manipulate protons and antiprotons but with opposite directions of motion for the particles. The antiprotons are accelerated to 150 GeV in the Main Ring and then injected into the Tevatron between the 150 GeV proton bunches. The current in the Tevatron's magnets is increased while the two beams are accelerated to 900 GeV each. The spreading of the beams due to interaction between proton and antiproton is minimized by employing electrostatic separators which maintain the beams in different helical orbits. The protons and antiprotons are stored in the Tevatron. Losses from collisions and transverse spreading of the beam profile decrease the available luminosity over time. After approximately 10 to 12 hours, the remaining 900 GeV protons and antiprotons are removed by steering the beams to a beam dump. The process of preparing new particles for injection into the Tevatron is repeated.

The counter-rotating beams in the Tevatron provide collisions with a center of mass energy of 1.8 TeV. During normal collider operation, 6 bunches of protons and 6 bunches of antiprotons are accelerated. The typical bunch used in Run 1A contained 12×10^{10} protons and 3×10^{10} antiprotons. For Run 1B, this was increased to 22.5×10^{10} protons and 6.5×10^{10} antiprotons. At the points B0 (location of the CDF detector) and D0 (location of the DØ detector; in figure 3.1 this would be on

the Tevatron towards the bottom of the page) along the Tevatron ring, the beams are adjusted and focused in order to produce proton antiproton collisions. The relative difference in position between proton and antiproton bunches is altered by changing the frequency of the RF systems controlling each. The frequency is tuned so that the center of collisions coincides with the nominal detector vertices. A process called squeezing is employed at the B0 collision region to increase the available luminosity. The beta function, β , characterizes the beam's width as the beam transits the Tevatron. Quadrupole magnets at both ends of the B0 collision area¹ serve to reduce the beam's beta function. The beams cross in the interaction regions approximately every 3.5 μ sec corresponding to a frequency of 286 kHz.

3.2 Collider Detector at Fermilab

The collisions which occur at B0 are recorded by a 5 kton general purpose detector, the Collider Detector at Fermilab (CDF). CDF is designed to collect data in the high energy and luminosity environment produced by the Tevatron. The detector has almost complete 4π solid angle coverage and specially designed detector components. Each component is employed to identify a certain class of particle or precisely measure their properties. Figure 3.3 shows one quarter of the detector with rotational symmetry about the beam axis and reflection symmetry between the front and back halves of the detector.

Positions are referenced through use of either Cartesian or cylindrical coordinate systems. The Cartesian coordinate system is defined by a positive x axis directed radially outwards from the Tevatron ring, a positive y axis directed up-

¹CDF denotes these as low beta quadrupoles.

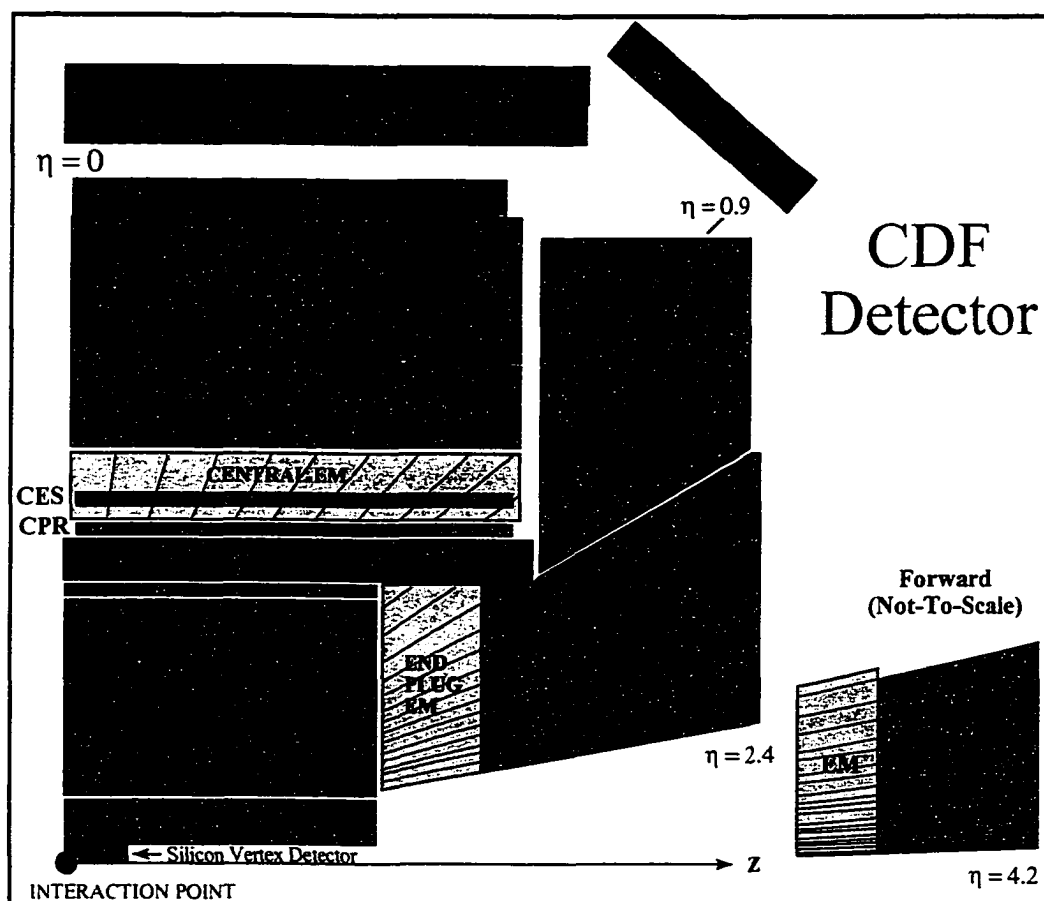


Figure 3.3: Schematic of one quarter of the CDF detector for Run 1. The placement and dimensions of the forward calorimeter is incorrect in the figure, but has been included to illustrate the pseudorapidity range of CDF.

wards, and a positive z axis in the direction of the proton beam direction with origin at the geometric center of the detector. CDF's symmetric construction naturally promotes the specification of positions by cylindrical coordinates. In this system, r is the radial distance from the z axis, ϕ is the azimuthal angle from the positive x axis with increasing values for subsequent clockwise locations with respect to the positive z axis, and z is as before. The description of particle trajectories is simplified by using the azimuthal angle ϕ and the polar angle from the positive z axis, θ .

Since the energy and momenta of the constituents of the proton and antiproton cannot be calculated *a priori* and a significant portion of the resultant particles may travel along the beampipe without detection, determining conserved quantities requires examining components of kinematic variables. The momentum is decomposed as $p^2 = p_T^2 + p_z^2$, with p_T the momentum in the transverse plane to the beam axis and p_z the momentum along the z axis. The transverse momentum, given by

$$p_T = p \times \sin \theta , \quad (3.2)$$

is assumed to be a conserved quantity. High p_T particles are well separated from the remnants of the colliding beams. In analogy, the transverse energy

$$E_T = E \times \sin \theta \quad (3.3)$$

is also regarded as conserved. If the sum of all transverse energy is not zero, the difference is attributed to particles which do not interact with the detector

material, such as neutrinos. Missing transverse energy, \cancel{E}_T , is calculated from the transverse energy measured in the calorimeter using

$$\vec{\cancel{E}} = - \sum_i E_T^i \hat{n}_i \quad (3.4)$$

where the sum is over the number of towers and \hat{n}_i is a unit vector in the transverse plane directed towards the i th tower.

The polar angle θ is commonly supplanted by another measure, the pseudorapidity η . Pseudorapidity is derived from the rapidity, y , which associates the lab frame, \mathfrak{F} , with a frame in which the particle has zero longitudinal momentum, \mathfrak{F}' . Particle velocity written using natural units, $\beta = v$, and rapidity are related by

$$\beta = \tanh y . \quad (3.5)$$

The Lorentz transformation from \mathfrak{F}' to \mathfrak{F} gives

$$p_z = M_T \sinh y \quad \text{and} \quad E = M_T \cosh y \quad (3.6)$$

where $M_T^2 = p_T^2 + m^2$ is referred to as the transverse mass. Solving for longitudinal rapidity, the equation

$$y = \frac{1}{2} \ln \left(\frac{E + p_z}{E - p_z} \right) \quad (3.7)$$

is obtained. The advantage of describing particles by rapidity arises from the additive property of y under Lorentz boosts along the z axis. The transverse

momentum is invariant under longitudinal boosts. Equation 3.7 can be simplified when the momentum is much greater than the mass of the particle. Defining α as

$$\alpha \equiv \frac{m}{p_T}$$

and pseudorapidity as

$$\eta = -\ln \tan \left(\frac{\theta}{2} \right) , \quad (3.8)$$

equation 3.7 can be expanded in terms of α for $p_T \gg m$,

$$y = \frac{1}{2} \ln \left(\frac{\sqrt{\cosh^2 \eta + \alpha^2} + \sinh \eta}{\sqrt{\cosh^2 \eta + \alpha^2} - \sinh \eta} \right) \sim \eta - \frac{1}{2} \alpha^2 \tanh \eta + \mathcal{O}(\alpha^3) . \quad (3.9)$$

As $\alpha \rightarrow 0$, the rapidity is equivalent to the pseudorapidity. In this approximation, boosts along the z axis of velocity β transform as $\eta \rightarrow \eta - \tanh^{-1} \beta$. Another benefit of employing pseudorapidity is the experimental observation that for $|\eta| < 3$, the particle density per unit rapidity from proton antiproton collisions is roughly constant.

Two distinct pseudorapidities with different meanings exist. Detector pseudorapidity, η_d , is determined with reference to the center of the detector. Along with r and the assumption of symmetry in ϕ , η_d indicates the position of the detector components. Physical segmentation is frequently specified in terms of the angles η_d and ϕ . Since the distribution of the interaction region is approximately Gaussian with a spread of 60 cm, employing a coordinate fixed to a detector location conceals the structure of a collision event. Instead of η_d , the pseudorapidity of the

particles produced from proton antiproton collisions are calculated with respect to the interaction vertex. This event pseudorapidity is denoted as η . Often, the notation η is used for both pseudorapidities with the meaning understood from the context.

The total number of collision events which occur at B0 is governed by the luminosity of the Tevatron. The instantaneous luminosity, measured in $\text{cm}^{-2} \text{sec}^{-1}$ and written using accelerator parameters, of a synchrotron proton antiproton collider is [61]

$$\mathcal{L} = \frac{N_p N_{\bar{p}} N_B f}{4\pi\sigma^2} , \quad (3.10)$$

where N_p and $N_{\bar{p}}$ represent the number of protons and antiprotons per bunch, respectively, N_B is the number of bunches in either the proton or antiproton beam, f is the revolution frequency, and σ^2 is the root-mean-square cross sectional area of a bunch. The instantaneous luminosity is monitored at CDF by the Beam Beam Counters (see section 3.2.6). The average instantaneous luminosity in Run 1 was approximately $5 \times 10^{30} \text{ cm}^{-2} \text{sec}^{-1}$. The quantity of available information is determined by integrating the instantaneous luminosity over the periods in which collision events were recorded. Run 1a, which collected data from August 1992 to May 1993, gathered an integrated luminosity of

$$\int \mathcal{L} dt = (19.6 \pm 0.8) \text{ pb}^{-1} .$$

After a brief pause to allow for detector improvements, CDF was exposed to proton antiproton collisions from January 1994 to July 1995. The integrated luminosity

obtained from Run 1b,

$$\int \mathcal{L} dt = (89.0 \pm 3.6) \text{ pb}^{-1} ,$$

significantly increased the volume of data. All of Run 1 provided

$$\int \mathcal{L} dt = (108.6 \pm 4.5) \text{ pb}^{-1} \quad (3.11)$$

for the combined integrated luminosity. The number of events for a particular process is computed using

$$N = \sigma \times \int \mathcal{L} dt , \quad (3.12)$$

where σ is the cross section of the interaction in units of cm^2 . The inelastic cross section for proton antiproton collisions at $\sqrt{s} = 1.8 \text{ TeV}$ is approximately $5 \times 10^{-26} \text{ cm}^2$. With an average instantaneous luminosity in Run 1b of $10^{31} \text{ cm}^{-2} \text{ sec}^{-1}$, the interaction rate is determined to be roughly 0.5 MHz. A bunch crossing time of $3.5 \mu\text{sec}$ will yield approximately 2 interactions per crossing.

The products of the collision events are recorded by various detector components. A list of major subsystems can be found in table 3.1. CDF's capabilities include charged particle tracking, high resolution momentum measurements, precision impact parameter determination, and finely segmented electromagnetic and hadronic calorimetry. The primary components of the tracking system are the silicon vertex detector (SVX) and the charged tracking chamber (CTC). Both are subjected to a 1.4 Tesla magnetic field along the proton beam path provided by

Table 3.1: CDF detector systems. The systems are composed of several elements which are denoted by various abbreviations.

System	Element	Abbreviation
Luminosity	Beam Beam Counters	BBC
Tracking	Silicon Vertex Detector	SVX
	Vertex Tracking Chamber	VTX
	Central Tracking Chamber	CTC
	Central Drift Tube Array	CDT
	Central Electromagnetic Strip Chamber	CES
Calorimetry	Central Electromagnetic	CEM
	Central Hadronic	CHA
	Wall Hadronic	WHA
	Plug Electromagnetic	PEM
	Plug Hadronic	PHA
	Forward Electromagnetic	FEM
	Forward Hadronic	FHA
Muon Detectors	Central Muon	CMU
	Central Muon Upgrade	CMP
	Central Muon Extension	CMX
	Forward Muon	FMU

a superconducting solenoid magnet. Charged particles in the CTC will follow helical trajectories permitting accurate measurements of momenta. Calorimeters surround the solenoid and are layered in sections specialized for particles which interact predominantly via either bremsstrahlung and pair creation or inelastic nuclear collisions. The components furthest in r from the interaction point are drift chambers designed to identify muons.

Electronic data paths to the detector components are designated as channels. The number of channels required to record an event from the SVX, calorimeters, and drift chambers is approximately 46,000, 60,000, and 44,000, respectively. Channels with primal triggering information send analog signals to detec-

tor mounted, or front-end, electronics. Once an event satisfies various criteria, the signals are transmitted from the collision hall to the counting room. In the counting room, the signals are digitized using either analog-to-digital or time-to-digital converters. Further requirements are imposed on the digital information to select data which will be stored on 8mm tape.

Detector subsystems utilized to construct Min-Bias, Jet20, Z boson, and J/ψ B data samples for the investigation of the underlying event are described in the following sections. Other surveys of CDF furnish additional details [67, 68].

3.2.1 Silicon Vertex Detector

The silicon vertex detector (SVX) is the tracking system closest to the beam and capable of the finest resolution in the r - ϕ plane [69, 70]. It uses silicon wafers as the active medium. These wafers are incorporated into SVX ladders which are mounted on a cylindrical structure called a barrel. Two identical barrels are connected at $z = 0$ and provide a total active length of 51 cm. The number of channels read from the SVX is 46.080. The original silicon vertex detector used during Run 1a was replaced with a device capable of tolerating the higher radiation exposures of Run 1b. Although similar to the SVX, the SVX' had alternating instead of direct current coupled silicon detectors and special radiation-hard readout chips [71]. Since the distinction is not significant for most purposes, both devices are commonly referred to as the SVX.

Silicon microstrip sensors are employed by the SVX to measure the positions of charged particles. By utilizing feature sizes at the sub-micron level common in semiconductor manufacturing today, an instrument capable of producing high

precision results is obtained. An approximately $300\text{ }\mu\text{m}$ thick n type silicon wafer is embedded with p type silicon strips. The separation between adjacent strips is either 55 or $60\text{ }\mu\text{m}$. At each strip implant location, a pn junction exists. Mobile charge carriers are removed by applying a reverse bias voltage across the sensor. Electrons and holes are produced through ionization when charged particles travel through the silicon wafer. An electric field causes the electrons to drift towards the nearest strip. A current is induced which creates the signal used in the readout measurement. The components of these detectors are called single-sided silicon since only one side of the wafer contains the strips.

The silicon detectors are attached to a low density material along with necessary electronics forming a ladder. Three silicon microstrip detectors are bonded together providing a total active length of 25.5 cm . The silicon detectors rest on a Rohacell foam substrate. A circuit board on one end of the ladder contains readout chips. These chips receive the electric signals generated in the readout strips. Once the signals are processed, the chips send the signals to electronics not mounted on the ladder. Each chip serves 128 channels. The entire assembly is attached to a carbon fiber support. A diagram of an SVX ladder is given in figure 3.4.

Individual ladders are mounted on a rigid structure which provides cooling for electronics called a SVX barrel. A schematic of the 4 layer microstrip vertex detector barrel is given in figure 3.5. The ladders are assigned to one of four concentric barrel layers of constant r with the first and fourth layers having an inner radius of 2.86 cm and 7.87 cm , respectively. Each ladder is oriented such that the direction of maximum length is parallel to the beam. An azimuthal range of approximately 30° is subtended by an individual ladder. A slight overlap between

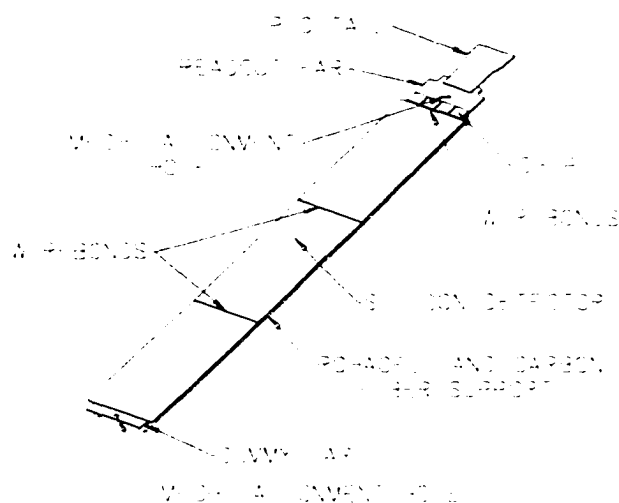


Figure 3.4: A schematic of a SVX ladder for an inner barrel layer. Three silicon detectors are wirebonded together and attached to readout electronics mounted on a common support structure. The dummy ear is connected to a corresponding ladder in another SVX barrel.

neighboring ladders within the same layer exists to provide complete coverage in ϕ . One complete barrel layer is composed of 12 ladders. To accommodate a fixed number of ladders per layer while maintaining the full azimuthal measurement capability, the number of readout strips in the silicon detectors must increase for larger radii resulting in a commensurate increase for the ladder widths. The ladders in the innermost layer contain 256 readout strips, whereas those in the outermost layer have 768. The strips are separated by $60\ \mu\text{m}$ in the inner 3 layers and $55\ \mu\text{m}$ in the fourth layer.

The SVX supplies measurements in the r - ϕ plane vital for determining precise impact parameters. Radial information is obtained by noting the SVX layer from which a signal is received. Since the strips in the silicon detectors are parallel to the beam, only ϕ information can be obtained from the drift of electrons and holes

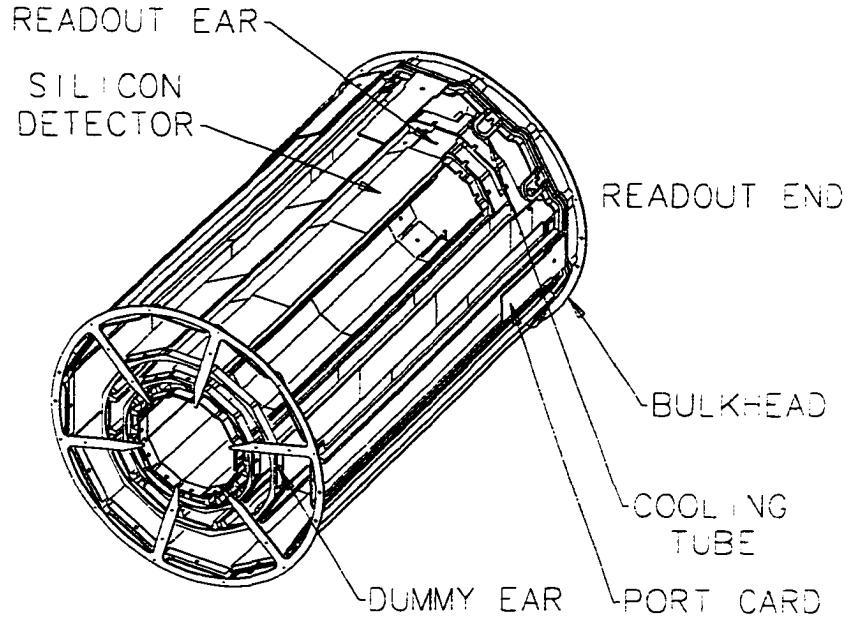


Figure 3.5: Configuration of the ladders within a SVX barrel and the accompanying support instrumentation.

within the semiconductor material. The lack of segmentation in z or a tilt of the strips with respect to the beamline renders the SVX incapable of recording z information. The r - ϕ hit positions in the SVX are used to reconstruct vertices with a resolution allowing primary and secondary interaction vertices to be differentiated. The position resolution for the SVX and SVX' is 13 and 11.6 μm , respectively. For high transverse momentum charged particles, the impact parameter is determined with a resolution of approximately 17 μm for the SVX and 13 μm for the SVX'. Since the z position of proton antiproton collisions is distributed as a Gaussian centered at $z = 0$ with a deviation of approximately 30 cm, many interaction ver-

tices are not contained within the length of the SVX. This results in a geometric acceptance for the SVX of approximately 60%.

3.2.2 Vertex Tracking Chamber

The vertex tracking chamber (VTX) is a time projection detector designed to record r - z measurements. Reconstructed tracks from the VTX are utilized to determine the z position of primary vertices and the presence of multiple proton antiproton interactions within the same beam crossing. The VTX is located directly outside the SVX and extends 22 cm from the beamline. With a length of 264 cm, a pseudorapidity region of $|\eta_d| < 3.5$ is covered.

The VTX is composed of 28 drift modules. Each module is separated into two drift regions by a central high voltage grid and segmented in ϕ into 8 wedges. Sense wires are connected within the wedges such that, when viewed in the r - ϕ plane, the wires form chords of circles centered on the beamline. The 20 end modules each contain 24 sense wire pairs. To accommodate the SVX, the inner 18 modules are smaller employing only 16 sense wire pairs. The drift electric field is maintained at approximately 1600 V/cm in a gas mixture primarily composed of argon and ethane in equal proportion with trace amounts of isopropyl. The drift electrons will travel along the z direction.

Radius measurements are given by hits registered on specific sense wires. Drift times from adjacent wires are used to determine positions in z . When this information is combined, particle trajectories in the r - z plane can be reconstructed. Adjacent modules are rotated 15° with respect to one another providing rudimentary r - ϕ information for those particles crossing multiple modules.

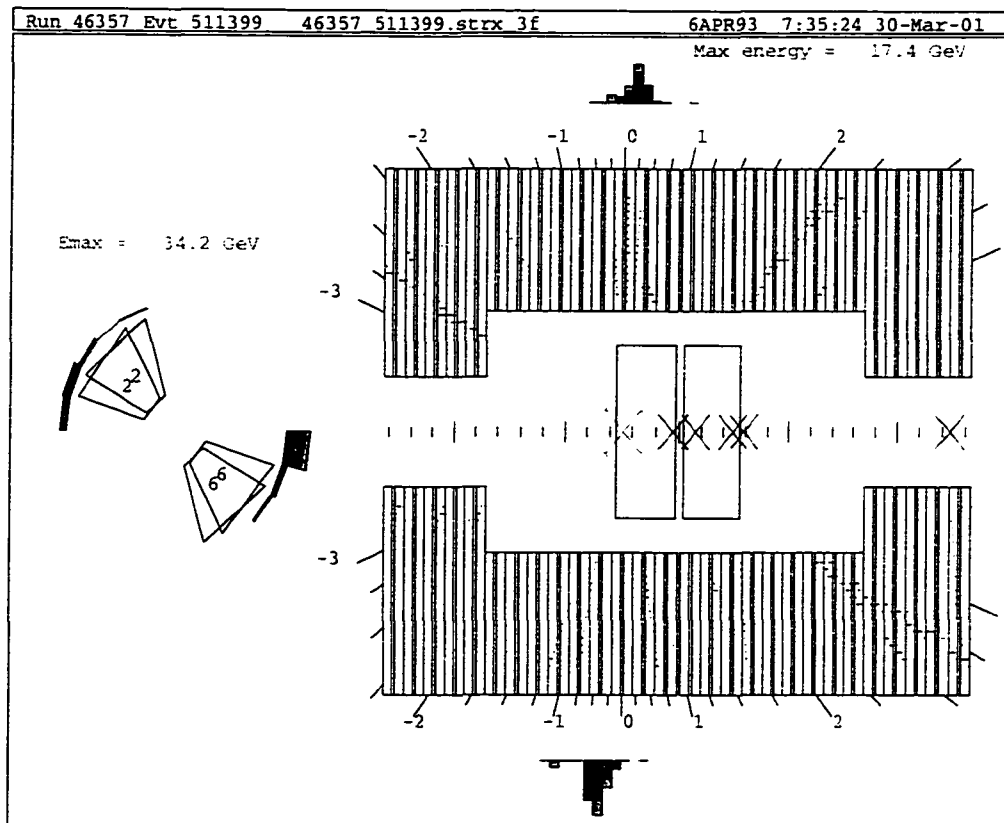


Figure 3.6: Views of the VTX from the CDF event display software package in both r - ϕ (left) and r - z (right). The r - ϕ view identifies the VTX octants containing sense wire hits. The r - z view shows the sense wire hits within the 28 drift modules. The positions of the SVX barrels are noted by the two large boxes within the VTX. Calorimetry information is provided in both views by the rectangular indicators outside of the VTX. The crosses along the beamline in the r - z view represent reconstructed vertices. A high-quality primary vertex is indicated by the large serifed cross. The event pseudorapidity is calculated from this vertex and marked on the outside of the VTX r - z view.

The z position of the primary interaction vertex is determined by the VTX vertex finding algorithm. Reconstructed r - z tracks are extended to the beamline and a scan for intersections of multiple tracks is performed. The quality of identified vertices is dependent on the number of tracks associated with a particular vertex and the available sense wire hits used to reconstruct each track. Primary and poorly reconstructed vertices found by the VTX algorithm are shown in figure 3.6. The resolution of the primary interaction z location is approximately 1 mm. Since the VTX z resolution is finer than that obtained from the CTC, the z vertex position measured by the VTX is employed as a seed for the three dimensional track reconstruction performed using CTC information.

3.2.3 Central Tracking Chamber

The central tracking chamber (CTC) records wire hit information from which charged particle tracks are reconstructed. These tracks are extrapolated to other detector subsystems where additional information is integrated to obtain a variety of particular parameters characterizing the passage of individual particles. Three dimensional track reconstruction is possible using CTC measurements alone making it the only detector component capable of independent tracking. Cylindrically symmetric with dimensions of inner diameter 55.4 cm, outer diameter 276 cm, and length 320.13 cm, the CTC encompasses the region $|\eta_d| \leq 1.1$. The VTX is located at smaller radii with the superconducting solenoid magnet at larger radii. The CTC was employed for all of Run 1, suffering from a broken wire during Run 1c which degraded its performance slightly. Together with the SVX and VTX, the CTC provided precision hit measurements of charged particles.

The CTC is an open cell drift chamber utilizing a total of 36,504 sense, potential, field, and field shaper wires in an argon (49.6%), ethane (49.6%), and ethanol (0.8%) gas mixture. The 6,156 $40\ \mu\text{m}$ diameter gold plated tungsten sense wires are used to measure the passage of charged particles through the drift chamber. The sense wires are arranged into 84 layers which are categorized into 9 superlayers. Five axial and four stereo superlayers exist which correspond to differing wire orientations. The CTC is composed of an alternating pattern of axial and stereo superlayers, with the superlayer nearest the beamline of axial type. The layers are labeled in order of increasing radii from the beamline as 0,2,4,6,8 for axial and 1,3,5,7 for stereo superlayers. Each superlayer is divided in the plane transverse to the beam into cells. The position of the cells in the superlayers is displayed in figure 3.7.

Individual cells constitute self-contained elements which record hits from drift electrons within that cell. Cells located in axial and stereo superlayers employ 12 and 6 sense wires, respectively. The orientation of sense wires in the axial superlayers is parallel to the beamline and in the stereo superlayers alternates between $+3^\circ$ and -3° with respect to the beamline for successive stereo layers. An electric field of strength 1350 V/cm and uniform at the 1.5% level is maintained by steel field and field shaper wires. The perimeter of the cell is marked by the field wires which are to either side of the sense wires isolating the cell from others. The maximum drift distance within a cell is approximately 40 mm. This distance corresponds to a drift time of 800 nsec which is less than the $3.5\ \mu\text{sec}$ beam crossing time. The signals from each sense wire are sent to time-to-digital converters (TDCs) designed to read at least 8 hits per wire in an event.

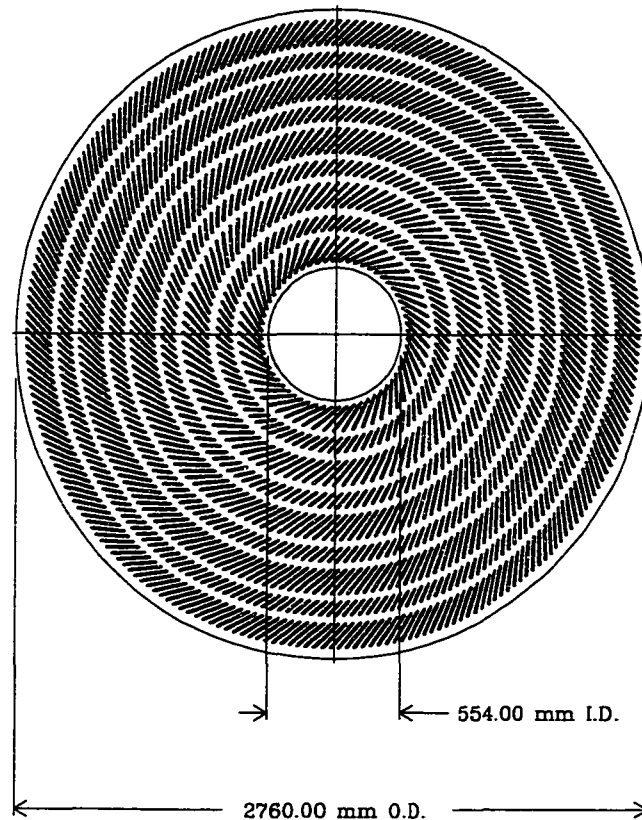


Figure 3.7: View of the central tracking chamber end plate. The wire slot locations of the nine superlayers are shown. The larger cells are located in the axial layers, whereas the smaller cells are in the stereo layers.

The presence of the axial magnetic and the drift electric fields in the cells causes the drift electrons to travel at an angle with respect to the electric field. To compensate for the Lorentz angle of the electrons, the cells are tilted. The degree of inclination is dependent upon the strength of the magnetic and electric fields and the constitution of the drift medium. The CTC properties entail a Lorentz angle of approximately 45° . Rotating the cells such that they create a commensurate angle to the radial direction produces drift electrons which move predominantly

in the azimuthal plane. In addition to creating the aesthetic spiral pattern seen in figure 3.7, the tilted drift cells aid in resolving the left-right ambiguity problem and provide added redundancy due to an approximately 20% overlap between superlayers.

Charged particles traversing the CTC volume are detected by sense wire hits. The axial superlayers provide r - ϕ position information with stereo superlayers furnishing data in the r - z plane. The single hit, wire resolution is approximately $200\text{ }\mu\text{m}$. Single hit, stereo wire resolution for z position measurements is $0.2\text{ mm}/\sin 3^\circ \simeq 4\text{ mm}$. To resolve two hits on the same wire, a minimum separation of 100 nsec is needed resulting in a double track resolution of approximately 5 mm. In order to pass through the CTC and avoid entrapment by the magnetic field, the charged particles must have $p_T \geq 0.275\text{ GeV}/c$. High momentum particles with $|\eta| \leq 1$ cross all 9 superlayers. Efficient track reconstruction on the order of approximately 90% occurs for charged particles in the central region with $p_T \geq 0.4\text{ GeV}/c$ [72]. For particles in the range $1 < |\eta| \leq 2$, only hit information from the inner superlayers can be used for track reconstruction resulting in poorer precision.

Axial and stereo superlayer measurements are combined by the CTC tracking algorithm to form three dimensional tracks. The algorithm begins by examining hits within each axial superlayer cell. These hits are used to create track segments, which when fit to an arc, produce track candidates in the r - ϕ plane. Once a r - ϕ candidate is found, stereo track reconstruction proceeds. Employing the VTX measured position of the primary vertex as a seed, the r - z track is determined from hits in the stereo superlayers. The r - ϕ and r - z measurements provide information for construction of the three dimensional tracks.

A charged particle subject to the uniform magnetic field in the longitudinal direction follows a helical path around an axis parallel to the magnetic field. This helix is parameterized by the five quantities z_0 , d_0 , ϕ_0 , θ_0 , and C . The z position at the point of closest approach to the origin defines z_0 . The impact parameter d_0 is the minimum distance in the transverse plane between the helix and the the origin. The track direction in the transverse plane at the impact parameter point gives ϕ_0 . The polar angle at the impact parameter point is θ . The half-curvature

$$C = \frac{1}{2QR}$$

is related to the radius, R , of the circle traced in the transverse plane by the helix and the particle's charge, Q .

The momenta of charged particles are calculated from their trajectories in the CTC. The transverse momentum component can be determined from the curvature of a particle's helix. With R in meters and B in Tesla, the transverse momentum in units of GeV/c is obtain by

$$p_T = 0.3z_{chg}RB$$

where $z_{chg}e$ is the charge of the particle. High momentum particles have little curvature and are espied by essentially straight reconstructed tracks. While the uncertainty in hit resolution is constant for infinite momentum tracks, a momentum dependent correction is necessary at low p_T . Since the curvature is directly related to the measured hits, the transverse momentum resolution will also have a momentum dependence. The momentum resolution of charged particle tracks

reconstructed using CTC information alone is

$$\frac{\delta p_T}{p_T} \leq \sqrt{(0.002 p_T)^2 + (0.0066)^2} . \quad (3.13)$$

When applicable, the CTC tracks can be extended into the SVX by projection roads and SVX information incorporated. The combined SVX-CTC momentum resolution improves to [73]

$$\frac{\delta p_T}{p_T} \leq \sqrt{(0.0009 p_T)^2 + (0.0066)^2} . \quad (3.14)$$

For values of $p_T > 10$ GeV/c, the constant term arising primarily from multiple scattering in the equations above is often neglected.

3.2.4 Calorimeters

The CDF calorimeters provide extensive coverage of the detector volume and accurate measurements of particle energy. The system surrounds the solenoid and is located at a pseudorapidity of $|\eta| < 4.2$ with complete 2π azimuthal angle. The calorimeters are segmented in solid angle into towers around the collision point. Figure 3.8 shows an eighth of the system in η - ϕ space with the central, endwall, endplug, and forward components indicated. Particles with $p_T \gtrsim 350$ MeV/c pass through the magnetic field and can be detected in the calorimeters. The measurements recorded by the calorimeters aid in the identification of electrons, muons, and photons. In addition, collections of tracks in η - ϕ space which create energy clusters in the calorimeters and originate from a common vertex often characterize particle jets. Jet energies are typically measured by the calorimeters.

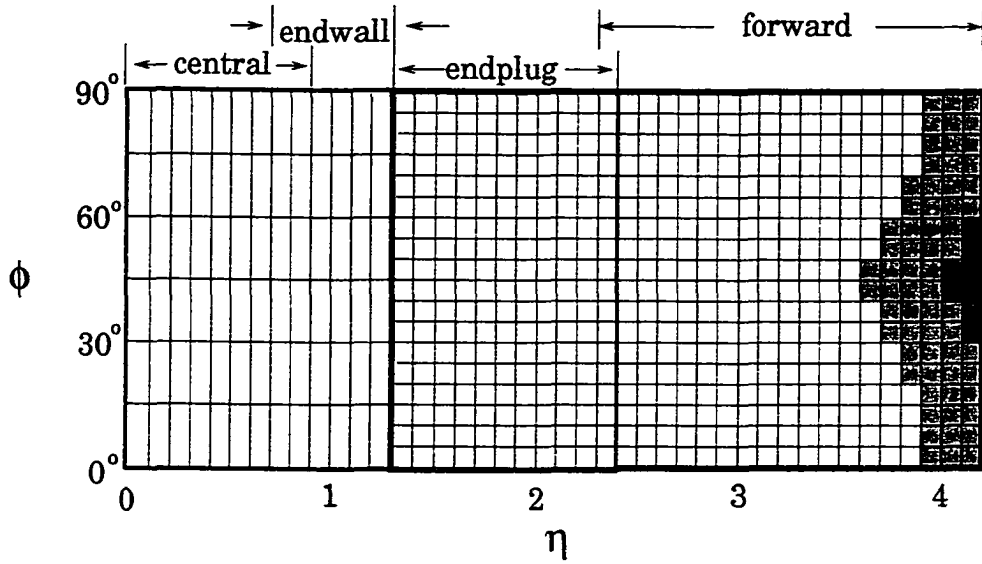


Figure 3.8: Segmentation of the calorimeter system at CDF in $\eta - \phi$ space. For $\phi \sim 45^\circ$, the shaded region at $\eta \sim 3.6$ represents only electromagnetic calorimeter coverage and the dark region at $\eta \sim 4.0$ represents no calorimeter coverage. The complete system is composed of eight such figures.

The calorimeter system determines particle energy through the technique of shower sampling. In shower sampling, high momentum particles traversing passive components interact via electromagnetic or nuclear forces to produce additional particles which form a shower. The number of particles in a shower is related to the energy of the incident particle. The characteristics of the shower are measured (or sampled) by an active material. For an active material composed of scintillator, the observed light is proportional to the shower particle multiplicity. Therefore, the light output from a scintillator provides a measurement of the incident particle energy.

CDF's calorimeters are constructed using several layers of dense, passive material interleaved with active components. Constituents of the showers may them-

selves interact with the passive material and produce additional particles. A particle shower can transit several layers of absorber with the total sampled signal approximately proportional to the energy of the incident particle. The layers are divided into two components which primarily measure specific characteristics for different species of incident particles.

Electromagnetic calorimeters use passive materials with a high number of shell electrons. Thin sheets of lead providing detailed sampling of electromagnetic showers are employed at CDF. The CEM is composed of 31 layers of 3.2 mm lead alternating with 5 mm plastic scintillator sheets. High energy electrons are usually confined to the electromagnetic calorimeter. Incident high energy photons will produce electron and positron pairs. Proportional strip and wire chambers denoted as the central electron shower detector (CES) are located at a depth in the CEM corresponding to the approximate position of the maximum energy deposition for electromagnetic showers.

Hadronic calorimeters typically require large amounts of material to contain high energy hadrons. The incident hadrons undergo inelastic nuclear collisions within the absorber material. Thick steel plates are utilized by CDF as the passive component. The CHA is constructed in 32 layers consisting of 25 mm steel alternating with 10 mm plastic scintillator sheets. The hadronic calorimeters are located directly behind the electromagnetic calorimeters.

The calorimeter system is separated into central, endwall, endplug, and forward regions. The endwall calorimeter is often treated as part of the central system due to similar construction and presence of components specialized for hadronic measurements only. Considering central, endplug, and forward systems, each of the

Table 3.2: Characteristics of the CDF calorimeters. Segmentation corresponds to the tower size in $\Delta\eta \times \Delta\phi$ and energy resolution is given by σ_E/\sqrt{E} with energy measured in GeV. The symbol \oplus in the energy resolution denotes addition of the constant term in quadrature.

System		η Coverage	Segmentation	Energy Resolution
Central	CEM	$ \eta < 1.1$	$0.11 \times 15^\circ$	$13.7\%/\sqrt{E} \oplus 2\%$
	CHA	$ \eta < 0.9$	$0.11 \times 15^\circ$	$50\%/\sqrt{E} \oplus 3\%$
	WHA	$0.7 < \eta < 1.3$	$0.11 \times 15^\circ$	$75\%/\sqrt{E} \oplus 4\%$
Plug	PEM	$1.1 < \eta < 2.4$	$0.09 \times 5^\circ$	$22\%/\sqrt{E} \oplus 2\%$
	PHA	$1.3 < \eta < 2.4$	$0.09 \times 5^\circ$	$106\%/\sqrt{E} \oplus 6\%$
Forward	FEM	$2.2 < \eta < 4.2$	$0.1 \times 5^\circ$	$26\%/\sqrt{E} \oplus 2\%$
	FHA	$2.4 < \eta < 4.2$	$0.1 \times 5^\circ$	$137\%/\sqrt{E} \oplus 3\%$

three regions is composed of electromagnetic and hadronic calorimeters. Individual systems are constructed from several identical modules which are subdivided into towers. The η - ϕ characteristics of a tower are maintained for the tower length. A projective geometry in which the towers indicate the nominal position of the detector interaction point is fashioned. Table 3.2 shows several properties of the calorimeter systems. The energy resolution of the electromagnetic calorimeters is determined from testbeam measurements of incident electrons and photons. Similarly, the energy resolution for the hadronic calorimeters is ascertained using incident isolated pions.

3.2.5 Muon Chambers

The small interaction cross section of muons in comparison to electrons, photons, and hadrons of the same energy motivates placement of the muon chambers several interaction lengths from the collision point. The muon detectors consists

of multiple layers of drift chambers with coverage in η - ϕ for CMU, CMX, and CMP as shown in figure 3.9. Track segments within the muon chambers can be constructed and are denoted as muon stubs. Most muons will deposit energy in the calorimeters characteristic of a minimum ionizing particle. The magnitude of energy deposited in the calorimeter system provides additional criteria useful in selecting muons.

3.2.6 Beam Beam Counters

The Beam Beam Counters (BBCs) are a pair of scintillator plate arrays positioned in front of the forward calorimeters 5.82 m from the nominal interaction point. An array is composed of 16 scintillator counters. Two phototubes are attached to each scintillator with both an anode and an inverted dynode signal measured from each phototube. The scintillator material is the primary determinant of the capabilities of the BBCs, with an overall time resolution less than 200 psec. The BBCs approximately² cover a range in pseudorapidity of $-5.9 \leq \eta \leq -3.24$ and $3.24 \leq \eta \leq 5.9$. Although initially designed for an instantaneous luminosity of $10^{30} \text{ cm}^{-2} \text{ sec}^{-1}$, the BBCs continued to function at a luminosity of $1.2 \times 10^{31} \text{ cm}^{-2} \text{ sec}^{-1}$.

The BBCs served to provide a minimum bias (Min-Bias) trigger and a luminosity monitor [74]. A BBC coincidence, defined as at least one hit in each of the forward and backward BBCs within a 15 nsec window around the beam crossing time, is required for both Min-Bias and luminosity measurements. The existence of a BBC coincidence is indicative of an interaction during a particular crossing.

²The profile of the BBCs in the x - y plane is square and not circular.

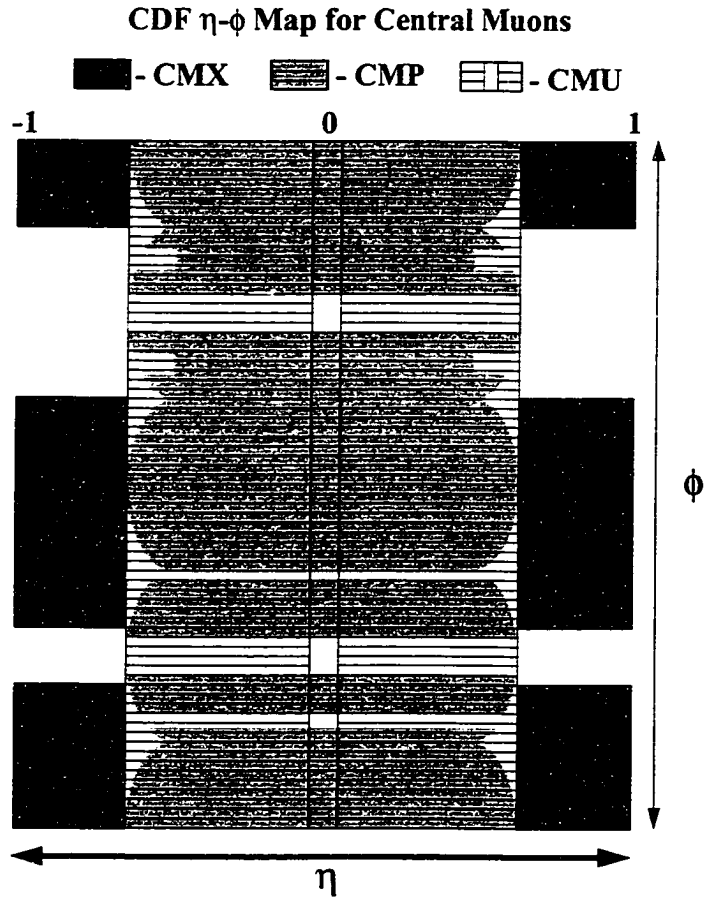


Figure 3.9: CDF central muon coverage in η - ϕ . The ϕ gaps in the CMX detector occur when the CMX intersects the floor (large gap) and the Tevatron (small gap).

The rate of hits in the BBCs can be used to create a method to normalize all other cross section measurements.

The instantaneous luminosity at CDF determined from BBC information can be calculated by

$$\mathcal{L} = \frac{f_0}{\sigma_{\text{BBC}}} \langle n \rangle \quad (3.15)$$

where f_0 is the Tevatron frequency (286.272 kHz) and $\langle n \rangle$ is the mean number of interactions per crossing. The effective cross section for the BBC counters, σ_{BBC} , is [74, 75]

$$\sigma_{\text{BBC}} = \sigma_{\text{tot}} \frac{N_{\text{BBC}}^{\text{vis}}}{N_{\text{tot}}} \quad (3.16)$$

with σ_{tot} the total $p\bar{p}$ cross section as measured by CDF [76], N_{BBC} the number of BBC triggered events, and N_{tot} the total number of elastic and inelastic events. The value of the BBC cross section is determined to be $\sigma_{\text{BBC}} = 51.15 \pm 1.6$ mb.

The derived quantity $\langle n \rangle$ can be replaced with an expression dependent on the directly measurable parameters f_0 and the BBC coincidence rate, R_{BBC} . Assuming a Poisson distribution for the number, α , of $p\bar{p}$ interactions per beam crossing

$$P(\alpha) = \exp(-\langle n \rangle) \frac{\langle n \rangle^\alpha}{\alpha!}$$

and a probability to have at least one BBC coincidence per crossing

$$\sum_{\alpha} P(\alpha) = 1 - P(0) = \frac{R_{\text{BBC}}}{f_0} ,$$

the mean number of interactions per crossing is written as

$$\langle n \rangle = -\ln \left(1 - \frac{R_{\text{BBC}}}{f_0} \right) . \quad (3.17)$$

Substituting this expression into equation 3.15, the instantaneous luminosity is given by

$$\mathcal{L} = -\frac{f_0}{\sigma_{\text{BBC}}} \ln \left(1 - \frac{R_{\text{BBC}}}{f_0} \right) . \quad (3.18)$$

Saturation of the BBC counters at high luminosity suppresses the value of R_{BBC} in comparison to what would be obtained if no saturation occurred. Alternatively, R_{BBC} may be enhanced due to beam gas and halo events. These extraneous sources of BBC coincidence can be described by a function of instantaneous luminosity and removed from the integrated luminosity [77, 75].

3.2.7 Triggers

The high crossing rate of 286 kHz with multiple interactions per crossing conspire to prevent the storage of complete information from all proton antiproton collisions. With a typical memory size of approximately 165 kbytes for an event, data can only be reliably written to 8 mm tapes at a rate of 10 Hz. In order to accommodate the requisite lower rate while selecting potentially interesting physics data, criteria are employed to select events for desired characteristics. Various stages of analysis with increasingly sophisticated requirements are needed in order to minimize the time in which collision events cannot be examined due to engagement with previous data. This dead-time would be approximately 99.7% for a

Table 3.3: CDF Level 1, 2, and 3 trigger acceptance rates at an instantaneous luminosity of $5 \times 10^{30} \text{ cm}^{-2} \text{ sec}^{-1}$.

Trigger Level	Acceptance Rate
1	1 kHz
2	12 Hz
3	5 Hz

single stage filter of 1 msec duration representative of the highest level filter at CDF. The selection criteria are encoded in hardware and software filters called triggers. The event rates presented to successive trigger levels decreases allowing for increasingly complex and time consuming analysis without incurring significant dead-time.

CDF employs a three stage trigger system [78]. The first and second stages, denoted as Level 1 and Level 2 triggers, respectively, select events which satisfy criteria programmed in hardware and FASTBUS control software. The third stage (Level 3) implements software algorithms to analyze the events in a detailed fashion. Level 2 and 3 triggers are programmable. The effect on the data rate is shown in table 3.3. From approximately 60,000 events, one event is recorded.

The Level 1 triggers determine if an event should be retained for further examination within $3.5 \mu\text{sec}$ eliminating any dead-time. This capability is due to the use of fast analog outputs from the calorimeters and central muon detectors for the trigger's decision. Dedicated FASTBUS electronics read out and process the data from the detector components. For the calorimeters, the information is segregated into trigger towers. The size of an individual trigger tower is larger than the usual segmentation of the calorimeter with an $\eta \times \phi$ for a trigger tower of

$0.2 \times 15^\circ$. Events associated with energies registered in any trigger tower above a predetermined threshold will be retained. The Level 1 trigger for the calorimeter can be prescaled to accept only a few events out of the total number which satisfy the trigger requirement allowing the trigger tower thresholds to be lowered. The muon information used in the Level 1 trigger originates in the CMU and CMX systems. Signals from the radially aligned wires in the drift cells define muon track segments. The transverse momentum of the charged particle creating the track segment is estimated by determining the deflection angle due to the magnetic field from the arrival times of drift electrons on the sense wires. The charged particle's momentum is then compared with predetermined momentum values. Several combinations of track segment criteria can be utilized in the Level 1 muon triggers to find events of interest. With an acceptance rate of 1 kHz, 0.4% of the events are accepted and submitted to the next trigger level.

The time necessary for the Level 2 trigger to process an event varies as the characteristics of the event topology change. A typical event can be analyzed in less than $30 \mu\text{sec}$ while an event with many tracks and large energy deposition in the calorimeters may require an order of magnitude more time. An approximately 12% dead-time is introduced since the Level 2 trigger is unable to handle all ~ 9 events which occur during the trigger's decision time. Selection proceeds by comparing criteria with electromagnetic and hadronic cluster energy, track parameters in the CTC, track segments in the muon detectors, and missing transverse energy.

Energy clusters are calculated by the hardware cluster finder which searches the calorimeter for seed towers and sums the appropriate nearest neighboring towers. Seed towers are defined as those calorimeter towers which have an energy deposition

greater than a specific threshold³. The four nearest neighbor towers are included in a cluster if they individually register an energy deposition greater than another threshold⁴. Each of the included towers is subjected to the same analysis and the cluster is extended until no calorimeter towers satisfying the requirements can be found. The E_T of the cluster is determined by summing all towers within the cluster. From this, an E_T weighted η - ϕ position with associated uncertainties σ_η and σ_ϕ for the cluster is calculated.

Track reconstruction in the r - ϕ plane occurs using the central fast track processor (CFT). The CFT receives signals from the axial CTC superlayers within a time window of 80 nsec after the proton antiproton collision. Signals appearing in the same axial superlayer at either side in ϕ of the original signal within a time window of approximately 650 nsec are generated by drift electrons. These later signals allow the transverse momentum of the charged particle to be calculated from the direction and curvature of the track. The CFT builds CTC tracks in approximately 10 μ sec. Tracks which satisfy minimum transverse momentum threshold criteria can be selected.

Energy clusters in the calorimeters and track segments in the muon detectors are associated with extrapolated CTC tracks and the quality of agreement computed. By summing the E_T from all energy clusters, an accurate measurement of missing transverse energy, \cancel{E}_T , can be determined. Requirements for events to contain features consistent with specific particles can be employed. Only 1.2% of the events accepted by the Level 2 trigger are forwarded to the succeeding level.

³Typical seed tower threshold energies are 3, 5, and 8 GeV.

⁴Typical neighbor tower threshold energies are 1 GeV and 1 GeV less than the seed tower threshold.

The Level 3 trigger employs complex requirements to determine if an event is of potential interest. The trigger has access to information from all detector components, the signals of which were digitized once the event passed the Level 2 trigger. Significant potential dead-time is incurred since the Level 3 trigger requires more than 1 msec for processing. The analysis reconstructs the entire event using software algorithms executed on multiple processor machines⁵ capable of approximately two billion operations per second. Due to the complexity of the task, reconstructing three dimensional tracks in the CTC consumes the largest percentage of computer time.

Electron candidates are determined by extrapolating the CTC tracks to the face of a calorimeter and matching the electromagnetic energy cluster in the r - ϕ and r - z planes to within a few centimeters. Since the electron has low mass, the CTC measured p_T should be approximately equivalent to the E_T of the electromagnetic cluster. For both electrons and photons, the energy deposited in neighboring towers and the profile of the transverse development of the shower measured in the CES must be consistent with expectations for electrons and photons. To find muon candidates, the CTC tracks are matched in both r - ϕ and r - z planes with track segments in the muon chambers. Differences in position between the extrapolated CTC track and track segment can be utilized as a measure to select muon candidates.

Once electron, photon, and muon candidates have been identified, jets have been clustered, and \cancel{E}_T computed, specific event topologies are explored. Several Level 3 triggers can be constructed which select events useful for the analysis of

⁵Silicon Graphics Power Servers.

different physics processes. Investigations involving bottom quarks often rely on the reconstruction of the J/ψ from two muons passing a trigger requiring two muons with low p_T . Level 3 triggers involving \cancel{E}_T criteria are useful in many searches for supersymmetric particles. The events which pass the Level 3 trigger are sent to specific data streams and stored. The data are written to 8mm tapes at a rate of approximately 5 Hz.

CHAPTER 4

DATA CONSTRUCTION AND REDUCTION

Four data samples were created in order to analyze event characteristics and ascertain the behavior of the underlying event. Commonly employed hardware and software triggers select information which is further fashioned by requirements designed to obtain unadulterated data reflective of the collision event. Detector regions and particle attributes were constrained to values in which reconstruction efficiency was high. Criteria utilized to purify the data possessed well understood systematic uncertainties.

Events were fully reconstructed and stored with information from several detector components. All samples included CTC measurements. Specialized algorithms used wire hits in the CTC and, when applicable, other tracking detectors to form particle tracks. Clusters of charged particles, identified by their associated tracks, traveling in the same direction were designated as charged particle jets. The charged particle jets or particles necessarily resulting from hard scattering collisions were used to determine angular correlations in the transverse plane.

The CTC records the passage of charged particle with a momentum resolution given by equation 3.13. Since the CTC efficiency can vary significantly in environments with low p_T tracks, the tracks were restricted to $p_T \geq 0.5$ GeV/c and $|\eta| \leq 1$. In this region, the CTC track reconstruction efficiency is stable and is estimated at 92% [79]. Dense, high p_T jets can also degrade CTC efficiency and therefore were limited to $p_{T(\text{jet1})} \leq 50$ GeV/c.

The overall event observables in the data samples were compared with results from QCD hard scattering models. Predictions must correctly describe the complete proton antiproton event structure to fit the global features. When comparing to theory, the data are not corrected for track finding efficiency. Instead, the theoretical predictions incorporate the track finding efficiency effects. These corrections are less than 10% and independent of track p_T and η in the selected regions.

All data samples include contamination from sources which obfuscate the study of the underlying event. Primary particles may interact with the detector material producing secondary particles. If admitted, these secondary particle tracks may be associated with identified vertices or cause vertices to be fabricated which were absent in the beam crossing. Inclusion of secondary particles corrupts the multiplicity, energy, and momentum ascribed to the event structure. Multiple proton antiproton interactions during the same bunch crossing also introduce obstacles when determining a unique hard scattering object in an event. These effects were reduced by selected tracks which were within 2 cm of the primary interaction vertex along the beam direction. Tracks were required to have impact parameters in the transverse plane calculated from CTC measurements, d_0^{CTC} , within 1 cm of the primary vertex. The contamination of the samples from spurious tracks was found to be $\sim 3.5\%$, with $\sim 9\%$ contamination if no d_0^{CTC} criterion was imposed [80].

4.1 Min-Bias Data

The minimum bias (Min-Bias) data sample is produced from one of the least restrictive sets of selection criteria and therefore represents an opportunity to investigate QCD phenomena over a broad range of transverse momenta without

Table 4.1: The Min-Bias data sample used in the analysis of the underlying event.

Sample	Trigger	Number of Events
Min-Bias	Coincident hits in the BBC	626,966

obscuring data due to trigger effects. The sample contains a mixture of diffractive and inelastic interactions arising from the beam collisions. The Min-Bias trigger required that at least one BBC coincidence, as defined in section 3.2.6, occur during a proton antiproton crossing. The trigger rate for Min-Bias events far exceeded the possible rate at which the information could be recorded necessitating a mechanism to reduce the number of selected events. In Run 1a, a prescale factor of 10^6 was employed with the purpose of storing only one of 10^6 acceptable events. Run 1b and 1c used dynamical prescales. In essence, the Min-Bias triggers for Run 1b and 1c were rate limited making the calculation of a luminosity for the sample extremely difficult. The data for the underlying event analysis originated from Run 1b and 1c. The characteristics of the sample are given in table 4.1.

Events and tracks are selected which provide a sample with a minimum contamination from impertinent sources. The Min-Bias data are required to contain zero or one vertex within $|z| < 100$ cm in order to be considered for further analysis. This criteria insures that events with multiple proton antiproton interactions are removed. If multiple proton antiproton interactions were included, the behavior of the underlying event would be difficult to characterize since the event structure would include components from different hard scattering processes and the number of tracks from spurious sources would increase. Tracks satisfying the requirements listed in table 4.2 are employed to construct charged particle jets and investigate

Table 4.2: Track selection criteria for the Min-Bias data sample.

$$\begin{aligned}
p_T^{\text{track}} &\geq 0.5 \text{ GeV}/c \\
|\eta_{\text{track}}| &\leq 1 \\
|d_0^{\text{CTC}}| &\leq 1 \text{ cm} \\
|z_c - z_v| &\leq 2 \text{ cm}
\end{aligned}$$

the behavior of the average charged particle multiplicity and scalar sum of transverse momentum. The variable z_c denotes the position along the z axis of the intercept between a charged particle track and the beam and z_v the position of the vertex along the z axis.

4.2 Jet20 Data

There are four dedicated jet triggers, each requiring different minimum energies registered in the calorimeters. Events are assigned to data samples which correspond to Level 2 E_T criteria (see section 3.2.7). For an event to be included in the Jet20 sample, at least one calorimeter cluster calculated at Level 2 must satisfy $E_T > 20$ GeV. The Jet50, Jet70, and Jet100 samples require cluster $E_T > 50$, 70, and 100 GeV, respectively. Since the E_T criteria result in an unacceptably high selection rate, the Jet20, Jet50, and Jet70 samples are prescaled¹ to accommodate the speed at which events can be recorded on 8mm tape. The Jet20 and Jet50 samples are prescaled at the Level 1 trigger, with Jet20 and Jet70 samples prescaled at the Level 2 trigger. No prescaling is required for the Jet100 sample. The prescaling factors of the various trigger sources are given in table 4.3.

¹Recall that prescaled triggers randomly select only a certain number of events from a total number that pass all other requirements. For instance, a trigger prescaled by a factor of 40 accepts one event from 40 which satisfied all other criteria.

Table 4.3: Level 1, Level 2, and combined prescaling factors for the Jet20, Jet50, Jet70, and Jet100 data samples.

Sample	Level 1 prescale	Level 2 prescale	Total prescale
Jet20	40	25	1000
Jet50	40	1	40
Jet70	1 (must pass calorimeter trigger)	8	8
Jet100	1	1	1

Table 4.4: The Jet20 data sample used in the analysis of the underlying event.

Sample	Trigger	Number of Events
Jet20	Calorimeter Tower cluster with $E_T > 20$ GeV	78.682

The characteristics of the Jet20 data sample used in the underlying event analysis are given in table 4.4. The event and charged particle track criteria were the same as for the Min-Bias data. Events with zero or one vertex within $|z| < 100$ cm were selected. The constraints of table 4.2 minimized tracks which did not arise directly from proton antiproton interactions.

The Min-Bias and Jet20 samples were combined to form the dijet sample.² Since the criteria employed to create the Jet20 sample satisfy the Min-Bias trigger, the data can be consolidated. A region of overlap between the two samples exists at $p_T(\text{jet1}) \sim 20$ GeV/c where the data connect smoothly in $p_T(\text{jet1})$. Together, the Min-Bias and Jet20 samples allow observables to be studied over the range $0.5 \leq p_T(\text{jet1}) \leq 50$ GeV/c.

²Although both samples do not explicitly trigger on two jets, the term dijet was chosen since the events which pass the selection criteria contained at least one charged particle jet, as defined in section 5.1, which must be balanced by another charged particle jet.

4.3 Z Boson Data

The Z boson data are constructed from the entire Run 1b stream A stored events. Three sets of selection criteria are applied to the raw data to form a sample with a high purity of Z candidates. The number of events in the stream A information is initially reduced by employing requirements which identify charged particles with the attributes of electrons. The resulting inclusive electron data sample is further refined by selecting events containing two electron candidates found using more stringent requirements. Once the loose Z sample is created, events containing particles consistent with Z bosons are retained to form the final Z data sample. Similar track selection criteria as in the Min-Bias and Jet20 samples are applied to the Z boson data.

The inclusive electron sample is derived from the Run 1b Stream A data stored on 131 DST tapes. All events are required to contain at least one candidate electron satisfying the criteria presented in table 4.5, regardless of the specific trigger used to select the original event. The variables employed in table 4.5 are designed to discriminate electrons from other charged particles (primarily hadrons and muons). Similar identification criteria were exploited in jet cluster finding [81] and have been utilized extensively in CDF analyses [73]. The Level 3 trigger algorithm matches reconstructed tracks with $p_T > 13$ GeV/c as determined by the CFT to calorimeter clusters with $E_T > 18$ GeV. The Level 2 inclusive electron trigger requires that the fraction of energy in the hadronic calorimeter towers behind the electromagnetic shower, E_{had} , to the measured cluster electromagnetic energy, E_{em} , be less than 0.125. Since trigger towers at Level 1 and 2 are larger than the physical dimensions of the calorimeter towers (see section 3.2.7), the $E_{\text{had}}/E_{\text{em}}$ ratio is applied over

Table 4.5: Selection criteria for the inclusive electron data sample.

For the central region:	
$E_T > 18 \text{ GeV}$	
$p_T > 13 \text{ GeV}/c$	
$E_{\text{had}}/E_{\text{em}} (3 \text{ tower}) < 0.125$	
$L_{\text{shr}} < 0.2$	
Track-CES matching: $ \Delta x < 5 \text{ cm}$	
Track-CES matching: $ \Delta z < 3 \text{ cm}$	
$\chi^2(\text{strip}) < 10$	

three adjacent calorimeter towers. The lateral sharing of a cluster's energy with several calorimeter towers, L_{shr} , compares the measured leakage from the seed tower to that expected from testbeam data for electrons. The distance between the extrapolated CTC track and the shower cluster position measured by the CES in mutually orthogonal coordinates x and z local to the strip chamber must be $|\Delta x| < 5 \text{ cm}$ and $|\Delta z| < 3 \text{ cm}$. The transverse profile of the shower in the CES is compared to expected shapes produced by testbeam electrons and the degree of correlation, χ^2 , determined. If a particle satisfied the criteria in table 4.5, the associated event was retained and entered into the inclusive electron data sample.

Inclusive electron data were purified by applying the requirements in table 4.6 to create a sample with high quality electron candidates used to reconstruct Z bosons. Particles crossing the fiducial area of the calorimeters yielded reliable energy measurements. The fiducial cut also ensured that effects due to calorimeter boundaries were suppressed. The calorimeter cluster energy, E , divided by the momentum of the corresponding track, P , provided a parameter to further distinguish electrons. The energy contribution of particles in proximity to the electrons was

Table 4.6: Selection criteria for the loose Z data sample.

Central ELES bank passing the tight cuts:	
Fiducial	
$E_T > 20 \text{ GeV}$	
$E_{\text{had}}/E_{\text{em}} < 0.05$	
$E/P < 1.8$	
$L_{\text{shr}} < 0.2$	
Track-CES matching: $ \Delta x < 1.5 \text{ cm}$	
Track-CES matching: $ \Delta z < 3.0 \text{ cm}$	
$\chi^2(\text{strip}) < 10$	
$ z_c - z_v < 5 \text{ cm}$	
$ z_v < 60 \text{ cm}$	
Calorimeter isolation cut:	
$I_{\text{cal}}/E_T(e) < 0.1$	

identified by determining the transverse energy in the calorimeter towers within a cone of $R = 0.4$ centered on the electron. By removing the electron's transverse energy, the calorimeter isolation variable, I_{cal} , was found. Electrons from apocryphal sources were reduced by imposing criteria on the distance between the z position of the interaction vertex, z_v , and the intercept between the reconstructed track and the z axis, z_c . The Z data sample consisted of events which contained one central electron candidate satisfying the restriction found in table 4.6 and another electron candidate with $E_T > 20/15/10$ for the central/plug/forward regions, respectively.

The selection criteria in table 4.6 have been extensively employed in previous CDF analyses to discern electrons from other particles [82, 83]. The discovery and investigation of top quarks involving semi-leptonic decays demanded accurate electron identification [73]. The requirements in table 4.6 are the same as those used in the top quark study, except for the E/P ratio. For high momentum

electrons, the electron mass can be neglected yielding a theoretical E/P value of approximately unity. The restriction of $E/P < 1.5$ in the top quark study was relaxed to $E/P < 1.8$ allowing a broader range of momenta. Although there was a greater possibility for misidentification of electrons and an increase in the number of events satisfying the requirements of table 4.6, the effect on the resultant data sample was minimal. Detailed discussion of reconstruction efficiencies can be found in the original top quark analysis [73].

Properties of the invariant mass distribution of the two leading electrons, $M(e^+e^-)$, and the pseudorapidity of the reconstructed Z boson, η_Z , were utilized to select Z candidates. The distribution of $M(e^+e^-)$ for the loose Z sample is shown in figure 4.1. Of the events in the loose Z sample, 20 have $M(e^+e^-) > 200$ GeV/c^2 . The value for the peak of the distribution is consistent with the mass of the Z boson. Constraining $M(e^+e^-)$ to be centered about the measured Z mass ($M(Z) = 91.187 \text{ GeV}/c^2$), the criterion

$$\left| M(Z) - M(e^+e^-) \right| \leq 10 \text{ GeV}/c^2, \quad (4.1)$$

eliminates events with either poorly resolved or no Z boson candidates. The shaded region in figure 4.1 indicates the $M(e^+e^-)$ range given by equation 4.1. The Z candidates at large pseudorapidity have low and unstable reconstruction efficiencies. This was resolved by accepting only Z bosons with $|\eta_Z| \leq 4$. In addition, events containing only single Z boson candidates were selected. The difference between the $M(e^+e^-)$ distributions for the loose Z sample and the data satisfying the Z specific criteria in figure 4.1 is due to the η_Z requirement. Approximately 80

events with appropriate invariant mass have reconstructed Z bosons that fail the pseudorapidity criterion.

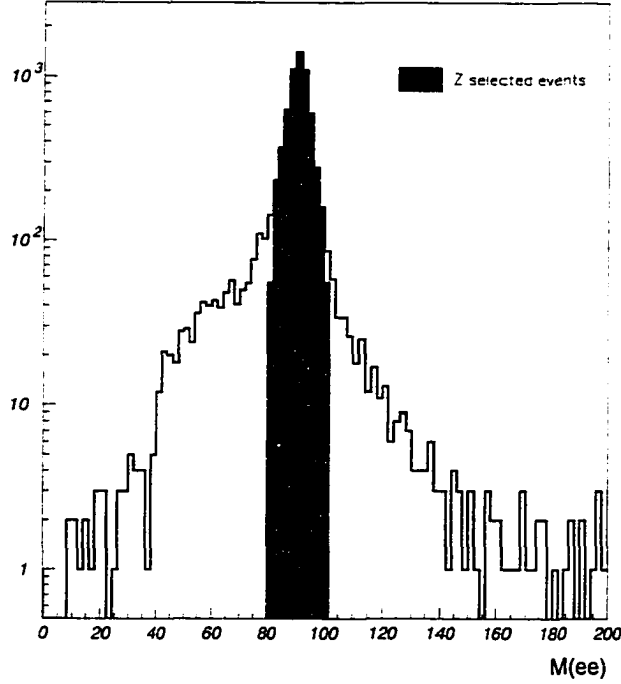


Figure 4.1: Histogram of the invariant mass distribution constructed from the two leading electrons. The shaded region corresponds to events with $|\eta_Z| \leq 4$ and $81.187 \leq M(e^+e^-) \leq 101.187 \text{ GeV}/c^2$.

Good tracks were selected using the requirements listed in table 4.7. Most of these criteria are the same as those used for the dijet sample. Since the specific decay mode $Z \rightarrow e^+e^-$ is employed, the products of the hard scattered particle can be eliminated from the event topology. Tracks arising from electrons identified as the daughters of the Z were removed from the events.

Table 4.7: Track selection criteria for the Z data sample.

$$\begin{aligned}
p_T^{\text{track}} &\geq 0.5 \text{ GeV/c} \\
|\eta_{\text{track}}| &\leq 1 \\
|d_0^{\text{CTC}}| &\leq 1 \text{ cm} \\
|z_c - z_v| &\leq 2 \text{ cm} \\
&\text{no electrons from } Z \text{ decay}
\end{aligned}$$

Table 4.8: Number of events satisfying the selection criteria used to create the Z sample.

Sample	Number of events
Inclusive electron sample	474,912
Loose Z sample	7412
Z sample after Z selection criteria	5005
Total after all selection criteria	4902

The number of events satisfying the selection requirements at successive stages is shown in table 4.8. The inclusive electron sample containing 474,912 events was refined to 4902 events. The corresponding efficiency to construct the Z boson data sample was 1.03%.

4.4 J/ψ B Data

The ability to clearly identify J/ψ particles decaying to two muons provides a discriminatory mechanism in the analyses of B meson events. Although the channel $J/\psi \rightarrow \mu^+ \mu^-$ occurs with a modest branching ratio of $6.01 \pm 0.19\%$ [22], a large quantity of data was collected because specific CDF triggers were designed for this distinctive signature. The canonical dimuon sample is often used by other investigations for such purposes as J/ψ polarization studies or cross-calibration

of various other samples. Access to approximately 970,000 dimuon events each consisting of an average 13 kbytes of information is facilitated by storage on 13 Gbytes of hard disk. The J/ψ B sample created for this study is derived from Run 1a and Run 1b data with a total integrated luminosity of $106.1 \pm 4.1 \text{ pb}^{-1}$.

The underlying event in processes involving B mesons was examined by employing the J/ψ as a reference. Characteristics of the J/ψ were selected which were consistent with production from the weak decay of a b to a c quark. An unfiltered dimuon sample will contain J/ψ particles from three production mechanisms.

1. direct production in which charm quarks are created in the proton antiproton collision and form J/ψ particles,
2. a feed down process where a more massive charmonium state such as χ_c or $\psi(2S)$ decays to a state with a J/ψ , and
3. B decay to final states including a J/ψ .

The hadrons with b quark components which can produce J/ψ particles include B^0 , B^\pm , B_s^0 , Λ_b , and their antiparticles.

These sources of J/ψ can be disentangled by determining whether the J/ψ vertex is primary or secondary. The primary vertex is indicative of the interaction between the constituents of the colliding hadrons. Extrapolated prompt particle tracks will originate at the primary vertex. Secondary vertices arise from particles created at the primary vertex which travel a detectable distance before they decay. When extended to the collision region, non-prompt tracks will reveal a secondary vertex which is displaced from the primary vertex. Figure 4.2 shows an illustration of primary and secondary vertices in the r - ϕ plane.

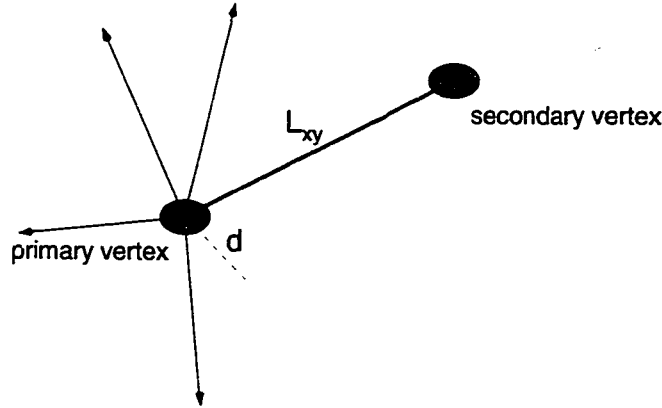


Figure 4.2: Illustration of an event in the r - ϕ plane with primary and secondary vertices. Lines with arrows represent particle tracks. The two dimensional distance between vertices is given by L_{xy} . The distance of closest approach to the primary vertex for extrapolated tracks is the impact parameter, d .

The J/ψ particles from B meson decay can be isolated from the other sources by differentiating between prompt and non-prompt J/ψ production. Direct and feed down production of J/ψ particles have associated tracks which appear at a primary interaction point. Since affiliated with the primary vertex, these sources are together categorized as prompt production mechanisms for J/ψ . A high momentum B meson created from the hadron collision will drift an appreciable distance since the B lifetime is approximately 1.5 psec [22]. The J/ψ particles arising from B decay will originate at displaced secondary vertices. By utilizing measurements of the displacement distance, a method for discriminating between J/ψ from prompt production and B decay can be formulated.

The techniques used to construct the J/ψ B data sample are similar to those used in previous CDF analyses [84, 85]. The former studies primarily attempted to ascertain particle properties such as measurement of B meson lifetimes and

J/ψ attributes. The dimuon data were employed in this investigation to create a sample of events containing J/ψ candidates arising from B decay. The effect on the underlying event due to the presence of heavy flavor physics was determined.

4.4.1 J/ψ Selection

Specific trigger paths produce data samples containing particles consistent with the properties of the J/ψ . Dimuon triggers are implemented at Level 1 and 2 and identify events with at least two high quality muon candidates. Wire hits within the CMU and CMX muon chambers are employed to reconstruct tracks. To avoid confusion with tracks determined from CTC measurements, the tracks in the CMU and CMX are denoted as muon stubs. The sensitivity to detect particles traversing the muon chambers is degraded by ionization energy losses in the central calorimeter. In order to reach the CMU, a muon must have $p_T \gtrsim 1.4$ GeV/c. The Level 3 trigger accepts data which satisfy Level 1 and 2 requirements and analyzes the events for features specific to J/ψ particles.

Basic pattern matching and kinematical restrictions performed by the Level 2 dimuon trigger allow events with two muon candidates to be identified. Tracks within the CTC are reconstructed by the CFT in the r - ϕ plane. These tracks are extended to the muon chambers where they are matched to muon stubs. The criteria for the difference in ϕ between extrapolated track and stub was originally $\Delta\phi \leq 15^\circ$. Early in Run 1b this angular requirement was lowered to $\Delta\phi \leq 5^\circ$. Events with at least one match between track and muon stub were selected. In addition, the presence of one or more CFT tracks was required during Run 1a. whereas for Run 1b this criteria was increased to two or more CFT tracks. Energy

Table 4.9: CDF Level 2 dimuon triggers.

Level 2 trigger	minimum muon p_T	Run
TWO_CMU_ONE_CFT	one > 2.7 , other > 1.7	1a
TWO_CMU_TWO_CFT	both > 2.0	1b
TWO_CMU_CMU_ONE_CFT_3.4	one > 2.9 , other > 1.7	1b
TWO_CMU_ONE_CFT_2.2_6TOW	both > 2.0	1b

loss of the muons, multiple interactions, and production of secondary particles all conspire to limit the lower bound of the momentum which can be reliably measured in the muon chambers. To insure that the trigger efficiencies are well understood while permitting a broad range of transverse momentum values, the CDF dimuon triggers typically record muon candidates with $p_T \geq 2.0$ GeV/c. The dimuon trigger name, the minimum p_T necessary for a muon candidate to be accepted, and the CDF run in which the trigger was utilized are listed in table 4.9. For $p_T \gtrsim 3.0$ GeV/c, the muon trigger efficiencies are high and stable at greater than 90% [86].

A Level 3 trigger used by CDF has been specifically designed to select dimuon events compatible with production from J/ψ decay. Candidate J/ψ particles are formed from two candidate muons, μ_1 and μ_2 , and subjected to criteria derived from known J/ψ characteristics. Events with an invariant mass of the two muons, $M(\mu_1\mu_2)$, in a range about the measured J/ψ mass of 3.09688 GeV/c² are selected [22]. In Run 1a, $M(\mu_1\mu_2)$ was constrained to

$$2.8 \leq M(\mu_1\mu_2) \leq 3.4 \text{ GeV}/c^2$$

with μ_1 and μ_2 of opposite charge. For Run 1b, the charge criteria of the candidate muons was removed and the invariant mass required to be in the interval

$$2.7 \leq M(\mu_1\mu_2) \leq 4.1 \text{ GeV}/c^2 .$$

The Level 3 dimuon trigger also employed more stringent pattern matching restrictions. An associated standard deviation is calculated by combining the multiple scattering and various measurement uncertainties. In Run 1a, a track and stub matched if the difference in their positions was less than four standard deviations. This criteria was lowered in Run 1b to three standard deviations. An event satisfying the Level 3 trigger requirements is stored on 8mm tape for further offline event reconstruction.

The J/ψ data sample must be refined by verifying that events do not include detector and instrumentation induced errors. The trigger, tracking, and calorimeter systems are required to be functioning normally. Events from Run 1a in which the bunch crossing time was poorly measured are omitted. Run 1b data where the CFT did not account for the gravitational wire sag in the tracking systems are also removed by the quality criteria. An accurate determination of the beam position from the SVX for each run and storage of this information in a database are required [87].

4.4.2 Event Selection

The J/ψ data sample can be separated into components which arise either from prompt or B decay production by employing the pseudo-proper decay length.

ct . To calculate ct , the vector from the primary to secondary vertex, defined as $\vec{r} = \vec{x}_{\text{sec}} - \vec{x}_{\text{prim}}$, and the transverse decay length, L_{xy} , must be determined in the r - ϕ plane. The position of the primary vertex, \vec{x}_{prim} , is replaced by the measured beam position. The transverse decay length provides a measure of the displacement between primary and secondary vertices and is calculated by projecting \vec{r} onto a particle's transverse momentum,

$$L_{xy} = \frac{\vec{r} \cdot \vec{p}_T}{|\vec{p}_T|} . \quad (4.2)$$

Possible negative values for L_{xy} are nonsensically interpreted as events in which a particle decayed before it was created. Fortunately, such values of L_{xy} are within the resolution of a Gaussian distribution centered on $L_{xy} = 0$ representing promptly produced (no lifetime) particles. For particles with decay lifetimes, the transverse decay length is expected to be positive. The proper decay time can be calculated from L_{xy} and provides the time for a particle to decay in its own rest frame. The distribution of proper decay times for J/ψ particles produced from B mesons should be that of an exponential decay with B meson lifetime as time constant. A proper decay length can be determined for fully reconstructed B mesons by

$$(ct)_{\text{proper}}^B = \frac{L_{xy}^B m_B}{p_T^B} ,$$

where L_{xy}^B , m_B , and p_T^B correspond to the B meson specific transverse decay length from equation 4.2, mass, and transverse momentum, respectively. Since the reconstruction efficiency is low for B mesons, the proper decay length is approximated by the pseudo-proper decay length which uses the J/ψ measurements. Monte

Carlo simulations indicate that the angular difference between J/ψ and B meson directions is on average 7.6° and the momentum of the J/ψ is on average greater than 70% of the B meson momentum [84]. Substituting J/ψ parameters for those of the B meson, the pseudo-proper decay length is written as

$$ct = \frac{L_{xy}^{J/\psi} m_{J/\psi}}{F_{\text{corr}} p_T^{J/\psi}}$$

with F_{corr} a correction factor parameterizing the effect of using J/ψ instead of B measurements. The correction factor is momentum dependent and determined to be

$$F_{\text{corr}}(p_T^{J/\psi}) = 2.44 \exp(-1.18 p_T^{J/\psi}) + 0.84$$

from Monte Carlo simulation of $B \rightarrow J/\psi X$ events [84].

Figure 4.3 shows the pseudo-proper decay length distributions for the fitted prompt and B decay signals of the J/ψ . The distributions are normalized to the same scale permitting overall features of the data sample to be discerned. The prompt signal appears as a Gaussian with width indicative of the pseudo-proper decay length resolution. The distribution produced from B decay exhibits the behavior of a displaced exponential decay. The point at which the two distributions intersect, $ct = 0.013$ cm, can be employed to differentiate between short and long lived processes.

In order to suppress the contribution from prompt production of J/ψ particles, the selection criteria in table 4.10 are applied. The pseudo-proper decay length can only be reliably calculated if the impact parameter of the muons is accurately

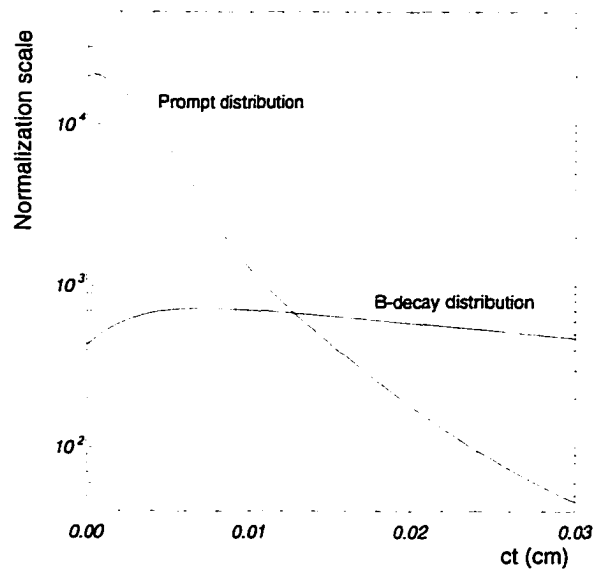


Figure 4.3: Pseudo-proper decay length distributions for prompt and B decay produced J/ψ . Both distributions are normalized to the same scale.

Table 4.10: Selection criteria which form a data sample containing J/ψ candidates predominately from B decay.

$$\begin{array}{l} \text{Both } J/\psi \text{ } \mu\text{'s found in SVX and CTC or} \\ 1 \text{ } J/\psi \text{ } \mu \text{ found in SVX and CTC and other in CTC only} \\ ct \geq 0.03 \end{array}$$

determined. Precision measurements are available for those muon candidates arising from J/ψ decay which produce a good hit pattern in the SVX. A good hit pattern is defined as three or four hits in the SVX which are not shared with other tracks. Once muon candidates incorporating SVX information are found, the pseudo-proper decay length can be utilized to discriminate between prompt and B decay production. By requiring $ct \geq 0.03$, the data is reduced to a high purity sample of B events in which the mesons decayed to J/ψ and other particles. Contamination of the sample due to prompt J/ψ production is less than 10%.

The data is further reduced by the requirements in table 4.11. Occasionally, two or more J/ψ particles are reconstructed in a single event. To insure that the underlying event can be investigated with reference to a unique J/ψ , each event must contain one reconstructed J/ψ particle. The pseudorapidity of the J/ψ is restricted to the central region providing an overlap with the η used for the underlying event analysis. Requiring the z position of the J/ψ decay vertex to be within 60 cm of the detector's center maintains the projective tower geometry of the calorimeters and insures that the interaction occurs in the fiducial volume. Muons identified as the decay products of the J/ψ must cross either the CMU or CMX chambers. Since the muon chambers are located at $|\eta| \leq 1$, the pseudorapidity of the J/ψ muons, $\eta^{\mu(J/\psi)}$, is restricted to the same range. The J/ψ muons with

Table 4.11: Selection criteria to create a data sample containing J/ψ candidates with high efficiency in the CTC and characteristics appropriate to the underlying event analysis.

$$\begin{aligned}
 N_{J/\psi} &= 1 \\
 |\eta_{J/\psi}| &\leq 1 \\
 |z_{J/\psi}| &\leq 60 \text{ cm} \\
 p_T^{\mu(J/\psi)} &\geq 2 \text{ GeV}/c \\
 |\eta^{\mu(J/\psi)}| &\leq 1
 \end{aligned}$$

transverse momentum, $p_T^{\mu(J/\psi)}$, sufficiently large are capable of penetrating through the calorimeters and can be reconstructed efficiently.

The requirements given in table 4.2 are employed to select tracks with high CTC efficiency. Unlike the Z sample in which the tracks of the Z decay products were removed, the tracks corresponding to muons originating from the J/ψ are treated in two distinct fashions. When topologies are examined as a function of the leading charged particle jet, the data includes the J/ψ muons. For the analysis of event structures with reference to the J/ψ particle, the J/ψ muons are excluded from the sample. After all selections are applied to the data, 30,445 events remain.

CHAPTER 5

DATA ANALYSIS TECHNIQUES

Several unique data analysis techniques are employed in this analysis which must be described and verified. These techniques include a non-standard definition of charged jets, the segregation of the azimuthal angle ϕ into regions towards, transverse, and away from the hard scattered object, and the determination of systematic uncertainties which are applied to the data. The towards, transverse, and away regions are shown to have characteristic behaviors which are presumed to arise from the dominance of different processes in the event.

The removal of events from the data sample due to selection criteria or detector component capabilities can be parameterized by the efficiency, ϵ . The efficiency is defined as

$$\epsilon = \frac{\text{Number of events passing selection}}{\text{Total number of events}} \times 100\% \quad (5.1)$$

and is a measure of the number of signal events remaining after the selection criteria are applied. A result of $\epsilon = 0\%$ would indicate that the selection criteria removed all signal events, whereas $\epsilon = 100\%$ would reflect that no signal events were removed. The efficacy of the criteria listed in section 4 to purify the data samples can be described by calculating their corresponding efficiencies.

When comparing theoretical calculations with experimental data, the capabilities of the detector components must be incorporated. Since this analysis relies

primarily on central tracking chamber measurements, the efficiency of the CTC to measure charged particle tracks is studied. In order to avoid regions where the efficiency either varies substantially or decreases dramatically due to low transverse momentum tracks, the tracks are restricted to $p_T \geq 0.5 \text{ GeV}/c$ and $|\eta| \leq 1$ where the CTC efficiency is high and stable. Another source of loss in track information arises from high transverse momentum jets in which the tracks in the jet may be densely packed. This reduction in efficiency is avoided by requiring $p_T(\text{jet1}) \leq 50 \text{ GeV}/c$ for the charged particle jets. Monte-Carlo studies have shown that for these criteria the probability that the CTC finds a charged track is roughly constant at 92%.

Experimental data and Monte Carlo predictions can be compared once corrections are applied to either the data or the predictions and both are subjected to the same selection criteria. The data presented in this analysis are uncorrected. Instead, the theoretical predictions are corrected for the track finding efficiency by removing 8% of the charged tracks. The Monte Carlo generated events are required to satisfy the selection criteria used for either the Min-Bias, Jet20, Z boson, or J/ψ B data sets given in section 4. The total uncertainties for the theoretical predictions and the data are determined by adding in quadrature the statistical and systematic uncertainties. The corrected theoretical predictions have a combined uncertainty of approximately 5%.

The techniques used to examine the average charged multiplicity and average scalar sum of transverse momentum and to determine the data's systematic uncertainty are developed in the following sections.

5.1 Jet Definitions

Jets are defined as momentum flow into circular regions of η - ϕ space with radius $R = \sqrt{(\Delta\eta)^2 + (\Delta\phi)^2}$. Charged particle jets consist of only charged particles arising from sources such as the underlying event and the fragmentation of high p_T outgoing partons. A simple jet definition is adopted since occasionally jets that contain a few low p_T charged particles will be found. The algorithm employed for the analysis of the underlying event assigns every charged particle in an event to a jet, with the possibility that some jets may contain a single charged particle. The charged particle jet algorithm is implemented as follows:

- all charged particles in an event are ordered according to their p_T .
- the highest p_T charged particle is selected and all charged particles within the radius $R = 0.7$ are included in the jet (the charged particles are considered in order of decreasing p_T with the jet centroid recalculated for each charged particle incorporated into the jet),
- the next highest p_T charged particle which has not been assigned to a jet is selected and all charged particles not already in a jet within $R = 0.7$ are included,
- the procedure continues until all charged particles are in a jet.

All charged particles with $p_T \geq 0.5$ GeV/c and $|\eta| \leq 1$ are considered. Portions of the jets are allowed to extend past the pseudorapidity range $|\eta| \leq 1$. The transverse momentum of the i th jet, $p_T(j_i^{\text{chg}})$, is calculated as the scalar p_T sum of all charged particles within the jet. Some observable quantities depend on the

specific jet definition and the algorithm used to construct the jets. Therefore, the same technique to determine charged particle jets is applied to both the theoretical predictions and the experimental data.

Two primary distinctions exist between the jet definition above and those used in other analyses. The charged particle jet definition given earlier produces infrared divergences if applied at the parton level. Subsequently, theoretical grounds exist which do not favor this prescription. However the objection is not relevant when examining information from collider events since all observable quantities at the hadron level must be infrared stable. The identification of particle jets in the central tracking chamber is uncommon. Typically, CDF jet definitions utilize the energy deposition in the calorimeter system to form tower clusters. These tower cluster measurements are input into various algorithms which determine the characteristics of the jets [88].

5.2 $\Delta\phi$ Correlations

In order to investigate the characteristics of the overall event structure, the plane transverse to the beam axis is partitioned into three regions according to the relative difference in azimuthal angle between charged particle tracks and the direction of the object assumed to arise from a hard scattering event. For the Min-Bias, Jet20, and J/ψ B data samples, angles are determined relative to the direction of the transverse momentum of the leading jet, $p_T(\text{jet1})$. For the Z boson and J/ψ B data samples, the direction of the reconstructed particle's transverse momentum is employed to determine the angular differences.

The regions fixed by the direction of the hard scattered object are sensitive to different sources of particle production. Specific behavior can be isolated by defining regions toward, transverse, and away from the hard scattered object. The toward region contains the hard scattered object and particles arising from the break up of the proton and antiproton, initial state gluon radiation, and final state gluon radiation. The transverse region isolates the particles arising from the fragments of the original proton and antiproton system, initial state gluon radiation, and possible multiple parton scattering. The underlying event is most easily studied in the transverse region. The away region is composed of underlying event, the hard scattering jet which balances the hard scattering jet in the toward region, final state gluon radiation. Occasionally, the hard scattered away side object is outside the pseudorapidity range $|\eta| \leq 1$ and therefore not included. This results in a greater role for the underlying event in the away region than the toward. Figure 5.1 illustrates these angular regions.

The angular differences between the hard scattered object and the charged particle track, $\Delta\phi = \phi(\text{hard scattered object}) - \phi(\text{track})$, varies from -180° to 180° . The toward region is defined as

$$|\Delta\phi| \leq 60^\circ, \quad (5.2)$$

the transverse region as

$$60^\circ < |\Delta\phi| \leq 120^\circ, \quad (5.3)$$

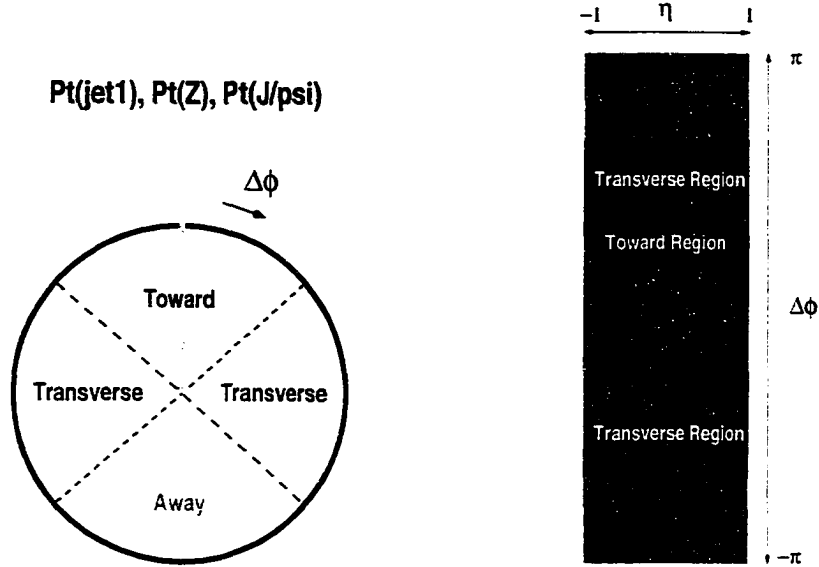


Figure 5.1: Toward, away, and transverse regions for azimuthal angles in the plane perpendicular to the beam axis (left). With $|\eta| \leq 1$, each of these three regions corresponds to an area of $4\pi/3$ in η - ϕ space (right).

and the away region as

$$|\Delta\phi| > 120^\circ . \quad (5.4)$$

Since the charged particle pseudorapidity cuts limit us to $|\eta| \leq 1$, any one of these regions in η - ϕ space has an area of $4\pi/3$.

The justification for the specific choices of angles for the toward, transverse, and away regions given in equations 5.2, 5.3, and 5.4 is motivated through the examination of the average charged multiplicity, $\langle N_{\text{chg}} \rangle$, and average scalar sum of the transverse momentum, $\langle \sum p_T^{\text{chg}} \rangle$, as a function of the hard scattering object in sections 5.2.1, 5.2.2, and 5.2.3. For the analyses involving leading transverse momentum jets, the toward region includes particles from the leading jet as well

as particles from the underlying event. In the Z boson and J/ψ B analyses, the decay products of the Z and J/ψ are explicitly excluded resulting in the toward region being a direct measure of the underlying event. The data for the $\langle N_{\text{chg}} \rangle$ and $\langle \sum p_T^{\text{chg}} \rangle$ distributions in azimuthal angle $\Delta\phi$ relative to the hard scattered object is examined for the two requirements $p_T(\text{hard scattered object}) \geq 5 \text{ GeV}/c$ and $30 \text{ GeV}/c$.

5.2.1 Angular Correlations in Min-Bias and Jet20 Data

In order to insure that equations 5.2, 5.3, and 5.4 isolate specific features in the average charged multiplicity and average scalar sum of transverse momentum, the Min-Bias and Jet20 data are examined with respect to the angular differences between the charged tracks and the leading charged jet. The effect of the transverse momentum of the leading charged jet on the event structure is investigated by requiring $p_T(\text{jet1}) \geq 5 \text{ GeV}/c$ for the Min-Bias data and $p_T(\text{jet1}) \geq 30 \text{ GeV}/c$ for the Jet20 data. The data presented in figures 5.2, 5.3, 5.4, and 5.5 include the tracks from the leading charged jet in the towards region. The angular bin size used in figures 5.2, 5.3, 5.4, and 5.5 is 3.6° .

Figures 5.2 and 5.3 present the average charged multiplicity and average scalar sum of the transverse momentum as a function of $|\Delta\phi|$ for $p_T(\text{jet1}) \geq 5 \text{ GeV}/c$. The average charged multiplicity decreases dramatically in the towards region as the angular difference between the charged jet direction and the tracks increases. A drop in the charged particle multiplicity occurs near $|\Delta\phi| = 35^\circ$ followed by an abrupt increase and subsequent approximate constant values for larger $|\Delta\phi|$ values. This feature is a consequence of employing a particular cone size for the

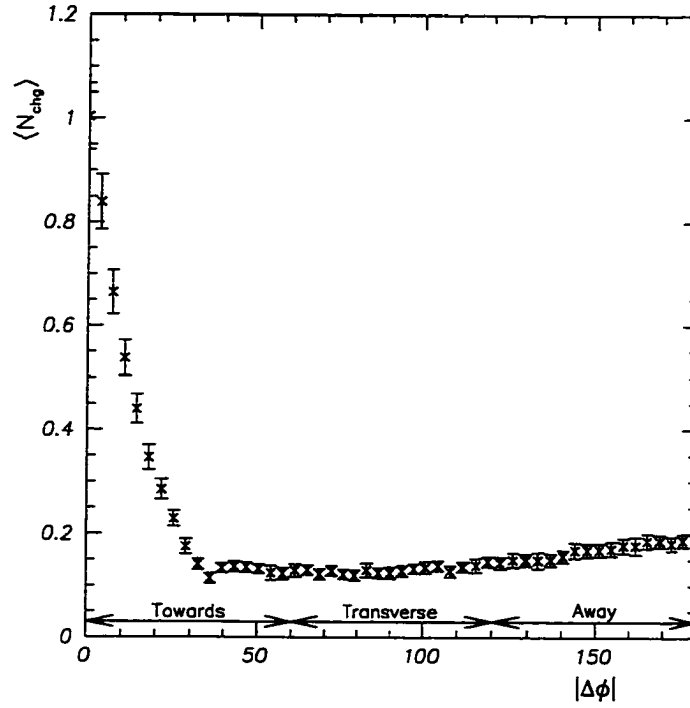


Figure 5.2: The average charged multiplicity as a function of the angles between the leading jet and the tracks for $p_T(\text{jet1}) \geq 5$. The angular bin size is 3.6° . Indicated are the towards, transverse, and away regions as defined in equations 5.2, 5.3, and 5.4, respectively. The leading jet tracks are included in the towards direction.

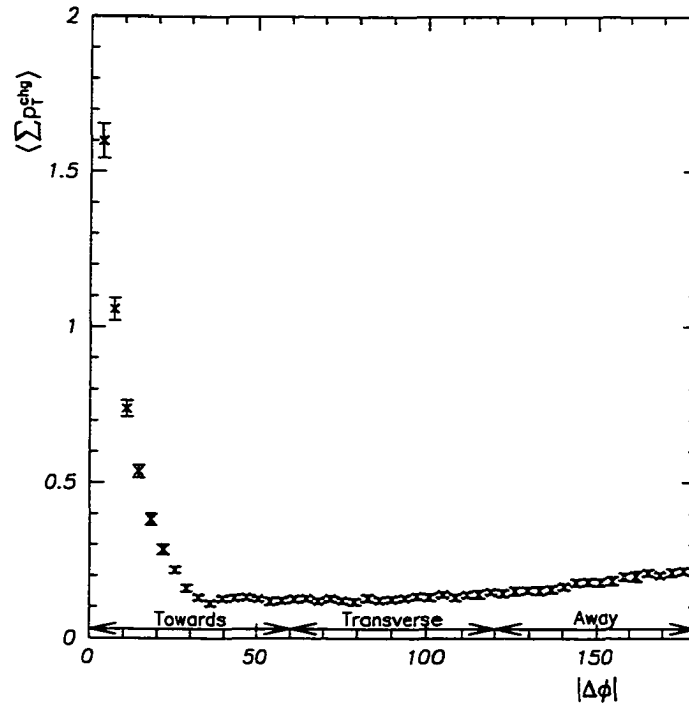


Figure 5.3: The average scalar sum of transverse momentum as a function of the angles between the leading jet and the tracks for $p_T(\text{jet1}) \geq 5$. The angular bin size is 3.6° . Indicated are the towards, transverse, and away regions as defined in equations 5.2, 5.3, and 5.4, respectively. The leading jet tracks are included in the towards direction.

jet definition. For the charged particle jets used in this analysis, $R = 0.7$. The overall behavior in the towards region reflects the higher multiplicity of the leading charged jet and particles which appear near the leading charged jet. The data in the transverse region of the average charged multiplicity is approximately constant at 0.13 with a slight rise for larger values of $|\Delta\phi|$. The rate of increase in average charged multiplicity grows modestly for data in the away region. The average scalar sum of the transverse momentum as a function of $|\Delta\phi|$ displayed in 5.2 exhibits the same behavior as that for the average charged multiplicity. However, for small values of $|\Delta\phi|$, the average scalar sum of transverse momentum rises more steeply than for the average charged multiplicity indicating that the particles near the center of a jet have higher transverse momentum than particles further from the center. The data in the towards, transverse, and away regions show distinct behavior for the average charged multiplicity and average scalar sum of transverse momentum. Separating these regions by the angular requirements of equations 5.2, 5.3, and 5.4 allows the isolation of specific features.

The data in figures 5.4 and 5.5 are obtained when restricting the transverse momentum of the leading charged jet to $p_T(\text{jet1}) \geq 30 \text{ GeV}/c$. The behavior in the towards and transverse regions of the average charged multiplicity and average scalar sum of transverse momentum is qualitatively similar to what was found for the $p_T(\text{jet1}) \geq 5 \text{ GeV}/c$ restriction. The differences between the $p_T(\text{jet1}) \geq 5 \text{ GeV}/c$ and $p_T(\text{jet1}) \geq 30 \text{ GeV}/c$ data are confined to the slightly increased growth in average charged multiplicity and average scalar sum of the transverse momentum at small $|\Delta\phi|$ in the towards region and large $|\Delta\phi|$ in the transverse region for the $p_T(\text{jet1}) \geq 30 \text{ GeV}/c$ data. In comparison to the $p_T(\text{jet1}) \geq 5$

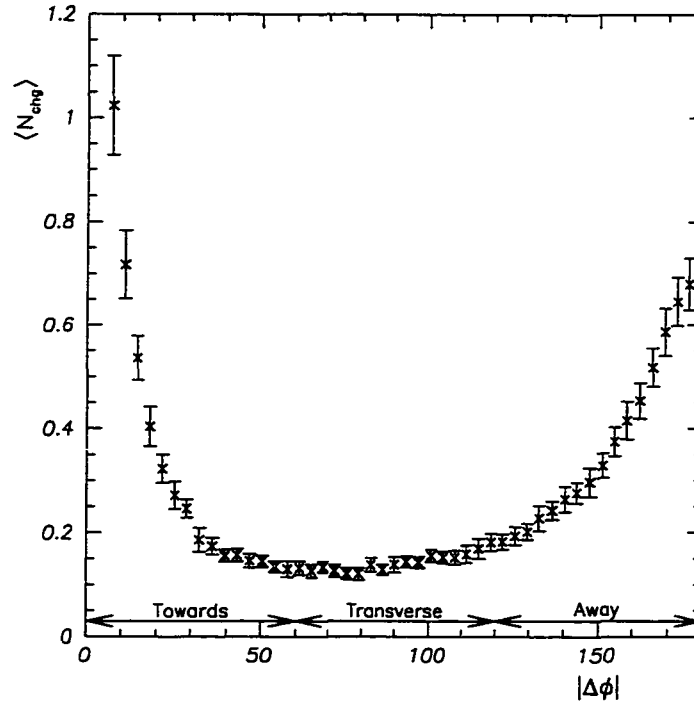


Figure 5.4: The average charged multiplicity as a function of the angles between the leading jet and the tracks for $p_T(\text{jet1}) \geq 30$. The angular bin size is 3.6° . Indicated are the towards, transverse, and away regions as defined in equations 5.2, 5.3, and 5.4, respectively. The leading jet tracks are included in the towards direction.

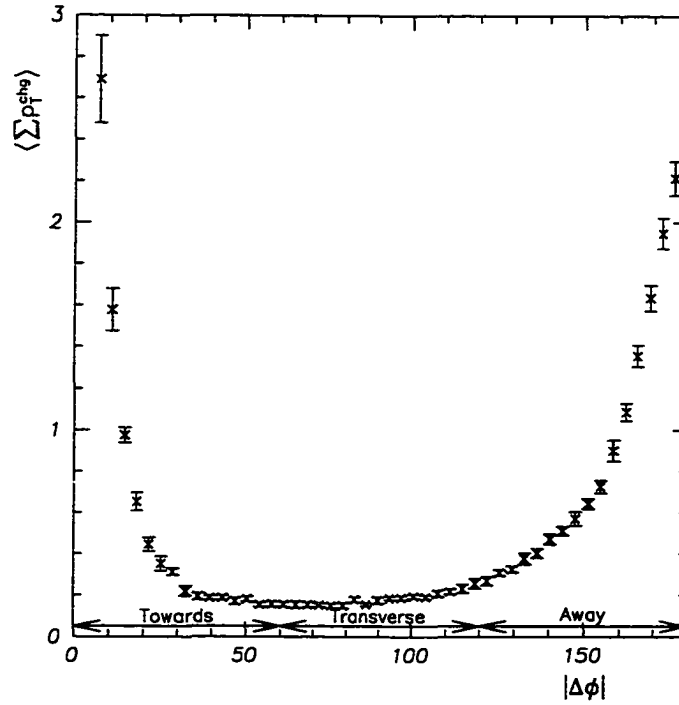


Figure 5.5: The average scalar sum of transverse momentum as a function of the angles between the leading jet and the tracks for $p_T(\text{jet1}) \geq 30$. The angular bin size is 3.6° . Indicated are the towards, transverse, and away regions as defined in equations 5.2, 5.3, and 5.4, respectively. The leading jet tracks are included in the towards direction.

GeV/c data, the $p_T(\text{jet1}) \geq 30$ GeV/c data in the away region are dramatically different. The average charged multiplicity and average scalar sum of transverse momentum rise steeply for increasing $|\Delta\phi|$. The rise is reminiscent of the increase in the towards region for smaller $|\Delta\phi|$, only in the away region the rise is less steep and the growth occurs over a greater region of $|\Delta\phi|$. The average scalar sum of the transverse momentum grows more rapidly than the average charged multiplicity as $|\Delta\phi|$ increases indicating that the particles further from the leading charged jet are contributing more to the total transverse momentum in the away region. This feature in the away region is due to the away side jet arising from an outgoing hard scattered parton. To satisfy higher transverse momentum requirements of the leading charged jet, the hard scattered parton which gives rise to the leading charged jet must also have a higher transverse momentum. A hard scattered parton with the same transverse momentum but opposite direction must be present to balance the interaction.

The values of the angular differences in equations 5.2, 5.3, and 5.4 are appropriate for isolating specific behavior of the data presented in 5.2, 5.3, 5.4, and 5.5, for the Min-Bias and Jet20 samples. The leading charged jet and features associated with the selection of the particular jet size are fully contained in the region of $|\Delta\phi| \leq 60^\circ$. The data in the transverse region are approximately constant with a slight rise for larger values of $|\Delta\phi|$. The effects of the away side jet and associated particle production most clearly seen in figures 5.4 and 5.5 can be distinguished from the transverse region at approximately $|\Delta\phi| = 120^\circ$. Therefore, the definitions of the towards, transverse, and away regions in equations 5.2, 5.3, and 5.4, respectively, are applicable to the Min-Bias and Jet20 data.

5.2.2 Angular Correlations in Z Data

The Z boson data is examined to verify the validity of segregating regions of the transverse plane around the Z boson according to equations 5.2, 5.3, and 5.4. The behavior of the average charged particle multiplicity and the average scalar sum of the transverse momentum must be consistent in each of the regions, otherwise attempting to describe a region as representative of the underlying event or of the away side jet would be meaningless. In addition, the proper values of the angular cuts which isolate a particular behavior need to be determined for the Z boson data.

The decay products of the Z have been removed from the data presented in figures 5.6, 5.7, 5.8, and 5.9. This produces a towards region that, like the transverse region, should be dominated by the effects of the underlying event. The angular bin size used in figures 5.6, 5.7, 5.8, and 5.9 is 3.6° .

When requiring $p_T(Z) \geq 5 \text{ GeV}/c$, the data obtained for the average charged multiplicity and average scalar sum of the transverse momentum as a function of $|\Delta\phi|$ are shown in figures 5.6 and 5.7. For the average charged multiplicity in the towards region, the data is approximately constant with a value of 0.15. A slight rise in average charged multiplicity occurs for progressively larger values of the angular difference in the transverse region. The away region is characterized by a dramatic rise in the average charged multiplicity. Similar features in the towards and transverse region occur for the average scalar sum of the transverse momentum. The data in the away region show a more pronounced rate of increase for the average scalar sum of the transverse momentum when compared to the average charged multiplicity. There is a clear differentiation between the behavior found

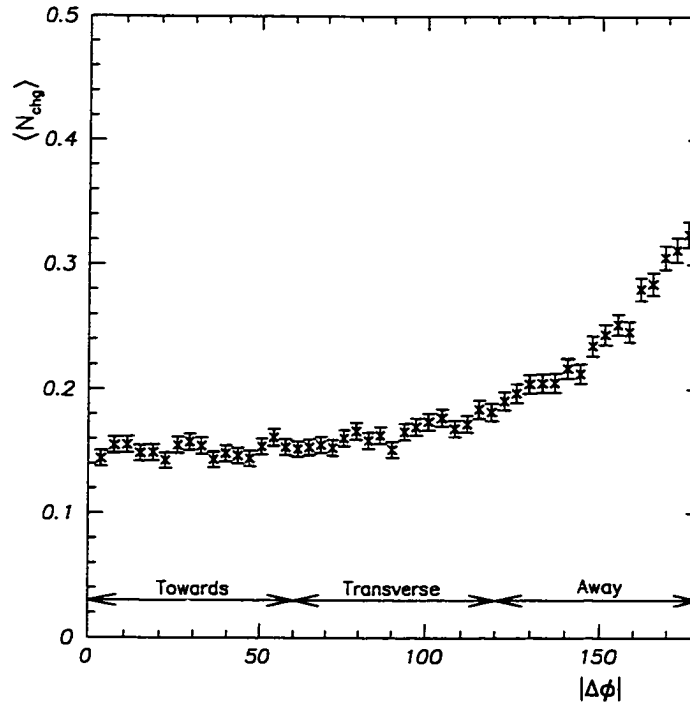


Figure 5.6: The average charged multiplicity as a function of the angles between the Z boson and the tracks for $p_T(Z) \geq 5$. The angular bin size is 3.6° . Indicated are the towards, transverse, and away regions as defined in equations 5.2, 5.3, and 5.4, respectively. The Z boson decay products have been removed.

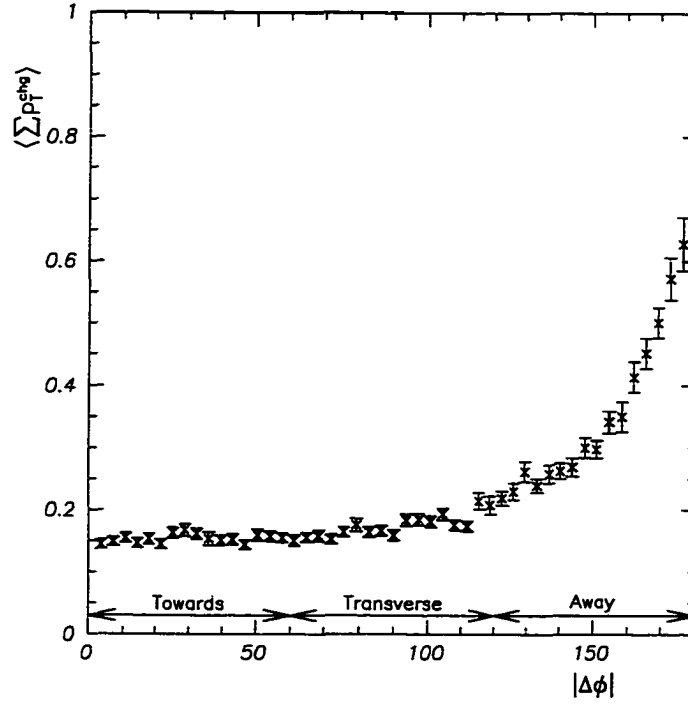


Figure 5.7: The average scalar sum of transverse momentum as a function of the angles between the Z boson and the tracks for $p_T(Z) \geq 5$. The angular bin size is 3.6° . Indicated are the towards, transverse, and away regions as defined in equations 5.2, 5.3, and 5.4, respectively. The Z boson decay products have been removed.

in the towards and away regions, with a transition between the two given by the transverse region. On the basis of the data presented in figures 5.6 and 5.7 no exact demarcation in the angular cuts can be made. The average charged multiplicity and average scalar sum of transverse momentum do show specific behavior as a function of $|\Delta\phi|$ and can qualitatively be separated into towards, transverse, and away regions.

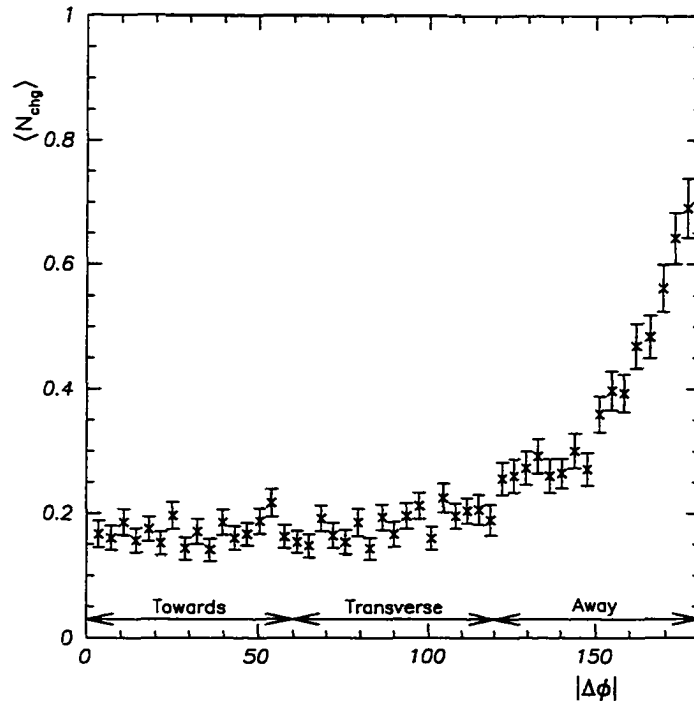


Figure 5.8: The average charged multiplicity as a function of the angles between the Z boson and the tracks for $p_T(Z) \geq 30$. The angular bin size is 3.6° . Indicated are the towards, transverse, and away regions as defined in equations 5.2, 5.3, and 5.4, respectively. The Z boson decay products have been removed.

Upon increasing the transverse momentum requirement of the Z boson to $p_T(Z) \geq 30$ GeV/c, the distinction between transverse and away regions becomes

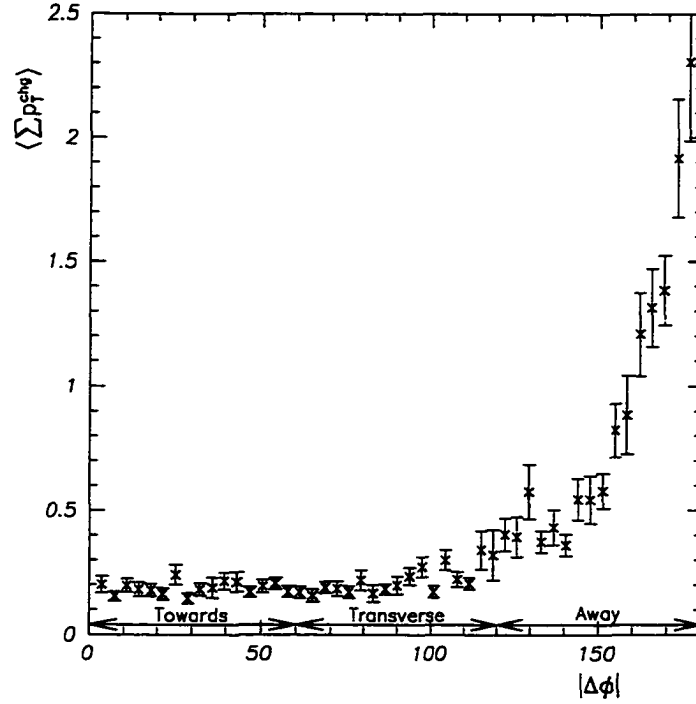


Figure 5.9: The average scalar sum of transverse momentum as a function of the angles between the Z boson and the tracks for $p_T(Z) \geq 30$. The angular bin size is 3.6° . Indicated are the towards, transverse, and away regions as defined in equations 5.2, 5.3, and 5.4, respectively. The Z boson decay products have been removed.

apparent. The data are presented in figures 5.8 and 5.9. As for $p_T(Z) \geq 5 \text{ GeV}/c$, the data in figures 5.8 and 5.9 corresponding to the towards region have an approximately constant value. The transverse region of the average charged multiplicity also displays an approximately constant value over $|\Delta\phi|$. The average scalar sum of the transverse momentum grows slightly in the transverse region as $|\Delta\phi|$ increases. A distinct increase in average charged multiplicity and average scalar sum of the transverse momentum occurs in the away region. The onset of the change in behavior between transverse and away regions occurs approximately at 120° .

The data in figures 5.6, 5.7, 5.8, and 5.9 clearly show that different behaviors exist for different regions in $|\Delta\phi|$. Figures 5.6 and 5.7 indicate that a separation between towards and transverse can be established at approximately $|\Delta\phi| = 60^\circ$ where the constant value of the data in the towards region changes to a slowly rising behavior in the transverse. The transverse and away regions can be separated at approximately $|\Delta\phi| = 120^\circ$ as shown in figures 5.8 and 5.9 where the constant value of the transverse region changes to steeply rising values in the away region. Therefore, the use of equations 5.2, 5.3, and 5.4 to define towards, transverse, and away regions is applicable to the Z boson data.

5.2.3 Angular Correlations in J/ψ B Data

Figures 5.10, 5.11, 5.12, and 5.13 show the distribution of $\langle N_{\text{chg}} \rangle$ and $\langle \sum p_T^{\text{chg}} \rangle$ in $|\Delta\phi|$ with the direction of the hard scattering object given by the transverse momentum of the leading jet. The effect of utilizing a particular jet size is demonstrated in the data for $p_T(\text{jet1}) \geq 5 \text{ GeV}/c$ by the feature observed at $|\Delta\phi| \lesssim 35^\circ$. The leading jet will primarily arise from the decay constituents of the B meson.

While the J/ψ and other B products ordinarily are contained within the same jet, lower momentum leading jets often consist of an incomplete set of B remnants. The behavior of $\langle N_{\text{chg}} \rangle$ and $\langle \sum p_T^{\text{chg}} \rangle$ for $p_T(\text{jet1}) \geq 5 \text{ GeV}/c$ in the range $35^\circ \lesssim |\Delta\phi| \lesssim 50^\circ$ is most likely produced by a contribution from B decay. The distributions in the transverse region for figures 5.10, 5.11, 5.12, and 5.13 show approximately constant values, with the away region demonstrating attributes consistent with the presence of away side jets.

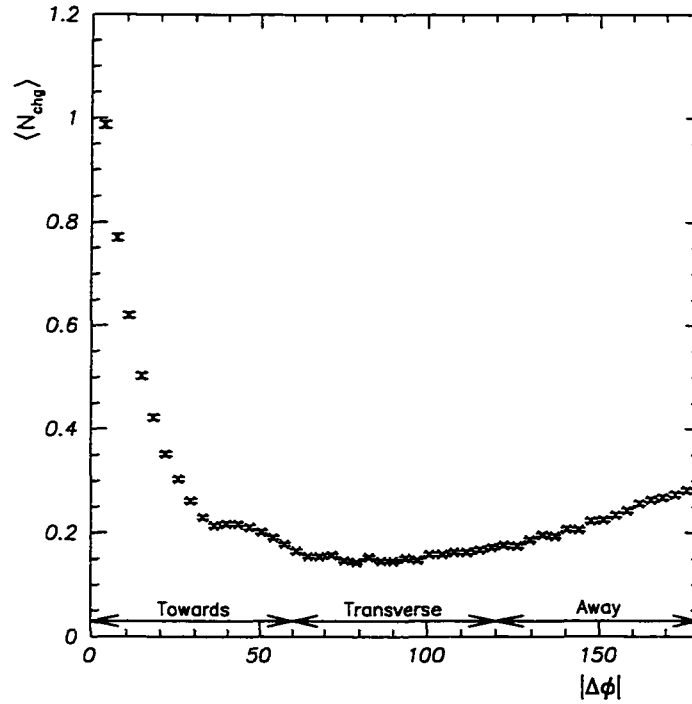


Figure 5.10: The average charged multiplicity as a function of the angles between the leading jet and the tracks for $p_T(\text{jet1}) \geq 5$. The angular bin size is 3.6° . Indicated are the towards, transverse, and away regions as defined in equations 5.2, 5.3, and 5.4, respectively. The leading jet tracks are included in the towards direction.

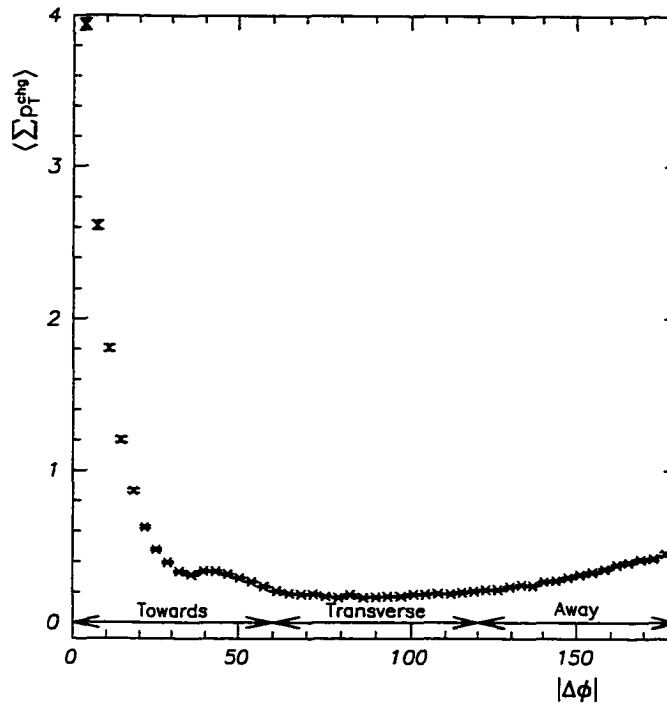


Figure 5.11: The average scalar sum of transverse momentum as a function of the angles between the leading jet and the tracks for $p_T(\text{jet1}) \geq 5$. The angular bin size is 3.6° . Indicated are the towards, transverse, and away regions as defined in equations 5.2, 5.3, and 5.4, respectively. The leading jet tracks are included in the towards direction.

Figures 5.14, 5.15, 5.16, and 5.17 show the distribution of $\langle N_{\text{chg}} \rangle$ and $\langle \sum p_T^{\text{chg}} \rangle$ in $|\Delta\phi|$ with the direction of the hard scattering object given by the transverse momentum of the J/ψ . The limited number of reconstructed J/ψ particles with $p_T(J/\psi) \geq 30$ GeV/c causes the data in figures 5.16 and 5.17 to be highly unreliable. Fortunately, the data for figures 5.14 and 5.15 contain sufficient statistics. Although the muons arising from J/ψ decay have been eliminated, the toward region contains average charged multiplicities and scalar p_T sums which obscure

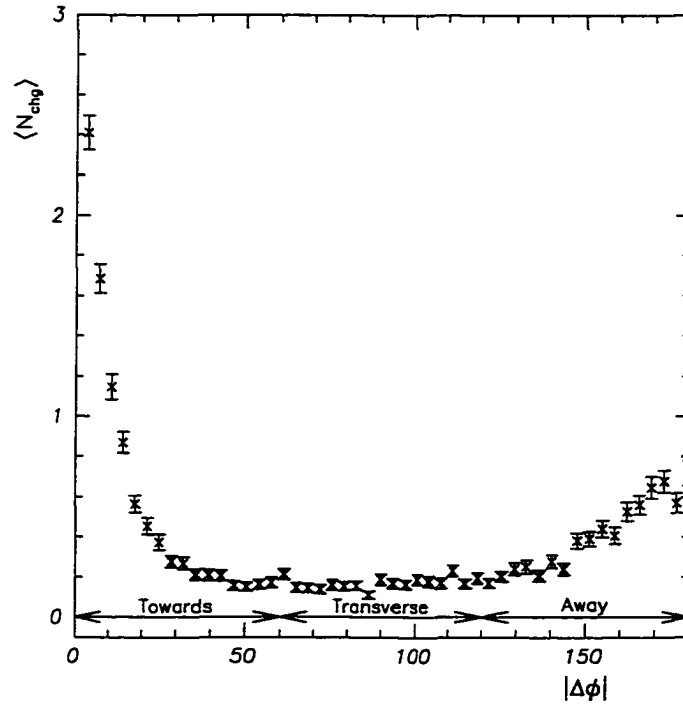


Figure 5.12: The average charged multiplicity as a function of the angles between the leading jet and the tracks for $p_T(\text{jet1}) \geq 30$. The angular bin size is 3.6° . Indicated are the towards, transverse, and away regions as defined in equations 5.2, 5.3, and 5.4, respectively. The leading jet tracks are included in the towards direction.

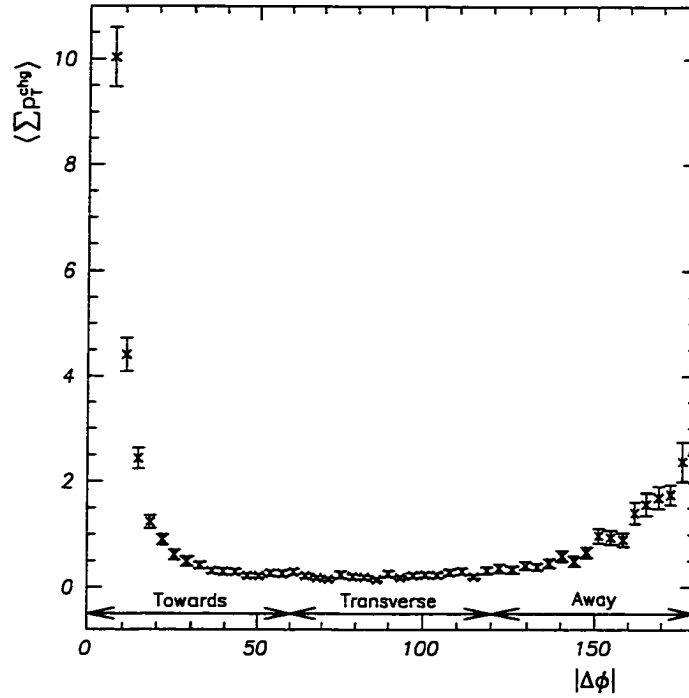


Figure 5.13: The average scalar sum of transverse momentum as a function of the angles between the leading jet and the tracks for $p_T(\text{jet1}) \geq 30$. The angular bin size is 3.6° . Indicated are the towards, transverse, and away regions as defined in equations 5.2, 5.3, and 5.4, respectively. The leading jet tracks are included in the towards direction.

examination of the underlying event. The B meson which creates the J/ψ also produces associated particles which will appear in the toward region. Unlike for the Z boson, removing the decay products does not insure extraction of the hard scattering component. Figures 5.14 and 5.15 demonstrate unique behaviors for transverse and away regions. The transverse region has a roughly uniform distribution for $60^\circ \leq p_T(J/\psi) \leq 120^\circ$. At higher angular differences, $\langle N_{\text{chg}} \rangle$ and $\langle \sum p_T^{\text{chg}} \rangle$ increase due to the particles created to balance the interaction.

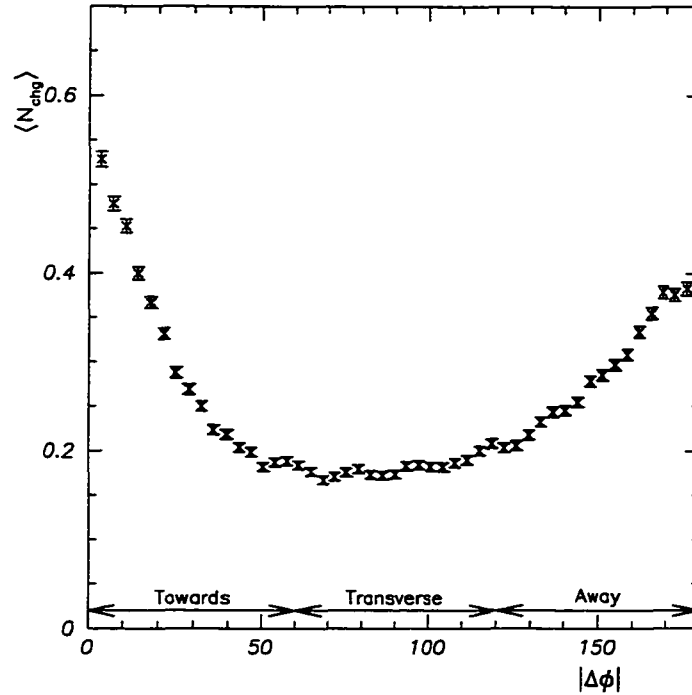


Figure 5.14: The average charged multiplicity as a function of the angles between the J/ψ and the tracks for $p_T(J/\psi) \geq 5$. The angular bin size is 3.6° . Indicated are the towards, transverse, and away regions as defined in equations 5.2, 5.3, and 5.4, respectively. The J/ψ decay products have been removed.

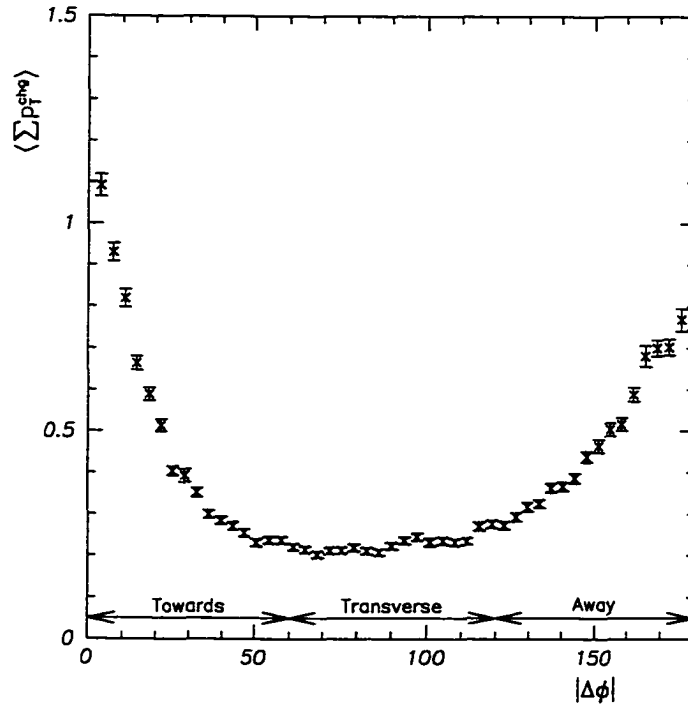


Figure 5.15: The average scalar sum of transverse momentum as a function of the angles between the J/ψ and the tracks for $p_T(J/\psi) \geq 5$. The angular bin size is 3.6° . Indicated are the towards, transverse, and away regions as defined in equations 5.2, 5.3, and 5.4, respectively. The J/ψ decay products have been removed.

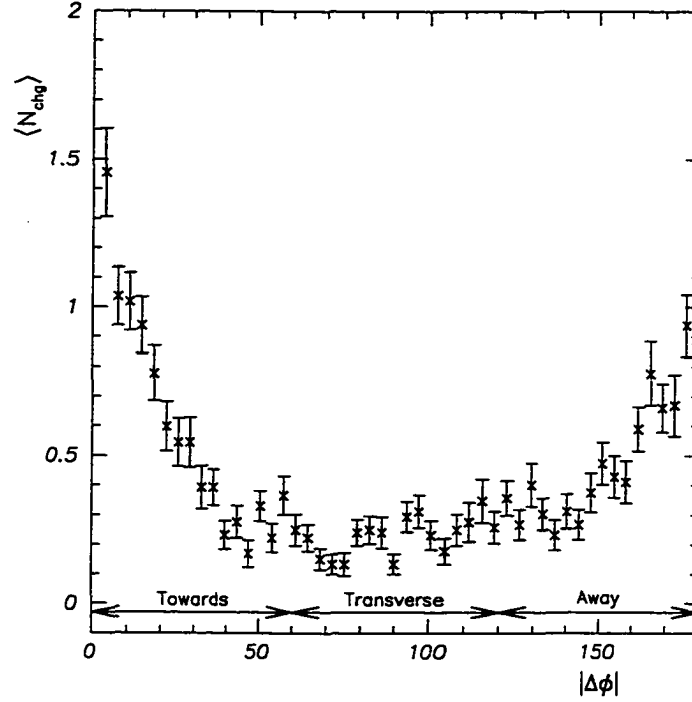


Figure 5.16: The average charged multiplicity as a function of the angles between the J/ψ and the tracks for $p_T(J/\psi) \geq 30$. The angular bin size is 3.6° . Indicated are the towards, transverse, and away regions as defined in equations 5.2, 5.3. and 5.4, respectively. The J/ψ decay products have been removed.

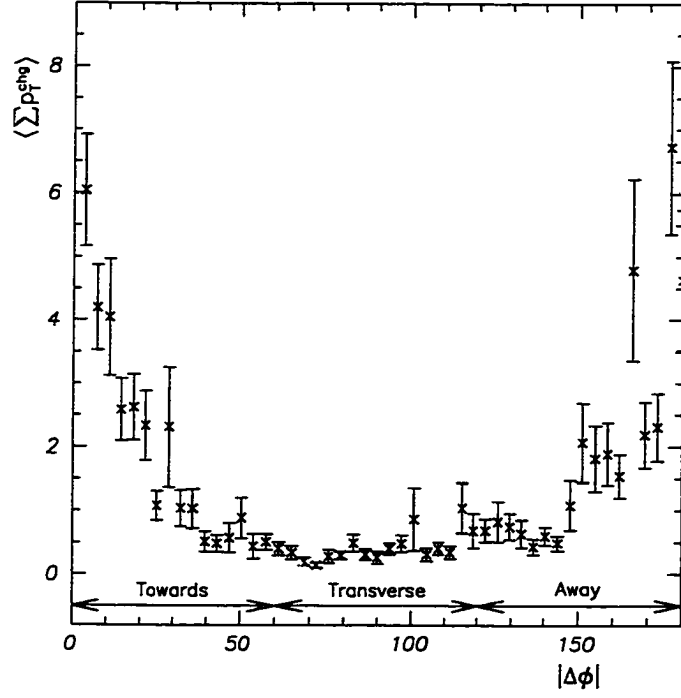


Figure 5.17: The average scalar sum of transverse momentum as a function of the angles between the J/ψ and the tracks for $p_T(J/\psi) \geq 30$. The angular bin size is 3.6° . Indicated are the towards, transverse, and away regions as defined in equations 5.2, 5.3, and 5.4, respectively. The J/ψ decay products have been removed.

5.3 Systematics

The value of the impact parameter cut was found to strongly affect the number of fake tracks in the data samples of Reference [80]. Similarly, the dominant systematic error is assumed to come from this source and denoted as ϵ_{ip} . For each data point, the systematic error is calculated by

$$\epsilon_{ip} = \frac{P|P_2 - P_1|}{P_1}, \quad (5.5)$$

where P corresponds to a data point with $d_0 \leq 1$ cm, P_1 the same data point with $d_0 \leq 0.5$ cm, and P_2 the same data point with no d_0 cut. To determine the total error, the systematic and statistical errors are added in quadrature. Unless otherwise stated, the errors on the data include both statistical and systematic uncertainties. The theory curves have a total error of around 5%.

CHAPTER 6

EVENT STRUCTURE

Structures in events with hard scattering collisions can be discerned by analyzing angular regions about an identified hard scattered object. The direction of the leading charged jet, Z boson, and J/ψ transverse momenta are utilized to define toward ($|\Delta\phi| \leq 60^\circ$), transverse ($60^\circ < |\Delta\phi| \leq 120^\circ$), and away ($|\Delta\phi| > 120^\circ$) azimuthal ranges. Charged particle tracks with $p_T \geq 0.5$ GeV/c and $|\eta| \leq 1$ are selected for the determination of average charged particle multiplicity, $\langle N_{\text{chg}} \rangle$, and average scalar p_T sum of charged particles, $\langle \sum p_T^{\text{chg}} \rangle$. Specific features of the event structure are isolated with the transverse region most sensitive to contributions from the underlying event.

6.1 Event Structure in Dijet Data

The leading charged jet in dijet events is employed to form angular correlations which are used to calculate $\langle N_{\text{chg}} \rangle$ and $\langle \sum p_T^{\text{chg}} \rangle$. While events were not required to contain a minimum of two identified jets, the Min-Bias and Jet20 samples resulting from the criteria described in sections 4.1 and 4.2 are collectively denoted as the dijet sample. Charged particles from the leading charged jet were included in the toward region. The results presented in this section are the subject of a recent publication describing the overall event structure and underlying event in dijet data [41].

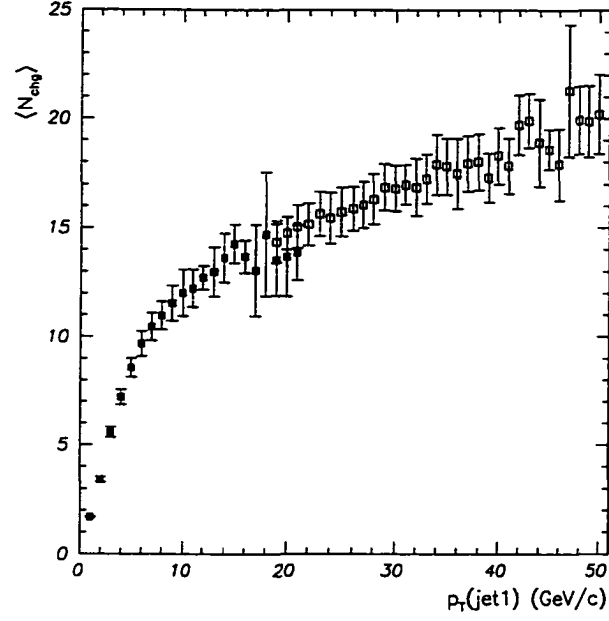


Figure 6.1: Dijet data for the average number of charged particles as a function of the transverse momentum of the leading charged jet. The contribution from the leading charged jet is included. The solid and open boxes represent data from the Min-Bias and Jet20 samples, respectively. The bin size in $p_T(\text{jet1})$ is 1 GeV/c. The uncertainty for the uncorrected data points combines statistical and correlated systematic uncertainties.

The average charged particle multiplicity as a function of the transverse momentum of the leading charged jet, $p_T(\text{jet1})$, is shown in figure 6.1. The sources of the data are denoted in the figure by solid and open points corresponding to the Min-Bias and Jet20 samples, respectively. An overlap between the two samples exists for $19 \leq p_T(\text{jet1}) \leq 21$ GeV/c where the data are found to be consistent with one another. This congruity along with the realization that events in the Jet20 sample will satisfy the Min-Bias trigger allows the full range $0.5 \leq p_T(\text{jet1}) \leq 50$ GeV/c to be investigated. The data in figure 6.1 show a sharp rise in the overall $\langle N_{\text{chg}} \rangle$ for leading charged jets up to a transverse momentum of 8 GeV/c. For higher $p_T(\text{jet1})$, the $\langle N_{\text{chg}} \rangle$ increases more gradually. The approach of $\langle N_{\text{chg}} \rangle$ to zero as $p_T(\text{jet1})$ decreases is a reflection of lower activity in the event. The jet finding algorithm described in section 5.1 guaranteed that if an event contained any charged particles, a jet could be found. Consequently, if $p_T(\text{jet1}) = 0$ GeV/c, no particles satisfying the selection requirements were recorded.

Figure 6.2 shows the average charged particle multiplicity as a function of $p_T(\text{jet1})$ in the toward, away, and transverse regions. Since the leading charged jet is included in $\langle N_{\text{chg}} \rangle$, the toward region will contain particles from the outgoing hard scattering jet. The toward region also receives additional contributions from the underlying event. The inclusion of the leading charged jet is clearly responsible for the toward $\langle N_{\text{chg}} \rangle$ dominating the overall $\langle N_{\text{chg}} \rangle$ measurement. The toward $\langle N_{\text{chg}} \rangle$ is greater than that in the away and transverse regions combined. In comparison to the other regions, the toward $\langle N_{\text{chg}} \rangle$ for $p_T(\text{jet1}) \leq 10$ GeV/c rises most rapidly. The growth in the toward $\langle N_{\text{chg}} \rangle$ moderates for higher momenta and can be approximated by a linear function. The away region contains both a hard scat-

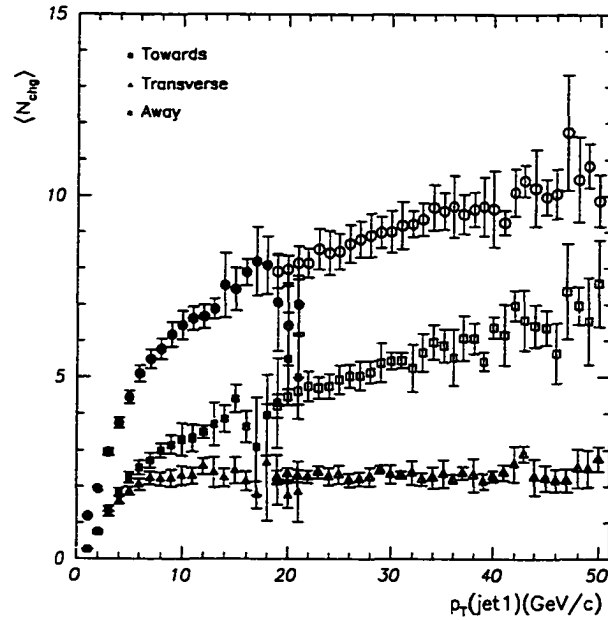


Figure 6.2: Dijet data for the average number of toward, away, and transverse charged particles as a function of the transverse momentum of the leading charged jet. The contribution from the leading charged jet is included. The solid and open boxes represent data from the Min-Bias and Jet20 samples, respectively. The bin size in $p_T(\text{jet1})$ is 1 GeV/c. The uncertainty for the uncorrected data points combines statistical and correlated systematic uncertainties.

tering jet which balances the jet in the toward direction and a contribution from the underlying event.¹ While the away $\langle N_{\text{chg}} \rangle$ rises dramatically for $p_T(\text{jet1}) \leq 10$ GeV/c, the reduction in growth near 10 GeV/c occurs earlier and more severely than for the toward $\langle N_{\text{chg}} \rangle$. When $p_T(\text{jet1}) > 10$ GeV/c, the rate of increase in away $\langle N_{\text{chg}} \rangle$ matches that observed in the towards region. The difference between the toward and away $\langle N_{\text{chg}} \rangle$ for $p_T(\text{jet1}) > 10$ GeV/c is approximately constant at 3.5 charged particles. The transverse $\langle N_{\text{chg}} \rangle$ rises quickly for $p_T \leq 6$ GeV/c, more than doubling when $p_T(\text{jet1})$ increases from 1 to 2 GeV/c. A stable plateau with an approximate value of 2.2 charged particles exists for $p_T(\text{jet1}) > 6$ GeV/c. Even as the transverse momentum of the leading charged jet increases by a factor of 5, the transverse $\langle N_{\text{chg}} \rangle$ remains roughly constant. This indicates that the contribution of the underlying event to the overall average charged particle multiplicity is stable as the hard scattering interaction increases in energy.

The average scalar p_T sum of the charged particles in the toward, away, and transverse regions is shown in figure 6.3. The toward $\langle \sum p_T^{\text{chg}} \rangle$ grows rapidly when $p_T(\text{jet1}) < 10$ GeV/c, approaching a linear function of $p_T(\text{jet1})$ at larger momenta. For $p_T(\text{jet1}) \geq 10$ GeV/c, the toward $\langle \sum p_T^{\text{chg}} \rangle$ is principally determined by the leading charged jet and can be approximated using

$$\left\langle \sum p_T^{\text{chg}} \right\rangle = p_T(\text{jet1}) + 1.4 .$$

The away and transverse $\langle \sum p_T^{\text{chg}} \rangle$ are roughly identical in the regime $p_T(\text{jet1}) \leq 6$ GeV/c. When $p_T(\text{jet1}) > 6$ GeV/c, the away $\langle \sum p_T^{\text{chg}} \rangle$ rises in a linear fashion as

¹The appearance of a second jet originally inspired the use of the terminology dijet to describe both Min-Bias and Jet20 samples.

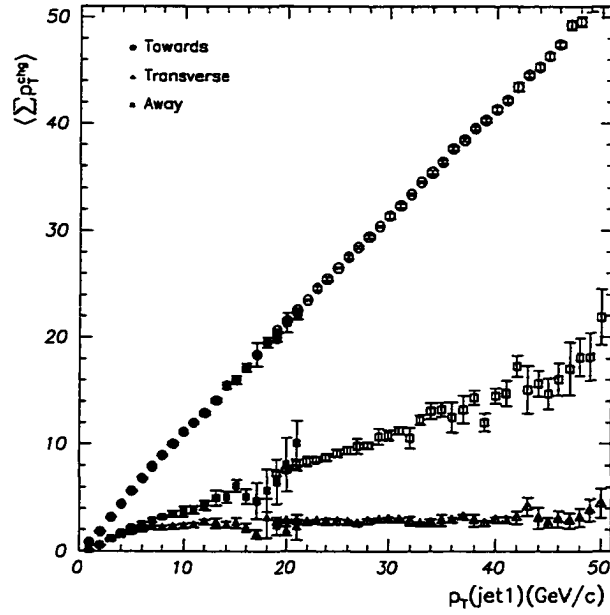


Figure 6.3: Dijet data for the average scalar p_T sum of toward, away, and transverse charged particles as a function of the transverse momentum of the leading charged jet. The contribution from the leading charged jet is included. The solid and open boxes represent data from the Min-Bias and Jet20 samples, respectively. The bin size in $p_T(\text{jet1})$ is 1 GeV/c. The uncertainty for the uncorrected data points combines statistical and correlated systematic uncertainties.

$p_T(\text{jet1})$ increases with a lower slope than that of the toward region. The transverse $\langle \sum p_T^{\text{chg}} \rangle$ values form a plateau at $p_T(\text{jet1}) > 6 \text{ GeV}/c$ with an approximately constant value of $2.8 \text{ GeV}/c$. In this momentum range, the behavior of the average scalar p_T sum associated with the underlying event exhibits no dependence on the transverse momentum of the hard scattering jet.

6.1.1 The Dijet Transverse Region: Theory and Data

The average charged multiplicity and scalar p_T sum from the dijet sample in figures 6.1, 6.2, and 6.3 are compared with theoretical predictions. The Monte Carlo models of HERWIG 5.9, ISAJET 7.32, and PYTHIA 6.115 are employed to calculate QCD hard scattering interactions in collisions of protons and antiprotons at 1.8 TeV. Parameters in the models which describe characteristics of the collision process are set to the default values of the Monte Carlo generators. The hard scattering transverse momentum of the partons is required to be $p_T^{\text{hard}} > 3 \text{ GeV}/c$. The 92% CTC track finding efficiency is incorporated into the theoretical predictions.

Figure 6.4 shows the predictions of HERWIG, ISAJET, and PYTHIA compared with dijet data for the average charged multiplicity as a function of the leading charged jet transverse momentum. All of the Monte Carlo generators produce too many charged particles on average for $p_T(\text{jet1}) < 5 \text{ GeV}/c$. While HERWIG is in accord with the majority of data, the overall shape of the generated $\langle N_{\text{chg}} \rangle$ distribution exhibits a discrepancy with observational values. The average multiplicity is too low in the interval $5 < p_T(\text{jet1}) < 16 \text{ GeV}/c$ with a rising trend that creates too many charged particles for $p_T(\text{jet1}) > 35 \text{ GeV}/c$. The $\langle N_{\text{chg}} \rangle$ predicted

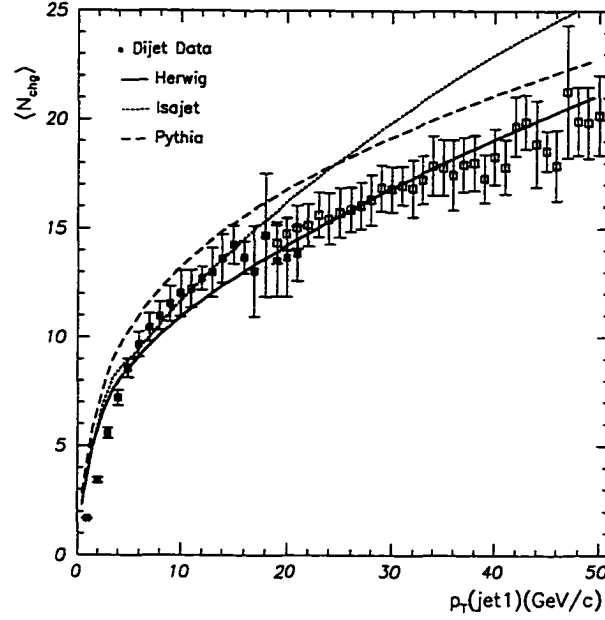


Figure 6.4: Comparison between dijet data and theoretical predictions for the average number of charged particles as a function of $p_T(\text{jet1})$. The contribution from the leading charged jet is included. The solid and open boxes represent data in 1 GeV/c bins from the Min-Bias and Jet20 samples, respectively. The theoretical predictions are generated by the QCD hard scattering models of HERWIG, ISAJET, and PYTHIA and have been corrected for the CTC efficiency. The uncertainty for the uncorrected data points combines statistical and correlated systematic uncertainties.

by ISAJET increases too rapidly as the leading charged jet momentum grows. If the rate of change in $\langle N_{\text{chg}} \rangle$ decreased as $p_T(\text{jet1}) > 16 \text{ GeV}/c$, ISAJET could describe the data more accurately. Instead, large differences between the theoretical predictions and experimental observations occur for $p_T(\text{jet1}) > 24 \text{ GeV}/c$. The general shape of the $\langle N_{\text{chg}} \rangle$ distribution as a function of $p_T(\text{jet1})$ produced by PYTHIA agrees with that found in the data. Unfortunately, the predicted $\langle N_{\text{chg}} \rangle$ is consistently too large by an average of approximately 2 charged particles.

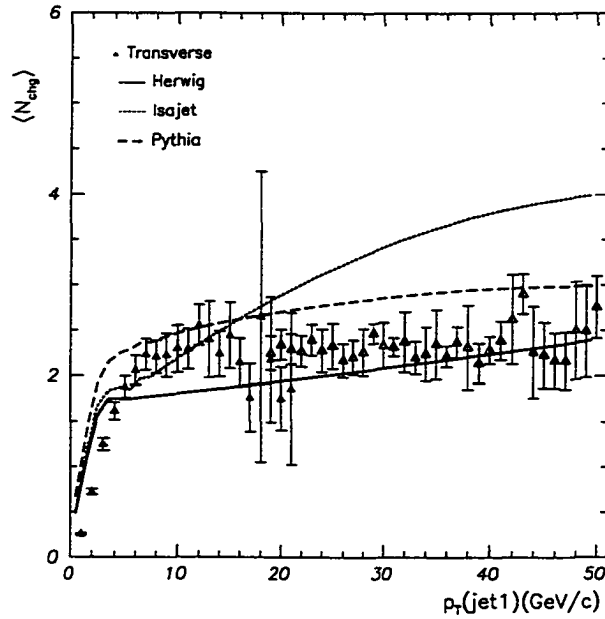


Figure 6.5: Comparison between dijet data and theoretical predictions in the transverse region for the average number of charged particles as a function of $p_T(\text{jet1})$. The contribution from the leading charged jet is included. The solid and open triangles represent data in $1 \text{ GeV}/c$ bins from the Min-Bias and Jet20 samples, respectively. The theoretical predictions are generated by the QCD hard scattering models of HERWIG, ISAJET, and PYTHIA and have been corrected for the CTC efficiency. The uncertainty for the uncorrected data points combines statistical and correlated systematic uncertainties.

The predictions and data for $\langle N_{\text{chg}} \rangle$ in the transverse region as a function of the leading charged jet momentum are shown in figure 6.5. The $\langle N_{\text{chg}} \rangle$ produced from the Monte Carlo generators rises rapidly for $p_T(\text{jet1}) \lesssim 3 \text{ GeV}/c$. At $p_T(\text{jet1}) \simeq 3 \text{ GeV}/c$, the growth of average charged multiplicity produced by HERWIG and ISAJET decreases drastically. The results from HERWIG are constant until $p_T(\text{jet1}) \simeq 6 \text{ GeV}/c$, after which $\langle N_{\text{chg}} \rangle$ gradually increases in a linear fashion with respect to $p_T(\text{jet1})$. On the whole, the $\langle N_{\text{chg}} \rangle$ distribution created by HERWIG underestimates much of the data and has a shape which does not match observations. The $\langle N_{\text{chg}} \rangle$ from ISAJET also changes at $p_T(\text{jet1}) \simeq 6 \text{ GeV}/c$ from an approximately constant value to predictions which increase rapidly. For $p_T(\text{jet1}) > 18 \text{ GeV}/c$, the $\langle N_{\text{chg}} \rangle$ calculations from ISAJET do not reproduce any data in the transverse region. The $\langle N_{\text{chg}} \rangle$ from PYTHIA undergoes a gradual transition at $p_T(\text{jet1}) \simeq 3 \text{ GeV}/c$ to a lower growth rate as the transverse momentum of the leading charged jet increases. Although the $\langle N_{\text{chg}} \rangle$ distribution has a shape similar to that observed in the data, the average number of charged particles generated by PYTHIA is greater than that obtained from the dijet sample for most values of $p_T(\text{jet1})$.

The average scalar p_T sum as a function of $p_T(\text{jet1})$ in the transverse region produced by HERWIG, ISAJET, and PYTHIA and determined from the dijet data is given in figure 6.6. As with $\langle N_{\text{chg}} \rangle$, the generated $\langle \sum p_T^{\text{chg}} \rangle$ rises rapidly in the region $p_T(\text{jet1}) \lesssim 3 \text{ GeV}/c$. Of the Monte Carlo generators, HERWIG's predictions moderate most severely for higher $p_T(\text{jet1})$. The distribution created by HERWIG is generally lower than most of the data. ISAJET forms an almost linear rise in $\langle \sum p_T^{\text{chg}} \rangle$ as the leading charged jet transverse momentum increases

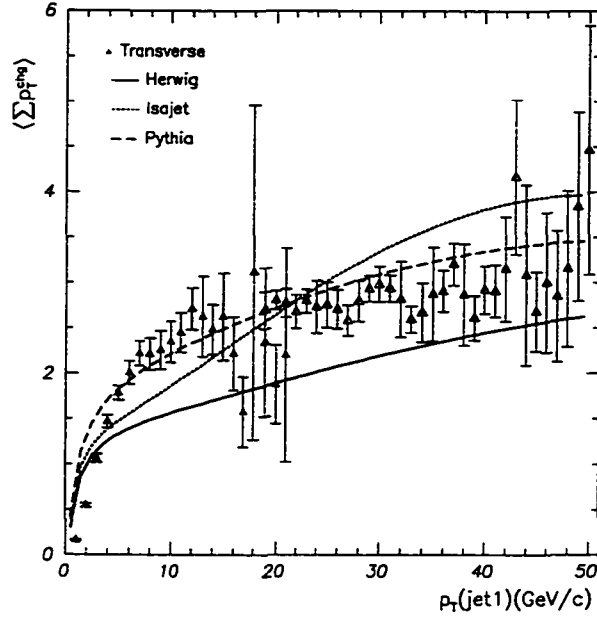


Figure 6.6: Comparison between dijet data and theoretical predictions in the transverse region for the average scalar p_T sum of charged particles as a function of $p_{T, \text{jet1}}$. The contribution from the leading charged jet is included. The solid and open triangles represent data in 1 GeV/c bins from the Min-Bias and Jet20 samples, respectively. The theoretical predictions are generated by the QCD hard scattering models of HERWIG, ISAJET, and PYTHIA and have been corrected for the CTC efficiency. The uncertainty for the uncorrected data points combines statistical and correlated systematic uncertainties.

from 3 to 30 GeV/c. After 30 GeV/c, the growth in $\langle \sum p_T^{\text{chg}} \rangle$ generated by ISAJET decreases eventually suggesting the formation of a plateau at $p_T(\text{jet1}) > 47$ GeV/c. The shape of ISAJET's $\langle \sum p_T^{\text{chg}} \rangle$ distribution does not match the data. PYTHIA produces values of $\langle \sum p_T^{\text{chg}} \rangle$ which replicate much of the behavior observed in the dijet sample for the transverse region. Although most features in the data are described, PYTHIA's predictions do demonstrate differences. For $5 < p_T(\text{jet1}) < 14$ GeV/c, the $\langle \sum p_T^{\text{chg}} \rangle$ from PYTHIA is slightly lower than the data. In addition, the generated $\langle \sum p_T^{\text{chg}} \rangle$ distribution rises more rapidly than the observations creating a small excess in the average scalar p_T sum for $p_T(\text{jet1}) \gtrsim 26$ GeV/c.

6.1.1.1 Sources of Charged Particle Multiplicity

The genesis of the theoretical predictions for average charged particle multiplicity in the transverse region is revealed in figures 6.7, 6.8, and 6.9 for HERWIG, ISAJET, and PYTHIA, respectively. The overall $\langle N_{\text{chg}} \rangle$ is decomposed into hard scattering and beam beam remnant components. Hard scattering contributions arise from outgoing jets and initial and final state radiation. The beam beam remnants originate in the dissolution of the proton and antiproton with multiple parton interactions included for PYTHIA.

The predicted distributions share similar characteristics, yet have features unique to the specific models employed. For $p_T(\text{jet1}) \lesssim 6$ GeV/c, the $\langle N_{\text{chg}} \rangle$ from the beam beam remnants form a peak where the remnants primarily compose the transverse $\langle N_{\text{chg}} \rangle$. The remnants from HERWIG and ISAJET generate approximate plateaus in $\langle N_{\text{chg}} \rangle$ for higher $p_T(\text{jet1})$. PYTHIA creates a $\langle N_{\text{chg}} \rangle$ distribution from the remnants which slowly decreases in a linear fashion with larger $p_T(\text{jet1})$. Ini-

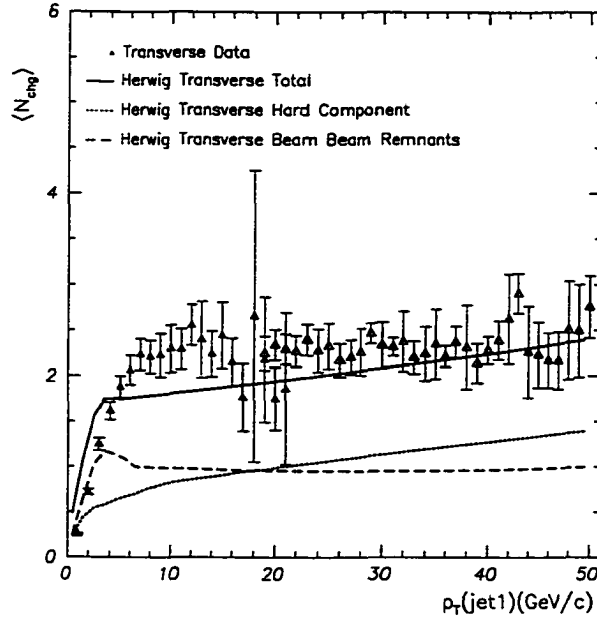


Figure 6.7: Dijet data and predictions from HERWIG for the average number of charged particles as a function of $p_T(\text{jet1})$ in the transverse region. Theoretical hard scattering and beam beam remnant contributions are isolated. The solid and open boxes represent data in 1 GeV/c bins from the Min-Bias and Jet20 samples, respectively. The theoretical predictions have been corrected for the CTC efficiency. The uncertainty for the uncorrected data points combines statistical and correlated systematic uncertainties.

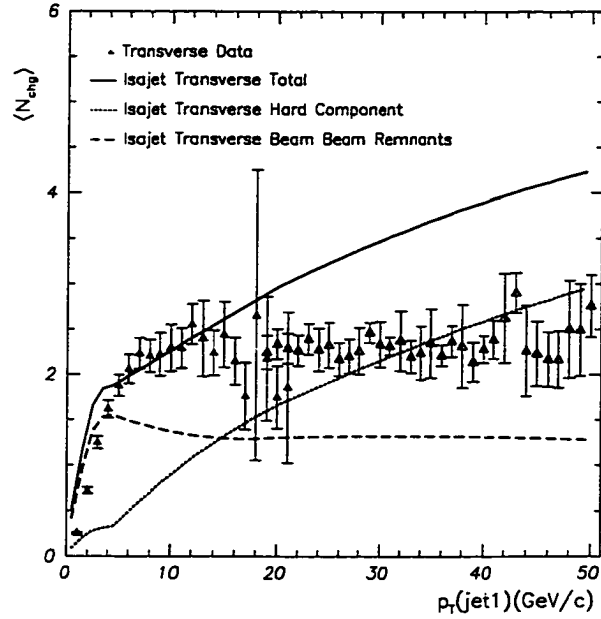


Figure 6.8: Dijet data and predictions from ISAJET for the average number of charged particles as a function of $p_T(\text{jet1})$ in the transverse region. Theoretical hard scattering and beam beam remnant contributions are isolated. The solid and open boxes represent data in 1 GeV/c bins from the Min-Bias and Jet20 samples, respectively. The theoretical predictions have been corrected for the CTC efficiency. The uncertainty for the uncorrected data points combines statistical and correlated systematic uncertainties.

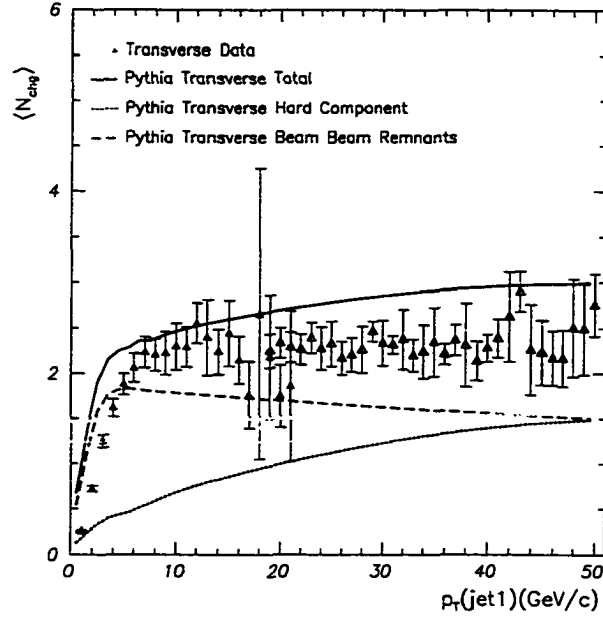


Figure 6.9: Dijet data and predictions from PYTHIA for the average number of charged particles as a function of $p_T(\text{jet1})$ in the transverse region. Theoretical hard scattering and beam beam remnant contributions are isolated. The solid and open boxes represent data in 1 GeV/c bins from the Min-Bias and Jet20 samples, respectively. The theoretical predictions have been corrected for the CTC efficiency. The uncertainty for the uncorrected data points combines statistical and correlated systematic uncertainties.

tially producing little $\langle N_{\text{chg}} \rangle$, the hard scattering component gains in prominence as $p_T(\text{jet1})$ increases. A transition from beam beam remnant to hard scattering component producing the dominant contribution of $\langle N_{\text{chg}} \rangle$ occurs for HERWIG at $p_T(\text{jet1}) \simeq 18 \text{ GeV}/c$ and for ISAJET at $p_T(\text{jet1}) \simeq 15 \text{ GeV}/c$. No transition occurs for PYTHIA in the range $p_T(\text{jet1}) \leq 50 \text{ GeV}/c$.

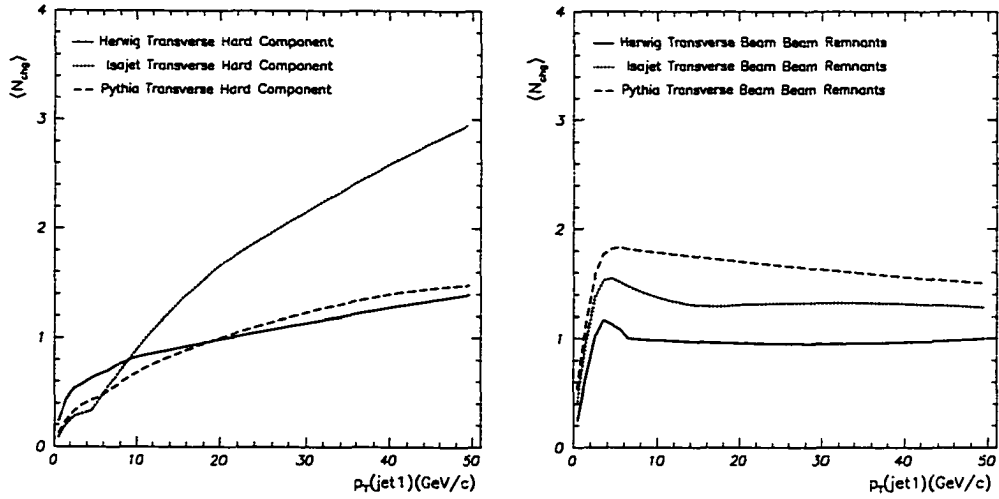


Figure 6.10: Comparison of the average charged particle multiplicity arising from the hard scattering component (left) and beam beam remnants (right) as a function of the transverse momentum of the leading charged jet as generated by HERWIG, ISAJET, and PYTHIA. The theoretical predications have been corrected for the CTC efficiency.

Predictions for charged particles originating from the same sources in the theoretical models are compared in figure 6.10. HERWIG and PYTHIA produce similar values for the hard scattering component. The rapid rise generated by ISAJET as $p_T(\text{jet1})$ increases is responsible for the disagreement with data in figure 6.5. The beam beam remnant distributions for the Monte Carlo simulations have similar shapes. The activity in $\langle N_{\text{chg}} \rangle$ for the beam beam remnants from PYTHIA is

greatest. When $p_T(\text{jet1}) \gtrsim 13 \text{ GeV}/c$, HERWIG and ISAJET predict plateaus in $\langle N_{\text{chg}} \rangle$.

The disparities between the predictions of the theoretical models is due to the mechanisms utilized to calculate the hard scattering processes. ISAJET generates parton showers with a hierarchy derived from the invariant mass in a strict leading log approximation. Both HERWIG and PYTHIA incorporate interference effects among the partons in a modified leading log approximation which produces an angular ordering that suppresses emission of high p_T radiation from the shower. Hadronization procedures differ as well, with the independent fragmentation employed by ISAJET creating an excess of soft hadrons. In addition, multiple parton interactions in PYTHIA enhance the $\langle N_{\text{chg}} \rangle$ contribution from the beam beam remnants. By adjusting the probability for interactions among consanguineous partons to occur, the height of the beam beam remnant plateau from PYTHIA can be regulated.

6.2 Event Structure in Z Data

The overall topology of the events in the Z boson sample differs substantially from the structure observed in the dijet data. The Z data is derived from an electron sample in which the invariant mass of the leading electrons is selected to coincide with a range about the Z boson mass². The electrons identified as the decay products of the Z boson are excluded from the event. The event structure

²A complete account of all requirements used to form the Z boson sample can be found in section 4.3

is analyzed with reference to the direction of the Z boson transverse momentum, $p_T(Z)$.

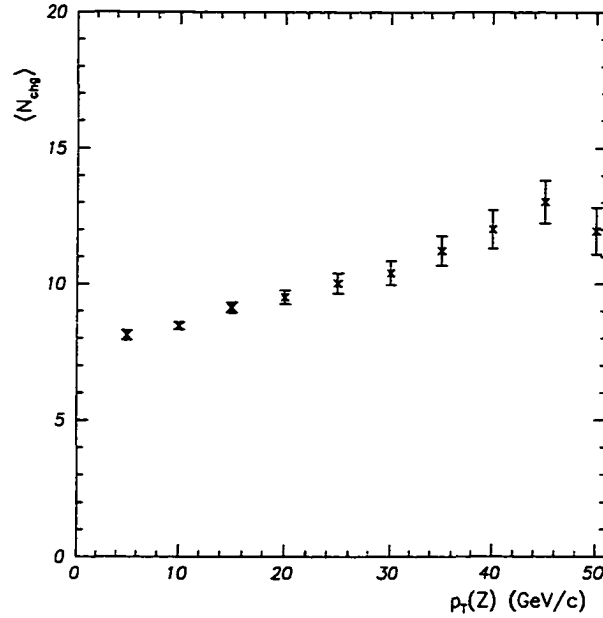


Figure 6.11: Z boson data for the average number of charged particles excluding Z boson decay products as a function of the transverse momentum of the Z boson. The bin size is 5 GeV/c. The errors on the (uncorrected) data include both statistical and correlated systematic uncertainties.

Figure 6.11 shows the average total multiplicity of charged particles as a function of the transverse momentum of the Z boson. The data demonstrate a constant rise in $\langle N_{\text{chg}} \rangle$ for increasing $p_T(Z)$. The dependence of $\langle N_{\text{chg}} \rangle$ on $p_T(Z)$ is approximately linear. Unlike for the dijet data, the activity of the Z boson event does not vanish as the transverse momentum of the reference object goes to zero. This behavior is a consequence of probing the event with a Z boson. In the Min-Bias studies, the transverse momentum of the leading jet was employed which allowed

a detailed examination of very low energy jets. This resulted in exploring regions which had little activity. In contrast, an event with low $p_T(Z)$ does not necessitate low activity. In fact since the Z has a mass of $91.187 \text{ GeV}/c^2$ and is created at a hadron collider, most Z boson events will be fairly dynamic.

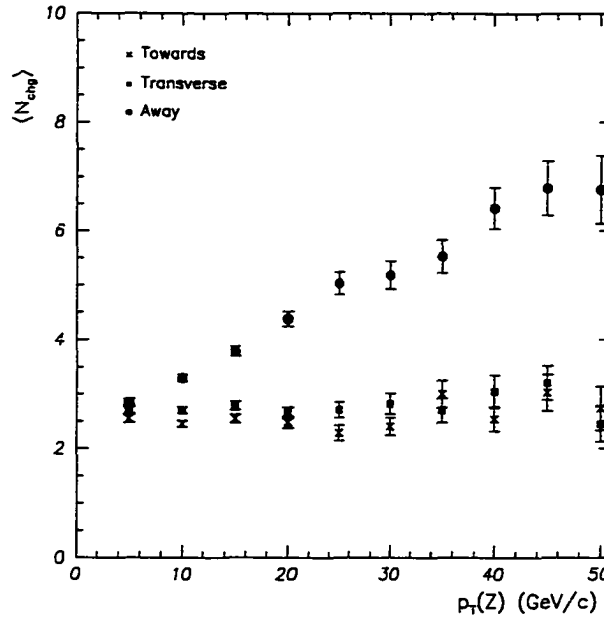


Figure 6.12: Z boson data for the average number of toward, away, and transverse charged particles excluding Z boson decay products as a function of the transverse momentum of the Z boson. The bin size is $5 \text{ GeV}/c$. The errors on the (uncorrected) data include both statistical and correlated systematic uncertainties.

The overall $\langle N_{\text{chg}} \rangle$ is partitioned into toward, away, and transverse regions in figure 6.12. The contribution from the away $\langle N_{\text{chg}} \rangle$ creates the rise observed in figure 6.11 for the overall average charged multiplicity. Since the away region includes a hard scattering jet balancing the production of a Z boson, the away $\langle N_{\text{chg}} \rangle$ is expected to increase for larger $p_T(Z)$. The slopes of the linear functions approx-

imating the overall and away $\langle N_{\text{chg}} \rangle$ are roughly equivalent. The distributions in the toward and transverse regions are consistent and have a constant $\langle N_{\text{chg}} \rangle$. By removing the Z boson decay products, the underlying event should represent the dominant component in the toward region. The underlying event is also isolated in the transverse region, where $\langle N_{\text{chg}} \rangle$ has a constant value of 2.7 charged particles.

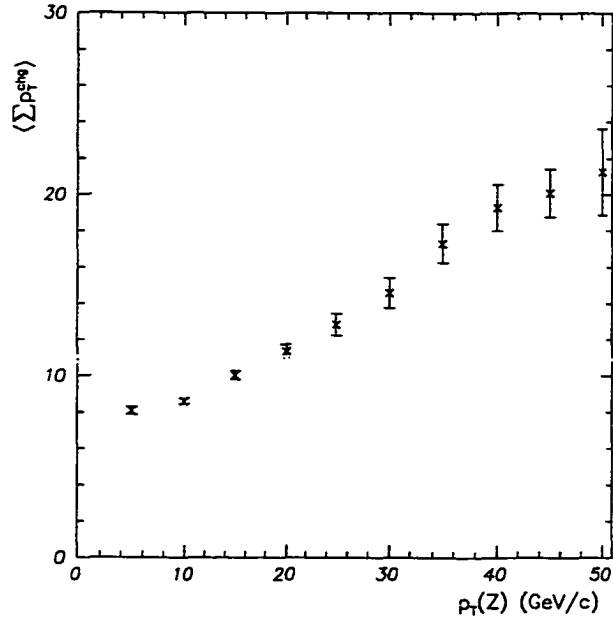


Figure 6.13: Z boson data for the average scalar p_T sum of charged particles excluding Z boson decay products as a function of the transverse momentum of the Z boson. The bin size is 5 GeV/c. The errors on the (uncorrected) data include both statistical and correlated systematic uncertainties.

The average scalar p_T sum of the charged particles as a function of $p_T(Z)$ is shown in figure 6.13. As the transverse momentum of the Z boson increases in the interval $0 \leq p_T(Z) < 15$ GeV/c, the overall $\langle \sum p_T^{\text{chg}} \rangle$ grows with a positive rate. The overall $\langle \sum p_T^{\text{chg}} \rangle$ moderates at larger p_T approaching a linear function

in the transverse momentum of the Z boson. For $p_T \geq 15$ GeV/c, the data are approximately described by

$$\langle \sum p_T^{\text{chg}} \rangle = 0.33 p_T(Z) + 5.0 .$$

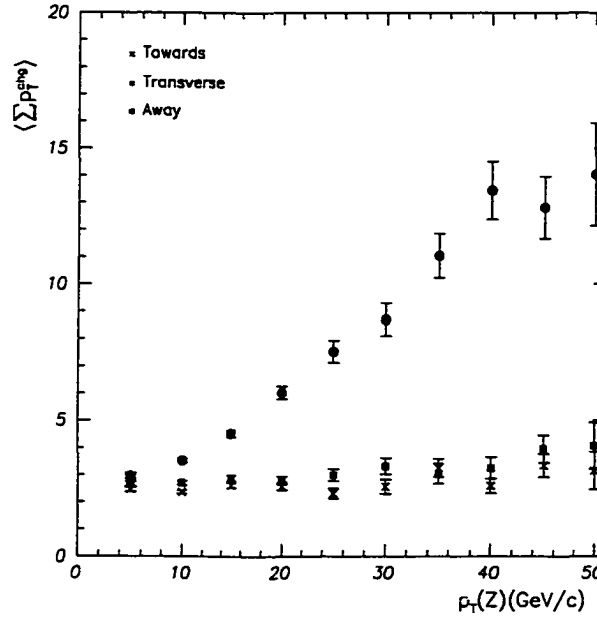


Figure 6.14: Z boson data for the average scalar p_T sum of toward, away, and transverse charged particles excluding Z boson decay products as a function of the transverse momentum of the Z boson. The bin size is 5 GeV/c. The errors on the (uncorrected) data include both statistical and correlated systematic uncertainties.

Figure 6.14 shows the $\langle \sum p_T^{\text{chg}} \rangle$ in the three angular regions for varying $p_T(Z)$. As for the average charged multiplicity, the contribution of $\langle \sum p_T^{\text{chg}} \rangle$ from the away region with $p_T(Z) > 10$ GeV/c produces the overall rise of the average scalar p_T sum of charged particles in figure 6.13. The toward and transverse $\langle \sum p_T^{\text{chg}} \rangle$ once again are consistent with one another. They form a flat plateau and are

suggestive of the underlying event. The transverse distribution has a constant value of $\langle \sum p_T^{\text{chg}} \rangle \simeq 3 \text{ GeV}/c$.

The behavior of the Z boson and dijet event structures generally agree in the away and transverse regions. The contribution from the toward region produces the disparity between the overall $\langle N_{\text{chg}} \rangle$ and $\langle \sum p_T^{\text{chg}} \rangle$ observed in the Z boson and dijet samples. While the leading charged jet was included for the dijet analysis, the decay products of the Z boson were explicitly removed from the event. Slight differences between the $\langle N_{\text{chg}} \rangle$ and $\langle \sum p_T^{\text{chg}} \rangle$ in the angular regions of the various samples indicate possible effects due to the mechanisms of production and particles created. A hard scattering between two partons has necessarily occurred in a Z boson event, while no such requirement exists for the dijet events. The resultant Z boson is a color singlet which has no associated gluon radiation. The particles producing leading charged jets in the dijet sample are likely to carry color and can therefore radiate gluons increasing the final particle multiplicity of an event.

6.2.1 The Z Transverse Region: Theory and Data

Theoretical expectations of the average charged multiplicity and scalar p_T sum for events containing Z bosons are determined and contrasted with the data in figures 6.11, 6.12, 6.13, and 6.14. The production of Z bosons occurs in most Monte Carlo models via two mechanisms. Single Z bosons can be created through the Drell-Yan Born process $q\bar{q} \rightarrow Z$ with jets provided by initial state radiation. Jets associated with the Z boson are produced in the order α_s 2-to-2 processes $q\bar{q} \rightarrow Zg$ and $gq \rightarrow Zq$ with initial and final state radiation incorporated. Earlier versions of

HERWIG included only the Drell-Yan Z calculations³. Since this analysis examines 2-to-2 hard scattering interactions, ISAJET 7.32 and PYTHIA 6.115 are utilized to generate predictions for Z boson production from proton antiproton collisions at 1.8 TeV. The default values for the parameters employed by the Monte Carlo generators are used with $p_T^{\text{hard}} > 3 \text{ GeV}/c$ to avoid the divergence in the subprocess as the momentum approaches zero. As for the dijet theoretical results, the charged tracks from ISAJET and PYTHIA are modified by the 92% track finding efficiency of the CTC.

The average charged multiplicity generated by ISAJET and PYTHIA and obtained from the Z boson sample as a function of $p_T(Z)$ is shown in figures 6.15 and 6.16 for the overall event and the transverse region, respectively. The overall $\langle N_{\text{chg}} \rangle$ predicted by both models is too low in comparison to the data for $p_T(Z) < 20 \text{ GeV}/c$. The distribution describing the average charged multiplicity of the events in ISAJET rises rapidly producing too many charged particles at large $p_T(Z)$. The generated $\langle N_{\text{chg}} \rangle$ from PYTHIA creates a shape which corresponds to experimental results, but is consistently lower by approximately 3.1 charged particles. Instead of predicting a plateau in the transverse region for $\langle N_{\text{chg}} \rangle$, both Monte Carlo models produce values which increase as $p_T(Z)$ grows. The average charged multiplicity calculated by ISAJET rises from $\langle N_{\text{chg}} \rangle \simeq 1.5$ charged particles at $p_T(Z) = 0.5 \text{ GeV}/c$ to $\langle N_{\text{chg}} \rangle \simeq 3.7$ charged particles at $p_T(Z) = 50 \text{ GeV}/c$. The shape of ISAJET's $\langle N_{\text{chg}} \rangle$ distribution is incommensurate with data. PYTHIA generates values for $\langle N_{\text{chg}} \rangle$ in the transverse region which are slightly smaller than the data at $p_T(Z) < 20 \text{ GeV}/c$. For $p_T \geq 20 \text{ GeV}/c$, PYTHIA's predictions reproduce the

³The Compton scattering and annihilation calculations are contained in HERWIG version 6.

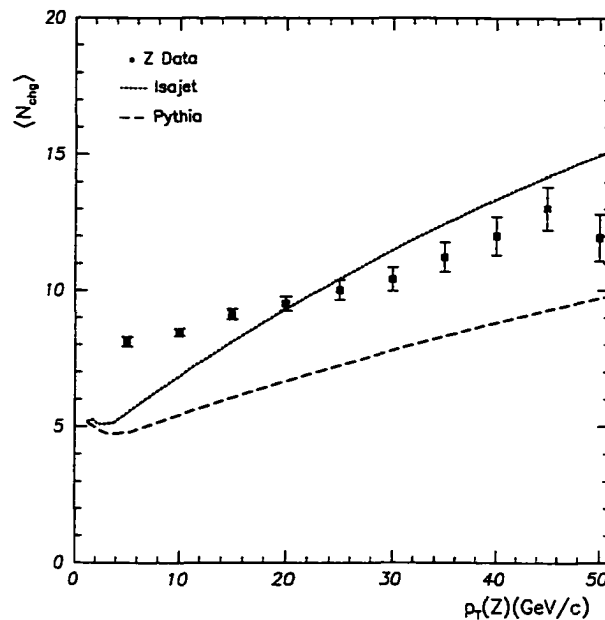


Figure 6.15: Comparison between Z boson data and theoretical predictions for the average number of charged particles excluding Z boson decay products as a function of $p_T(Z)$. The solid triangles represent Z boson data in 5 GeV/c bins. The theoretical predictions are generated by the QCD hard scattering models of ISAJET and PYTHIA and have been corrected for the CTC efficiency. The uncertainty for the uncorrected data points combines statistical and correlated systematic uncertainties.

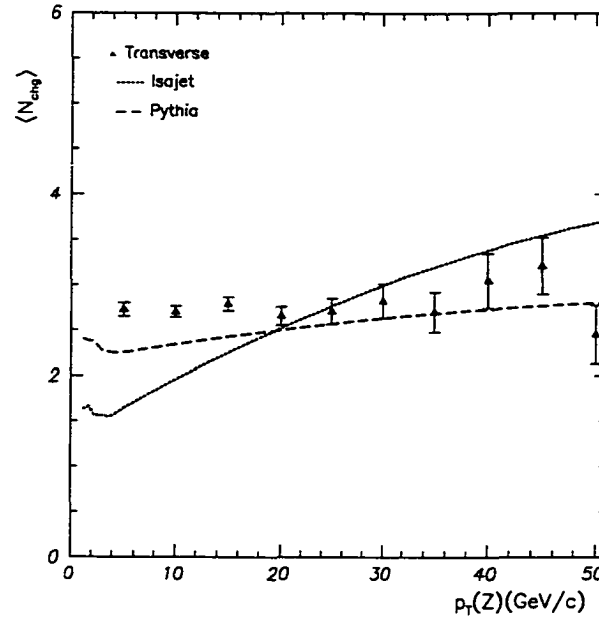


Figure 6.16: Comparison between Z boson data and theoretical predictions in the transverse region for the average number of charged particles excluding Z boson decay products as a function of $p_T(Z)$. The solid triangles represent Z boson data in 5 GeV/c bins. The theoretical predictions are generated by the QCD hard scattering models of ISAJET and PYTHIA and have been corrected for the CTC efficiency. The uncertainty for the uncorrected data points combines statistical and correlated systematic uncertainties.

observations and the growth in $\langle N_{\text{chg}} \rangle$ moderates as p_T increases. The distribution created by PYTHIA for $\langle N_{\text{chg}} \rangle$ approximates the data well at higher transverse momenta of the Z boson.

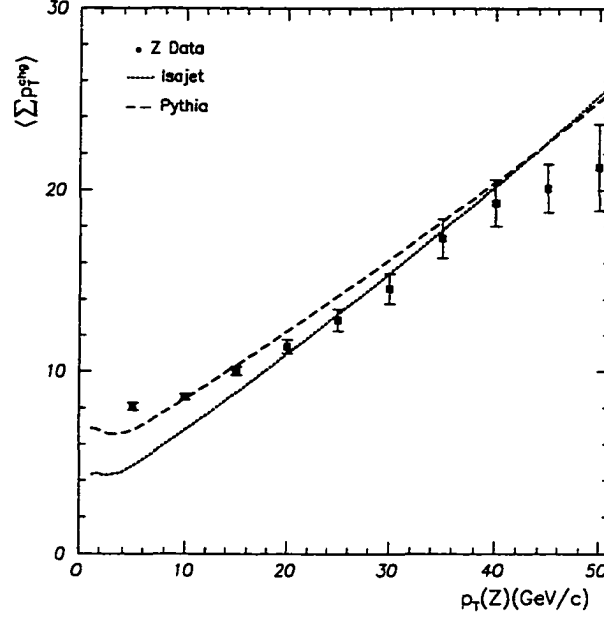


Figure 6.17: Comparison between Z boson data and theoretical predictions for the average scalar p_T sum of charged particles excluding Z boson decay products as a function of $p_T(Z)$. The solid triangles represent Z boson data in 5 GeV/c bins. The theoretical predictions are generated by the QCD hard scattering models of ISAJET and PYTHIA and have been corrected for the CTC efficiency. The uncertainty for the uncorrected data points combines statistical and correlated systematic uncertainties.

Figures 6.17 and 6.18 show the dependence of the overall and transverse average scalar p_T sum of charged particles on the transverse momentum of the Z boson. ISAJET and PYTHIA produce less overall $\langle \sum p_T^{\text{chg}} \rangle$ than observed at low $p_T(Z)$. ISAJET's predictions coincide with data in the region $20 \leq p_T(Z) \leq 40$ GeV/c. Thereafter, the rapid growth in overall $\langle \sum p_T^{\text{chg}} \rangle$ from ISAJET as $p_T(Z)$ increases

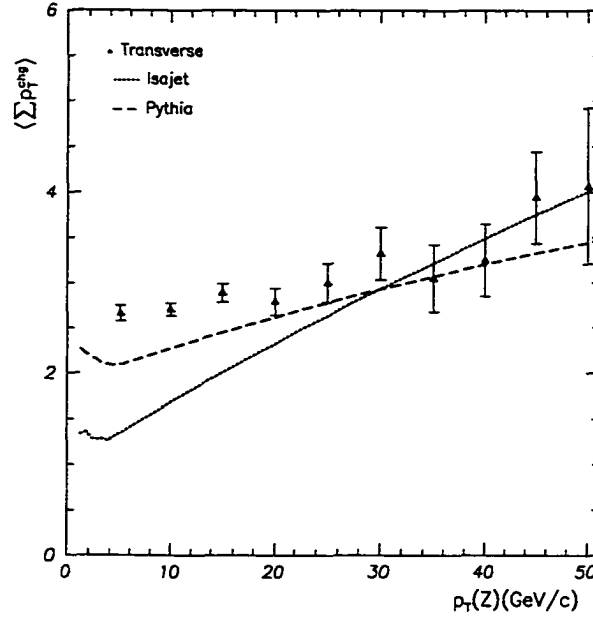


Figure 6.18: Comparison between Z boson data and theoretical predictions in the transverse region for the average scalar p_T sum of charged particles excluding Z boson decay products as a function of $p_T(Z)$. The solid triangles represent Z boson data in 5 GeV/c bins. The theoretical predictions are generated by the QCD hard scattering models of ISAJET and PYTHIA and have been corrected for the CTC efficiency. The uncertainty for the uncorrected data points combines statistical and correlated systematic uncertainties.

creates values which are greater than data. The overall $\langle \sum p_T^{\text{chg}} \rangle$ generated by PYTHIA also has a rate of increase as $p_T(Z)$ grows which is not present in the observations. This effect is tempered in comparison to that of ISAJET's, but still produces a distribution which does not describe features of the data. In the transverse region, the Monte Carlo generators predict values for $\langle \sum p_T^{\text{chg}} \rangle$ which are generally less than those from the Z boson sample. The $\langle \sum p_T^{\text{chg}} \rangle$ from ISAJET rises rapidly as $p_T(Z)$ increases creating a behavior which agrees with the observations only for $p_T(Z) \geq 35$ GeV/c. ISAJET's distribution of $\langle \sum p_T^{\text{chg}} \rangle$ in the transverse region does not match the trend found in the data. The transverse $\langle \sum p_T^{\text{chg}} \rangle$ from PYTHIA underestimates the observations for $p_T < 20$ GeV/c. With a steeper increase than expected from data, PYTHIA reproduces much of the average scalar p_T sum in the transverse region obtained from the Z boson sample.

6.3 Event Structure in J/ψ B Data

The J/ψ B data sample affords the ability to utilize both a leading charged jet and a particle resulting from a hard scattering interaction in the analysis of event structures. The sample is obtained from dimuon data which is subjected to the requirements described in section 4.4. The transverse momenta of the J/ψ , $p_T(J/\psi)$, range from 2 to 51 GeV/c. The extremely low number of J/ψ particles with $p_T(J/\psi) > 35$ GeV/c produces a region in which the uncertainties are statistics dominated and highly unreliable. Therefore, the $p_T(\text{jet1})$ and $p_T(J/\psi)$ are limited to upper bounds of 35 GeV/c. Dijet and Z boson data are compared to observations obtained using the leading charged jet and J/ψ in the J/ψ B sample, respectively.

6.3.1 Event Structure using the Leading Jet

The leading charged jet is employed to determine the behavior of the event structure in the J/ψ B data sample. Construction of the charged particle jets occurs according to the prescription in section 5.1. As in the analysis of the dijet sample, the particles from the leading charged jet are included in calculations of both $\langle N_{\text{chg}} \rangle$ and $\langle \sum p_T^{\text{chg}} \rangle$.

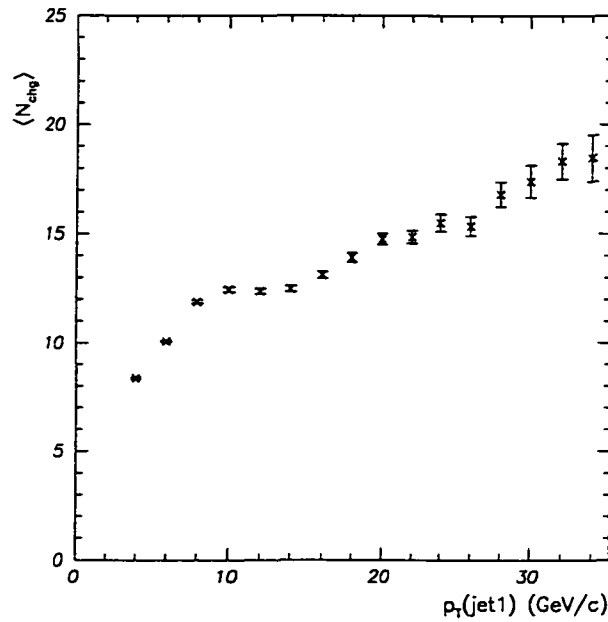


Figure 6.19: J/ψ B data for the average number of charged particles as a function of $p_T(\text{jet1})$. The contribution from the leading charged jet is included. The bin size in $p_T(\text{jet1})$ is 2 GeV/c. The uncertainty for the uncorrected data points combines statistical and correlated systematic uncertainties.

Figures 6.19 and 6.20 show the average number of charged particles as a function of the transverse momentum of the leading charged jet. The overall $\langle N_{\text{chg}} \rangle$ given in figure 6.19 demonstrates generally increasing values for greater $p_T(\text{jet1})$.

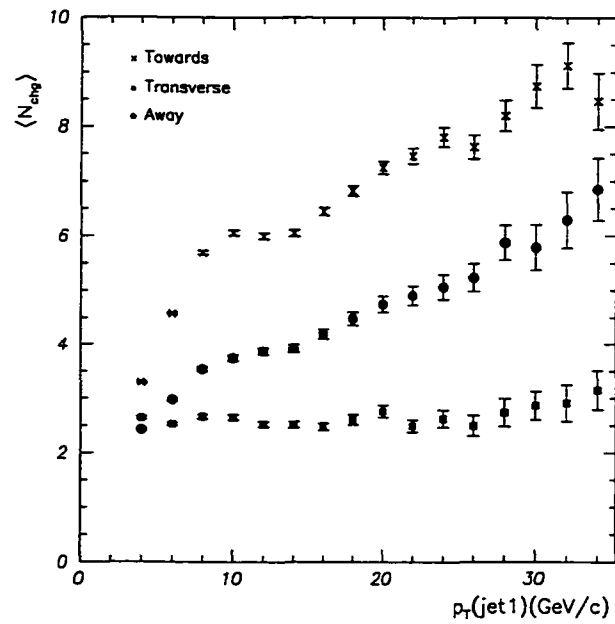


Figure 6.20: J/ψ B data for the average number of toward, away, and transverse charged particles as a function of $p_T(\text{jet1})$. The contribution from the leading charged jet is included. The bin size in $p_T(\text{jet1})$ is 2 GeV/c. The uncertainty for the uncorrected data points combines statistical and correlated systematic uncertainties.

Two approximately flat plateaus interrupt the rising trend in the $p_T(\text{jet1})$ regions 10 to 14 GeV/c and 20 to 26 GeV/c. Segregating the average charged multiplicity into towards, away, and transverse regions in figure 6.20, the cause for the behavior observed in the overall $\langle N_{\text{chg}} \rangle$ can be discerned. Plateaus occur for toward and away $\langle N_{\text{chg}} \rangle$ in the $p_T(\text{jet1})$ range of 10 to 14 GeV/c. If the toward and away average charge multiplicities are combined, a plateau is found for $20 \leq p_T(\text{jet1}) \leq 26$ GeV/c. The transverse region isolates the underlying event and appears as a flat distribution with $\langle N_{\text{chg}} \rangle \simeq 2.6$ charged particles.

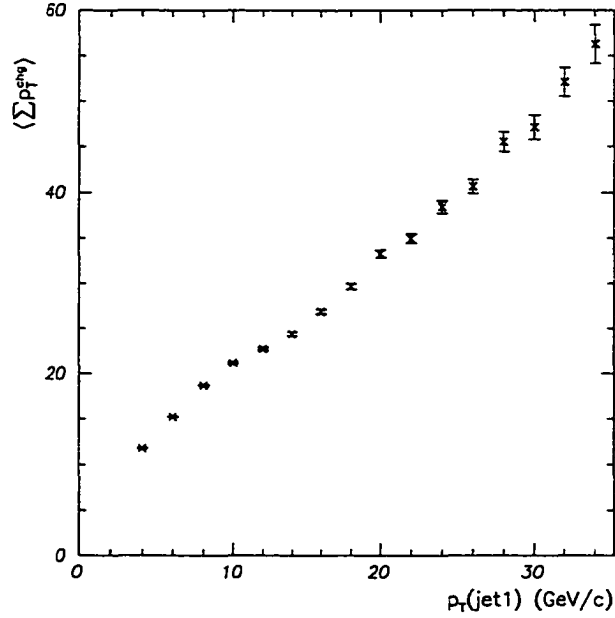


Figure 6.21: J/ψ B data for the average scalar p_T sum of charged particles as a function of $p_T(\text{jet1})$. The contribution from the leading charged jet is included. The bin size in $p_T(\text{jet1})$ is 2 GeV/c. The uncertainty for the uncorrected data points combines statistical and correlated systematic uncertainties.

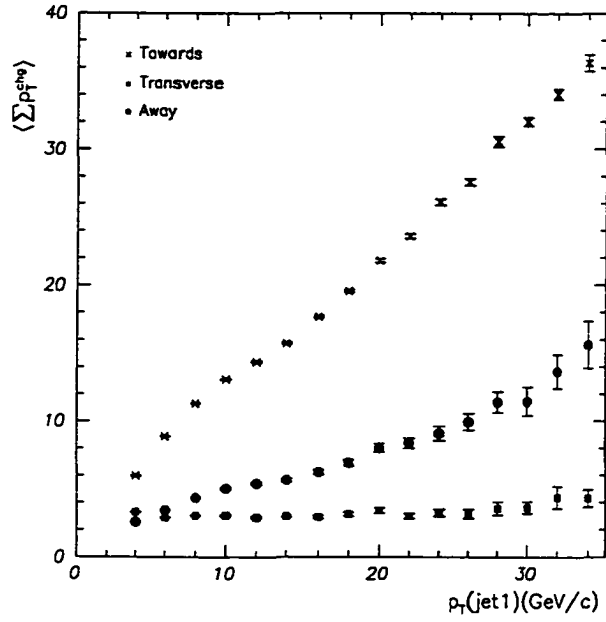


Figure 6.22: J/ψ B data for the average scalar p_T sum of toward, away, and transverse charged particles as a function of $p_T(\text{jet1})$. The contribution from the leading charged jet is included. The bin size in $p_T(\text{jet1})$ is 2 GeV/c. The uncertainty for the uncorrected data points combines statistical and correlated systematic uncertainties.

The average scalar p_T sum as a function of the transverse momentum of the leading charged jet is shown in figures 6.21 and 6.22. The distribution for the overall $\langle \sum p_T^{\text{chg}} \rangle$ exhibits an approximately constant increase as $p_T(\text{jet1})$ grows except in the region $p_T(\text{jet1}) = 10$ to 14 GeV/c where the increase occurs at a lower rate. Once again, the toward and away $\langle \sum p_T^{\text{chg}} \rangle$ are responsible for this feature. The dominant contribution to the overall $\langle \sum p_T^{\text{chg}} \rangle$ arises from the component in the toward region, with the away $\langle \sum p_T^{\text{chg}} \rangle$ representing a smaller, but increasing, constituent. The $\langle \sum p_T^{\text{chg}} \rangle$ in the transverse region forms a plateau with an approximately constant value of 3.0 GeV/c for $p_T(\text{jet1}) \leq 35$ GeV/c.

6.3.1.1 Comparison of J/ψ and Dijet Data

The dijet data for average charged multiplicity and scalar p_T sum in figures 6.1, 6.2, and 6.3 are compared to results from the J/ψ B sample given in figures 6.19, 6.20, and 6.22. Both samples are examined with respect to the leading charged jet defined by the same algorithm given in section 5.1. The multiplicity and momentum in the toward region for dijet and J/ψ B data include the contribution from the leading charged jet. By analyzing differences with and similarities to the dijet $\langle N_{\text{chg}} \rangle$ and $\langle \sum p_T^{\text{chg}} \rangle$, novel features of the underlying event from collisions which produce B mesons may be ascertained.

Figures 6.23 and 6.24 compare the average charged multiplicity as a function of $p_T(\text{jet1})$ obtained from the dijet and J/ψ B data samples. The dijet and J/ψ B values for overall $\langle N_{\text{chg}} \rangle$ are consistent with one another. When $p_T(\text{jet1}) < 2$ GeV/c, no data exists for the J/ψ B sample due to the inefficiencies arising from muon detection and reconstruction. If the data could be extended to $p_T(\text{jet1}) \rightarrow 0$

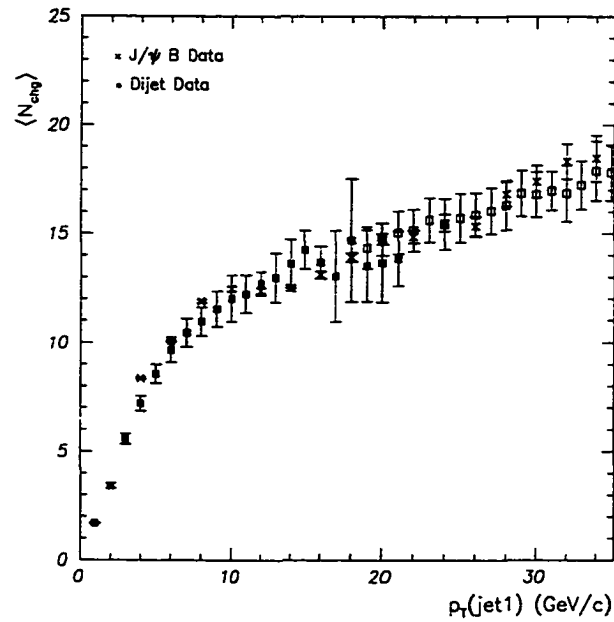


Figure 6.23: Comparison of average number of charged particles in the dijet (solid and open boxes) and $J/\psi B$ (crosses) samples as a function of $p_T(\text{jet1})$. The bin size for the dijet and $J/\psi B$ data is 1 and 2 GeV/c, respectively. The uncertainty for the uncorrected data points combines statistical and correlated systematic uncertainties.

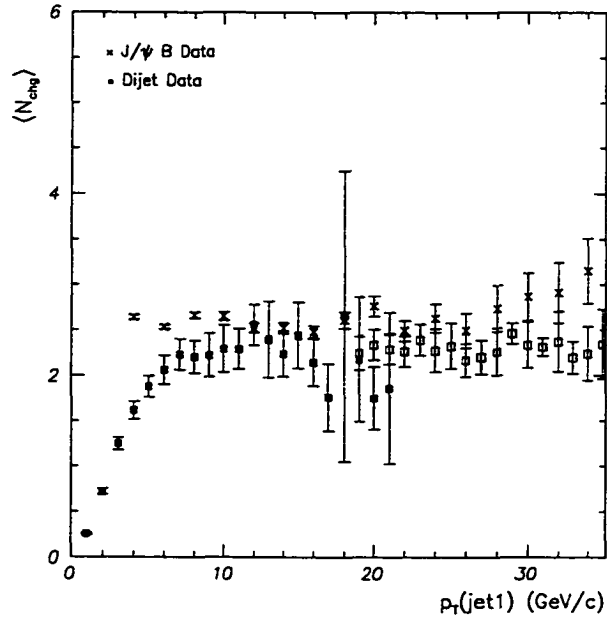


Figure 6.24: Comparison of average number of charged particles in the dijet (solid and open boxes) and J/ψ B (crosses) samples for the transverse region as a function of $p_T(\text{jet1})$. The bin size for the dijet and J/ψ B data is 1 and 2 GeV/c. respectively. The uncertainty for the uncorrected data points combines statistical and correlated systematic uncertainties.

GeV/c, differences between the dijet and $J/\psi B$ $\langle N_{\text{chg}} \rangle$ probably would appear. Candidate B mesons are created in the $J/\psi B$ sample even at low $p_T(\text{jet1})$, whereas no hard interaction is required in the dijet data. The B meson with mass greater than $5 \text{ GeV}/c^2$ decays to a J/ψ with mass $3.09688 \text{ GeV}/c^2$ and another particle. The J/ψ in turn decays to two muons, each with mass $105.658 \text{ MeV}/c^2$. Since the muons are included in the leading charged jet, kinematic considerations imply that no low p_T leading charged jets will exist in the $J/\psi B$ data. The transverse $\langle N_{\text{chg}} \rangle$ of the two samples shown in figure 6.24 demonstrates differences at low $p_T(\text{jet1})$. Dijet and $J/\psi B$ transverse $\langle N_{\text{chg}} \rangle$ do not agree in the region $p_T(\text{jet1}) < 12 \text{ GeV}/c$. In contrast to the decrease observed for the dijet $\langle N_{\text{chg}} \rangle$, the $J/\psi B$ $\langle N_{\text{chg}} \rangle$ is roughly constant. This behavior is indicative of a contribution to the average charged multiplicity from the underlying event for all $J/\psi B$ events. Dijet and $J/\psi B$ $\langle N_{\text{chg}} \rangle$ are similar for $12 \leq p_T(\text{jet1}) \leq 32 \text{ GeV}/c$, although the $J/\psi B$ data indicate a rise when $p_T(\text{jet1}) > 26 \text{ GeV}/c$ not apparent in the dijet sample.

The $\langle \sum p_T^{\text{chg}} \rangle$ in the transverse region from dijet and $J/\psi B$ data for varying $p_T(\text{jet1})$ is shown in figure 6.25. The correlation between the transverse $\langle \sum p_T^{\text{chg}} \rangle$ of the samples is worse than that observed for the transverse $\langle N_{\text{chg}} \rangle$. This suggests that collisions in which B mesons are produced have an underlying event similar in average multiplicity but with higher average total scalar p_T of charged particles than found for the dijet data. When $p_T(\text{jet1}) < 12 \text{ GeV}/c$, the $J/\psi B$ $\langle \sum p_T^{\text{chg}} \rangle$ increases slightly as $p_T(\text{jet1})$ decreases in opposition to the behavior of the dijet $\langle \sum p_T^{\text{chg}} \rangle$ distribution. A more pronounced increase in the transverse $\langle \sum p_T^{\text{chg}} \rangle$ from the $J/\psi B$ sample occurs for $p_T(\text{jet1}) > 26 \text{ GeV}/c$ as the dijet $\langle \sum p_T^{\text{chg}} \rangle$ remains

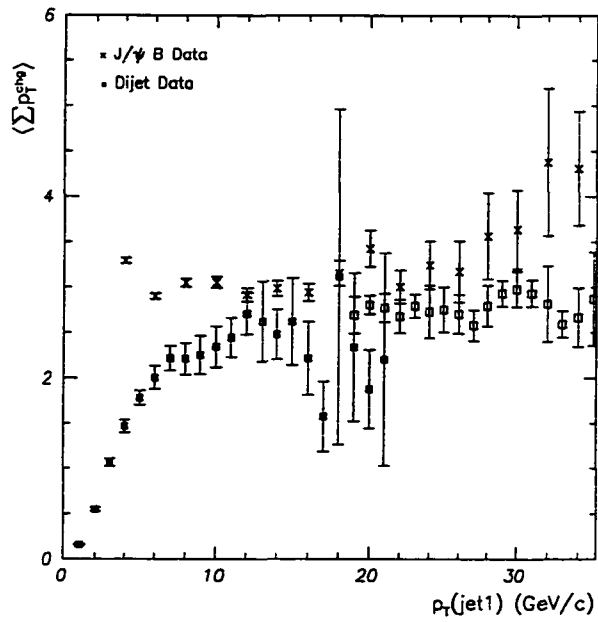


Figure 6.25: Comparison of average scalar p_T sum in the dijet (solid and open boxes) and J/ψ B (crosses) samples for the transverse region as a function of $p_{T(\text{jet1})}$. The bin size for the dijet and J/ψ B data is 1 and 2 GeV/c, respectively. The uncertainty for the uncorrected data points combines statistical and correlated systematic uncertainties.

constant. The agreement between dijet and J/ψ B samples is tenuous in the range $12 \leq p_T(\text{jet1}) \leq 26$ GeV/c.

6.3.2 Event Structure using the J/ψ

The structure of events in the J/ψ B sample is analyzed using the direction and magnitude of the J/ψ transverse momentum. The uncertainty associated with the data increases appreciably for $p_T(J/\psi) \geq 28$ GeV/c due to the dramatic decrease in the number of reconstructed J/ψ particles. When $p_T(J/\psi) > 35$ GeV/c. the low J/ψ multiplicity produces inaccurate results for average quantities in the sample. The decay products of the J/ψ are treated in the same fashion as were those of the Z boson. Muons identified as the J/ψ offspring are excluded from the events.

The average charged multiplicity as a function of the transverse momentum of the J/ψ is shown in figures 6.26 and 6.27. A linear rise of the overall $\langle N_{\text{chg}} \rangle$ with respect to $p_T(J/\psi)$ occurs in the region $6 \leq p_T(J/\psi) < 28$ GeV/c. While the sample contains no J/ψ with $p_T \leq 2$ GeV/c, the data for $2 < p_T < 6$ GeV/c suggest that the overall $\langle N_{\text{chg}} \rangle$ approaches a constant value as the transverse momentum of the J/ψ decreases. This effect is the result of requiring J/ψ particles in the sample. The B mesons which produce the J/ψ candidates used to create the J/ψ B sample are generally the product of hard scattering collisions [89]. Since even low transverse momentum B mesons are formed in energetic interactions, the event will contain a positive charged particle multiplicity. The contributions to the overall $\langle N_{\text{chg}} \rangle$ from the toward and away regions cause the observed rise for higher $p_T(J/\psi)$. Toward and away $\langle N_{\text{chg}} \rangle$ values are consistent for $p_T(J/\psi) < 28$ GeV/c. The increasing $\langle N_{\text{chg}} \rangle$ in the away region is produced by higher transverse momenta

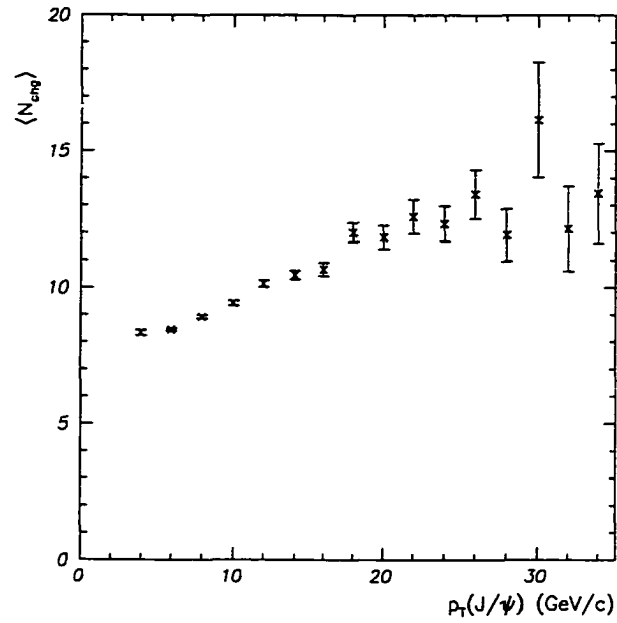


Figure 6.26: J/ψ B data for the average number of charged particles as a function of $p_T(J/\psi)$. The muons from the J/ψ decay have been removed. The bin size in $p_T(J/\psi)$ is 2 GeV/c. The uncertainty for the uncorrected data points combines statistical and correlated systematic uncertainties.

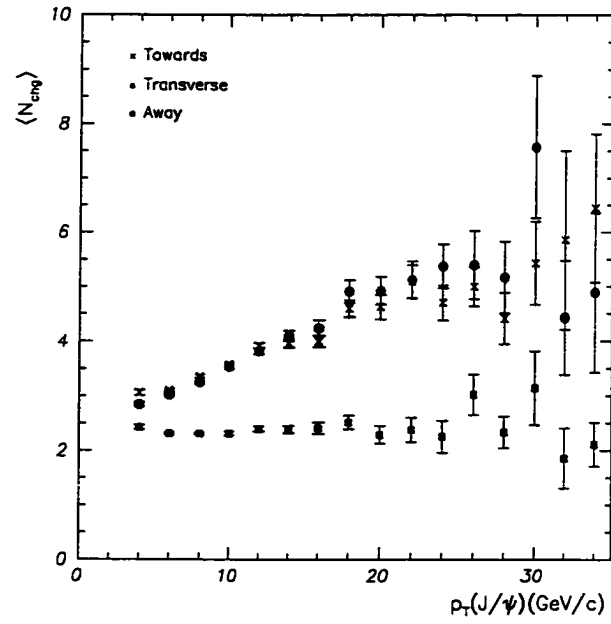


Figure 6.27: J/ψ B data for the average number of toward, away, and transverse charged particles as a function of $p_T(J/\psi)$. The muons from the J/ψ decay have been removed. The bin size in $p_T(J/\psi)$ is 2 GeV/c. The uncertainty for the uncorrected data points combines statistical and correlated systematic uncertainties.

jets balancing the 2-to-2 hard interaction. Although the contribution from the J/ψ is removed in the toward region, the parent B decays as $B \rightarrow J/\psi X$, where X is another particle state. The X component will on average be included in the calculation of the toward $\langle N_{\text{chg}} \rangle$ [84]. The flat distribution of the average charged multiplicity in the transverse region is representative of the underlying event. The transverse $\langle N_{\text{chg}} \rangle$ has an approximate value of 2.3 charged particles.

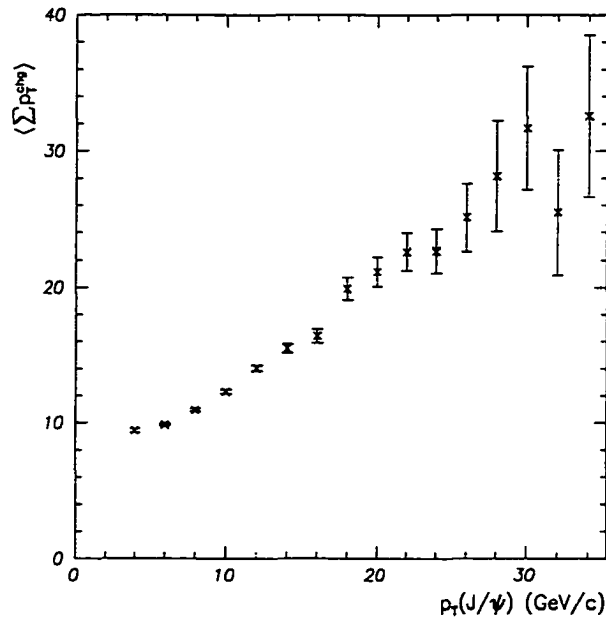


Figure 6.28: J/ψ B data for the average scalar p_T sum of charged particles as a function of $p_T(J/\psi)$. The contribution from the leading charged jet is included. The bin size in $p_T(J/\psi)$ is 2 GeV/c. The uncertainty for the uncorrected data points combines statistical and correlated systematic uncertainties.

Figures 6.28 and 6.29 show the dependence of the average scalar p_T sum on the J/ψ transverse momentum. While the overall $\langle \sum p_T^{\text{chg}} \rangle$ values grow as $p_T(J/\psi)$ increases, the distribution is interrupted by several features. For $p_T(J/\psi) < 6$

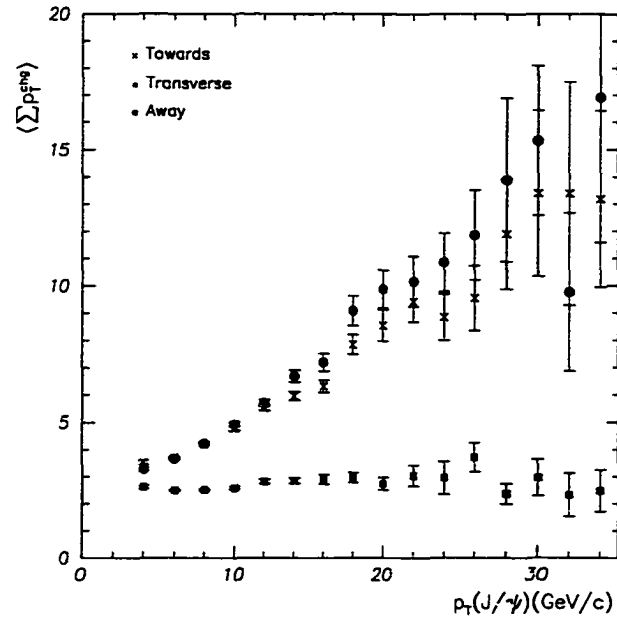


Figure 6.29: J/ψ B data for the average scalar p_T sum of toward, away, and transverse charged particles as a function of $p_T(J/\psi)$. The muons from the J/ψ decay have been removed. The bin size in $p_T(J/\psi)$ is 2 GeV/c. The uncertainty for the uncorrected data points combines statistical and correlated systematic uncertainties.

GeV/c, $\langle \sum p_T^{\text{chg}} \rangle$ apparently coincides with a constant value at low J/ψ transverse momentum. The regions $6 \leq p_T(J/\psi) \leq 16$ GeV/c and $18 \leq p_T(J/\psi) < 28$ GeV/c contain $\langle \sum p_T^{\text{chg}} \rangle$ values which can be approximated by linear functions of $p_T(J/\psi)$ with the same slope. A transition in $\langle \sum p_T^{\text{chg}} \rangle$ occurs when the J/ψ transverse momentum increases from 16 to 18 GeV/c. This behavior originates in the toward and away regions, where the distribution of $\langle \sum p_T^{\text{chg}} \rangle$ exhibits similar characteristics. The toward and away $\langle \sum p_T^{\text{chg}} \rangle$ are also responsible for the rise in overall $\langle \sum p_T^{\text{chg}} \rangle$ values. Although consistent at lower momenta, the away $\langle \sum p_T^{\text{chg}} \rangle$ is greater than the toward $\langle \sum p_T^{\text{chg}} \rangle$ for $p_T(J/\psi) > 12$ GeV/c. Unlike the toward and away regions, the transverse $\langle \sum p_T^{\text{chg}} \rangle$ is constant with a value of $\langle \sum p_T^{\text{chg}} \rangle \simeq 2.8$ GeV/c.

6.3.2.1 Comparison of J/ψ and Z Data

The behavior of average charged multiplicity and scalar p_T sum from the J/ψ B sample as a function of $p_T(J/\psi)$ in relation to the results obtained from the Z sample as a function of $p_T(Z)$ is examined. The decay products of reconstructed particles are treated in both data samples similarly. The muons and electrons from the J/ψ and Z decays, respectively, are removed from the event. The transverse momentum representing the same magnitude for the Z boson and J/ψ particle, $p_T(Z \text{ or } J/\psi)$, is employed to compare $\langle N_{\text{chg}} \rangle$ and $\langle \sum p_T^{\text{chg}} \rangle$ from the different samples. Disagreement between the Z and J/ψ B data may indicate that the color of the produced particles influences the observed event structure and the underlying event.

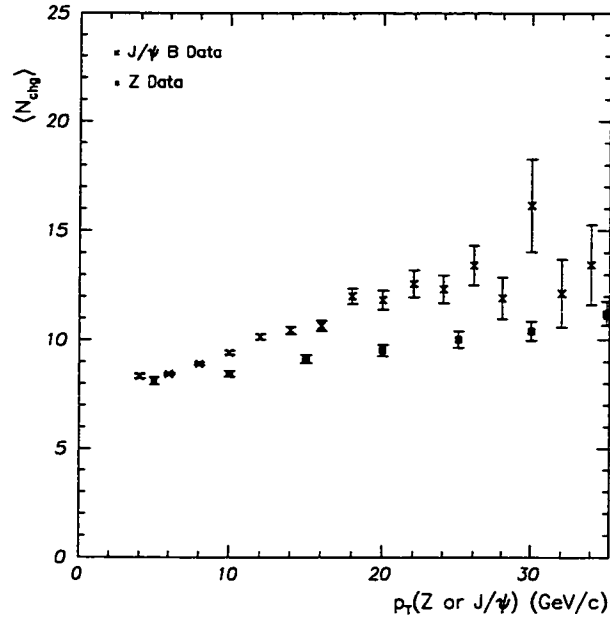


Figure 6.30: Comparison of average number of charged particles in the Z boson (solid boxes) sample as a function of $p_T(Z)$ and $J/\psi B$ (crosses) sample as a function of $p_T(J/\psi)$. The bin size for the Z and $J/\psi B$ data is 5 and 2 GeV/c. respectively. The uncertainty for the uncorrected data points combines statistical and correlated systematic uncertainties.

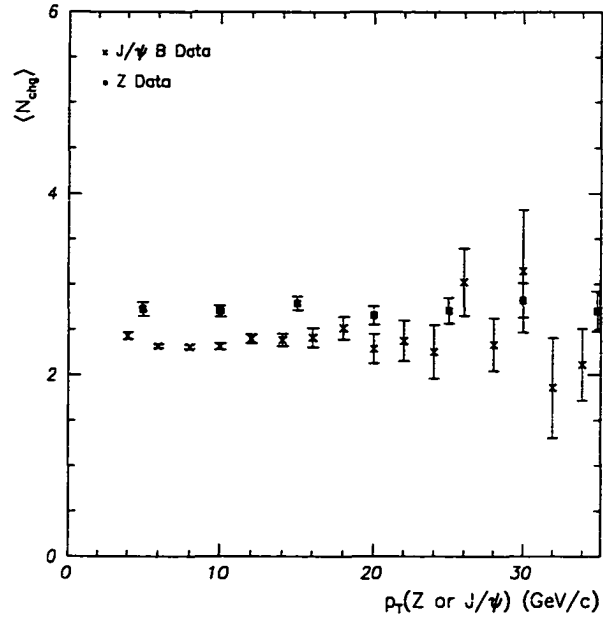


Figure 6.31: Comparison of average number of charged particles for the transverse region in the Z boson (solid boxes) sample as a function of $p_T(Z)$ and $J/\psi B$ (crosses) sample as a function of $p_T(J/\psi)$. The bin size for the Z and $J/\psi B$ data is 5 and 2 GeV/c, respectively. The uncertainty for the uncorrected data points combines statistical and correlated systematic uncertainties.

Figures 6.30 and 6.31 show the comparison between the Z and J/ψ B data for the average charged multiplicity as a function of $p_T(Z \text{ or } J/\psi)$. In the region $p_T(Z \text{ or } J/\psi) < 28 \text{ GeV}/c$, the overall $\langle N_{\text{chg}} \rangle$ rises more rapidly for the J/ψ B than for the Z boson sample. The distribution of both J/ψ B and Z $\langle N_{\text{chg}} \rangle$ can be related to $p_T(Z \text{ or } J/\psi)$ in a linear fashion with different slopes. The greater production of charged particles on average observed from the J/ψ B data is most likely due to the creation of colored particles at the parton level and the multibody decay of the B meson. A B meson in the J/ψ B sample arises from parton interactions which produce b and \bar{b} . The b and \bar{b} may emit gluon radiation before they hadronize into mesons. In addition, the J/ψ is produced in conjunction with other particles when the B meson decays. Only the muons from J/ψ decay are removed from the event. In contrast, the Z boson is created in a hard scattering interaction, emits no gluon radiation, and decays directly to two electrons which are identified and excluded from analysis. The contributions to the overall $\langle N_{\text{chg}} \rangle$ from the toward and away regions must be responsible for the greater overall J/ψ B $\langle N_{\text{chg}} \rangle$ in comparison to the Z boson results. This follows from the observations for $\langle N_{\text{chg}} \rangle$ in the transverse region presented in figure 6.31. Both J/ψ B and Z transverse $\langle N_{\text{chg}} \rangle$ distributions form approximate plateaus in the region $p_T(Z \text{ or } J/\psi) < 28 \text{ GeV}/c$. The average charged multiplicity for the J/ψ B data is constant with $\langle N_{\text{chg}} \rangle \simeq 2.3$ charged particles. The Z $\langle N_{\text{chg}} \rangle$ is larger on average by roughly 0.4 charged particles. The slightly increased activity for the Z data in the transverse region is probably a reflection of the high mass particle ($m(Z) = 91.187 \text{ GeV}$) created in the interaction.

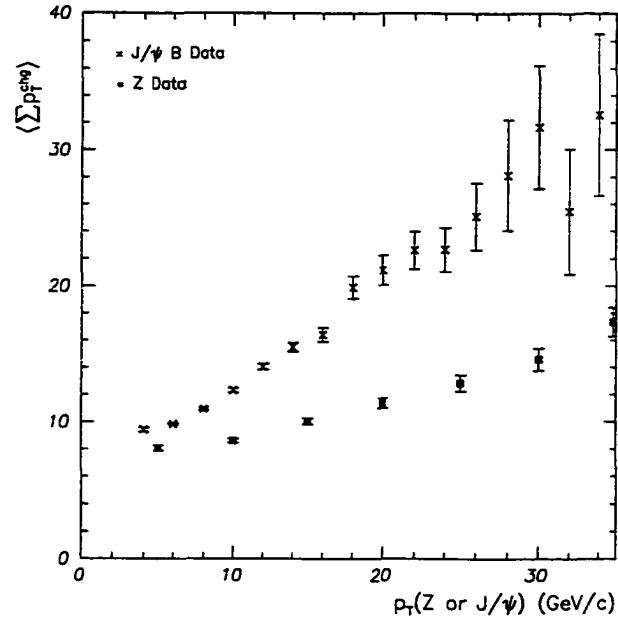


Figure 6.32: Comparison of average scalar p_T sum in the Z boson (solid boxes) sample as a function of $p_T(Z)$ and $J/\psi B$ (crosses) sample as a function of $p_T(J/\psi)$. The bin size for the Z and $J/\psi B$ data is 5 and 2 GeV/c. respectively. The uncertainty for the uncorrected data points combines statistical and correlated systematic uncertainties.

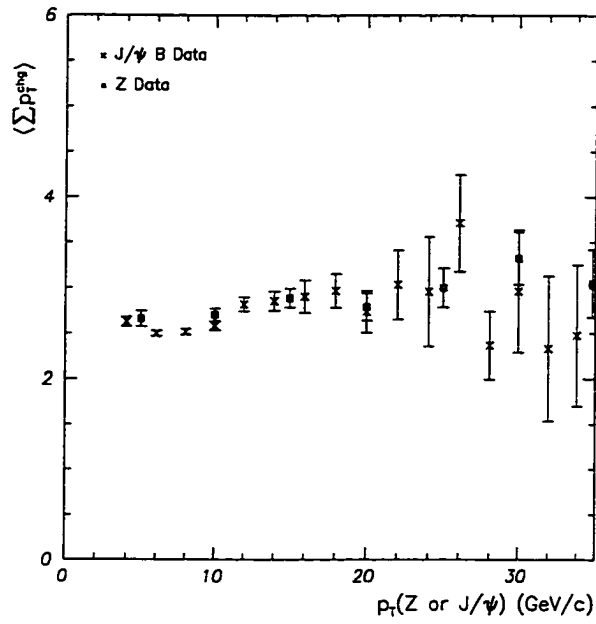


Figure 6.33: Comparison of average scalar p_T sum for the transverse region in the Z boson (solid boxes) sample as a function of $p_T(Z)$ and J/ψ B (crosses) sample as a function of $p_T(J/\psi)$. The bin size for the Z and J/ψ B data is 5 and 2 GeV/c, respectively. The uncertainty for the uncorrected data points combines statistical and correlated systematic uncertainties.

The average scalar p_T sum with respect to $p_T(Z \text{ or } J/\psi)$ for the Z boson and $J/\psi B$ samples is shown in figures 6.32 and 6.33. Linear functions in $p_T(Z \text{ or } J/\psi)$ approximately describe the overall $J/\psi B$ $\langle \sum p_T^{\text{chg}} \rangle$ for $p_T(Z \text{ or } J/\psi) \geq 6 \text{ GeV}/c$ and the overall Z $\langle \sum p_T^{\text{chg}} \rangle$ for $p_T(Z \text{ or } J/\psi) \geq 10 \text{ GeV}/c$. The $J/\psi B$ distribution rises more rapidly than the Z distribution as $p_T(Z \text{ or } J/\psi)$ increases. Although potentially an artifact of the chosen bin size, the apparent discontinuity at $16 < p_T(Z \text{ or } J/\psi) < 18 \text{ GeV}/c$ in the overall $J/\psi B$ $\langle \sum p_T^{\text{chg}} \rangle$ is not present in the Z data. Since the transverse $\langle \sum p_T^{\text{chg}} \rangle$ for both $J/\psi B$ and Z samples are consistent and form a roughly constant plateau, the greater overall $J/\psi B$ $\langle \sum p_T^{\text{chg}} \rangle$ in relation to Z $\langle \sum p_T^{\text{chg}} \rangle$ is the result of contributions from the toward and away regions. Averaging both the transverse $J/\psi B$ and Z $\langle \sum p_T^{\text{chg}} \rangle$ over the full range of $p_T(Z \text{ or } J/\psi)$, a value of $\langle \sum p_T^{\text{chg}} \rangle \simeq 2.7 \text{ GeV}/c$ is determined.

CHAPTER 7 CONCLUSION

An investigation of the event structures in dijet, Z boson, and J/ψ B samples was performed. The dijet and Z boson data were compared to theoretical predictions from QCD hard scattering Monte Carlo generators. The J/ψ B data were analyzed using both the leading charged jet and the J/ψ particle. The leading charged jet and J/ψ behavior of the J/ψ B sample was compared to the dijet and Z boson results, respectively.

To discern the characteristics of the underlying event, a region in ϕ was constructed and carefully studied. The transverse region corresponds to angular differences in the range $60^\circ < |\Delta\phi| \leq 120^\circ$ and allows isolation of components orthogonal to the plane of the 2-to-2 hard scattering processes. The underlying event is formed from beam beam remnants, initial state radiation, and possible soft or hard multiple parton interactions. Since it is present in all collision events at hadron colliders, accurate theoretical predications require a detailed understanding of the underlying event.

7.1 Theoretical Comparisons

The theoretical predictions from HERWIG 5.9, ISAJET 7.32, and PYTHIA 6.115 are compared to dijet and Z boson data. None of the QCD Monte Carlo models correctly describe all of the properties observed in data for the overall event

and the transverse region indicative of the underlying event. In most instances, HERWIG and PYTHIA create results which agree more closely with the data than ISAJET.

HERWIG is employed only to generate parameters appropriate for the dijet sample. The predicted results for the overall average charged multiplicity furnish the closest correlation with data. At lower leading jet transverse momenta, slight features are omitted. While it may reproduce the overall event fairly accurately, HERWIG does not model the underlying event correctly. For the transverse region, HERWIG produces an average charged multiplicity and a scalar p_T sum which underestimates the observations.

ISAJET generally produces distributions of average charged multiplicity and scalar p_T sum which rise too rapidly for either increasing leading charged jet or Z boson transverse momentum. The dijet overall average charged multiplicity is reproduced only at low momentum, after which too many charged particles on average are created. The generated values for dijet, Z boson overall, and Z boson transverse average charged multiplicities all rise too rapidly and only minimally describe any behavior of the data. ISAJET duplicates in an acceptable fashion the observed overall average scalar p_T sum. For transverse average scalar p_T sum in both the dijet and Z samples, the predicted values rise rapidly producing results which do not correspond to the data.

PYTHIA creates values for the average charged multiplicity and scalar p_T sum which agree with much of the data in many of the samples. The distributions for the overall and transverse average charged multiplicities generally have shapes similar to that found in the data. Predictions for the average charged multiplicity in the

Table 7.1: Average charged multiplicity and scalar p_T sum in the transverse regions for the data samples used in this analysis.

Data Sample	Transverse $\langle N_{\text{chg}} \rangle$	Transverse $\langle \sum p_T^{\text{chg}} \rangle$
Dijet	2.2	2.8
Z boson	2.7	3.0
J/ψ B wrt $p_T(\text{jet1})$	2.6	3.0
J/ψ B wrt $p_T(J/\psi)$	2.3	2.8

dijet sample overestimate and in the Z sample underestimate the observations. Of the generators used, PYTHIA most accurately reproduces the behavior and values for the average scalar p_T sum of charged particles in the overall event and the transverse region.

7.2 The Underlying Event

The underlying event should produce the dominant contribution in the transverse region. The transverse average charged multiplicity and scalar p_T sum provide parameters which are employed to ascertain the behavior of the underlying event. Differences are apparent between an underlying event associated with a hard scattering interaction and a soft proton and antiproton collision. The multiplicities determined in this analysis for the underlying event indicate greater activity than for soft collisions.

The average values for the average charged multiplicity and scalar p_T sum corresponding to the flat distributions in the transverse region are provided in table 7.1. The J/ψ B sample was analyzed both with respect to (wrt) the leading charged jet and reconstructed J/ψ transverse momentum. Assuming an uncertainty of

roughly ± 0.1 , the values in the transverse region of the dijet and J/ψ B wrt $p_T(J/\psi)$ data agree as do the Z boson and J/ψ B wrt $p_T(\text{jet1})$ data. The transverse average charged multiplicities determined for the plateaus suggest results which are greater than those observed in soft collisions of protons and antiprotons at $\sqrt{s} = 1.8$ TeV [90].

Comparison of Z boson to J/ψ B wrt $p_T(J/\psi)$ data in the transverse region allows specific characteristics of the underlying event to be determined. Issues concerning the role of particles carrying color charge and the creation of massive particles can be addressed by contrasting the two samples. The transverse average charged multiplicity and scalar p_T sum shown in figures 6.31 and 6.33 indicate that the events on average have distinctive behaviors. The collisions which produce Z bosons have an underlying event with higher average charged multiplicity but the same average scalar p_T sum of charged particles as collisions which produce B mesons decaying to states including a J/ψ .

7.3 Future Endeavors

The creation of samples which are analyzed for overall event topology and the underlying event can be utilized to determine the predictive powers of QCD hard scattering theories and may indicate novel features which require new models. Parameters within Monte Carlo generators can be adjusted to reproduce the distributions observed in the dijet, Z boson, and J/ψ B data. In developing generators that describe the underlying event more faithfully, an important background process to every search for new phenomena at hadron colliders can be reliably

calculated. An increased understanding of the dynamics of the underlying event may also facilitate further comprehension of non-perturbative QCD interactions.

APPENDIX A NOTATION

A.1 Metric, Four Vectors, and Operators

The form of the metric tensor used in this text is

$$g_{\mu\nu} = \begin{pmatrix} 1 & 0 & 0 & 0 \\ 0 & -1 & 0 & 0 \\ 0 & 0 & -1 & 0 \\ 0 & 0 & 0 & -1 \end{pmatrix} . \quad (\text{A.1})$$

The space-time and energy-momentum four vectors are written as

$$x^\mu = (x^0, \mathbf{x}) \quad (\text{A.2})$$

and

$$p^\mu = (E, \mathbf{p}) , \quad (\text{A.3})$$

respectively. From equation A.3, the Lorentz invariant quantity

$$p^2 = E^2 - |\mathbf{p}|^2 = m^2 \quad (\text{A.4})$$

can be determined. The differential operator is defined as

$$\partial_\mu \equiv \frac{\partial}{\partial x^\mu} = \left(\frac{\partial}{\partial x^0}, \nabla \right) . \quad (\text{A.5})$$

The Lorentz invariant d'Alembertian operator is formed from successive use of equation A.5 and is given by

$$\square \equiv \partial_\mu \partial^\mu = \frac{\partial^2}{\partial x^0} - \nabla^2 . \quad (\text{A.6})$$

A.2 Levi-Civita Tensor

The antisymmetric Levi-Civita tensor, $\epsilon^{\mu\nu\rho\sigma}$, satisfies the properties

$$\epsilon^{\mu\nu\rho\sigma} = \begin{cases} +1 & \text{if } \mu, \nu, \rho, \sigma \text{ an even permutation of } 0,1,2,3 \\ -1 & \text{if } \mu, \nu, \rho, \sigma \text{ an odd permutation of } 0,1,2,3 \\ 0 & \text{otherwise} \end{cases} \quad (\text{A.7})$$

and

$$\epsilon_{\mu\nu\rho\sigma} = -\epsilon^{\mu\nu\rho\sigma} . \quad (\text{A.8})$$

Contractions of Levi-Civita tensors can be written as

$$\epsilon^{\mu\nu\rho\sigma} \epsilon_{\mu\nu\rho\sigma} = -24 \quad (\text{A.9})$$

$$\epsilon^{\alpha\beta\gamma\mu} \epsilon_{\alpha\beta\gamma\nu} = -6\delta_\nu^\mu$$

$$\epsilon^{\alpha\beta\mu\nu} \epsilon_{\alpha\beta\rho\sigma} = -2(\delta_\rho^\mu \delta_\sigma^\nu - \delta_\sigma^\mu \delta_\rho^\nu) .$$

APPENDIX B MATRIX PROPERTIES

B.1 Gamma Matrices

The gamma matrices in chiral representation (also known as the Weyl representation) are

$$\gamma^\mu = \begin{pmatrix} 0 & \sigma^\mu \\ \bar{\sigma}^\mu & 0 \end{pmatrix} \quad \text{and} \quad \gamma^5 = \begin{pmatrix} -1 & 0 \\ 0 & 1 \end{pmatrix} \quad (\text{B.1})$$

with

$$\sigma^\mu \equiv (1, \boldsymbol{\sigma}) \quad \text{and} \quad \bar{\sigma}^\mu \equiv (1, -\boldsymbol{\sigma}) . \quad (\text{B.2})$$

The $\boldsymbol{\sigma}$ are the 2×2 Pauli matrices given by

$$\sigma^1 = \begin{pmatrix} 0 & 1 \\ 1 & 0 \end{pmatrix} , \quad \sigma^2 = \begin{pmatrix} 0 & -i \\ i & 0 \end{pmatrix} , \quad \text{and} \quad \sigma^3 = \begin{pmatrix} 1 & 0 \\ 0 & -1 \end{pmatrix} . \quad (\text{B.3})$$

The gamma matrices satisfy the anticommutation relations

$$\{\gamma^\mu, \gamma^\nu\} = 2g^{\mu\nu} \quad \text{and} \quad \{\gamma^\mu, \gamma^5\} = 0 . \quad (\text{B.4})$$

Combinations of variables with γ^0 and γ^μ appear frequently in field theory calculations. Therefore the notation

$$\bar{\psi} \equiv \psi^\dagger \gamma^0 \quad (\text{B.5})$$

and

$$\not{p} \equiv \gamma^\mu p_\mu \quad (\text{B.6})$$

is commonly used.

Evaluating traces and contractions of gamma matrices often occurs when calculating cross sections and scattering amplitudes. Traces of gamma matrices can be eliminated using

$$\text{tr}(\mathbf{1}) = 4 \quad (\text{B.7})$$

$$\text{tr}(\text{odd number of } \gamma \text{ matrices}) = 0$$

$$\text{tr}(\gamma^\mu \gamma^\nu) = 4g^{\mu\nu}$$

$$\text{tr}(\gamma^\mu \gamma^\nu \gamma^\rho \gamma^\sigma) = 4(g^{\mu\nu} g^{\rho\sigma} - g^{\mu\rho} g^{\nu\sigma} + g^{\mu\sigma} g^{\nu\rho})$$

$$\text{tr}(\gamma^5) = 0$$

$$\text{tr}(\gamma^\mu \gamma^\nu \gamma^5) = 0$$

$$\text{tr}(\gamma^\mu \gamma^\nu \gamma^\rho \gamma^\sigma \gamma^5) = -4i\epsilon^{\mu\nu\rho\sigma}.$$

The order of gamma matrices within traces can be inverted in the following manner

$$\text{tr}(\gamma^\mu \gamma^\nu \gamma^\rho \dots) = \text{tr}(\dots \gamma^\rho \gamma^\nu \gamma^\mu) . \quad (\text{B.8})$$

Similarly, contractions of gamma matrices can be simplified by using

$$\begin{aligned} \gamma^\mu \gamma_\mu &= 4 \\ \gamma^\mu \gamma^\nu \gamma_{\mu\nu} &= -2\gamma^\nu \\ \gamma^\mu \gamma^\nu \gamma^\rho \gamma_\mu &= 4g^{\nu\rho} \\ \gamma^\mu \gamma^\nu \gamma^\rho \gamma^\sigma \gamma_\mu &= -2\gamma^\sigma \gamma^\rho \gamma^\nu . \end{aligned} \quad (\text{B.9})$$

B.2 Gell-Mann Matrices

The Gell-Mann matrices are written as

$$\begin{aligned}
 \lambda_1 &= \begin{pmatrix} 0 & 1 & 0 \\ 1 & 0 & 0 \\ 0 & 0 & 0 \end{pmatrix} & \lambda_2 &= \begin{pmatrix} 0 & -i & 0 \\ i & 0 & 0 \\ 0 & 0 & 0 \end{pmatrix} & \lambda_3 &= \begin{pmatrix} 1 & 0 & 0 \\ 0 & -1 & 0 \\ 0 & 0 & 0 \end{pmatrix} \\
 \lambda_4 &= \begin{pmatrix} 0 & 0 & 1 \\ 0 & 0 & 0 \\ 1 & 0 & 0 \end{pmatrix} & \lambda_5 &= \begin{pmatrix} 0 & 0 & -i \\ 0 & 0 & 0 \\ i & 0 & 0 \end{pmatrix} & \lambda_6 &= \begin{pmatrix} 0 & 0 & 0 \\ 0 & 0 & 1 \\ 0 & 1 & 0 \end{pmatrix} \\
 \lambda_7 &= \begin{pmatrix} 0 & 0 & 0 \\ 0 & 0 & -i \\ 0 & i & 0 \end{pmatrix} & \lambda_8 &= \frac{1}{\sqrt{3}} \begin{pmatrix} 1 & 0 & 0 \\ 0 & 1 & 0 \\ 0 & 0 & -2 \end{pmatrix}
 \end{aligned} \tag{B.10}$$

The generators of the $SU(3)$ group can be written as

$$T_\alpha = \frac{1}{2} \lambda_\alpha \tag{B.11}$$

where α takes values of 1 to 8. The generators obey the commutation relation

$$[T_\alpha, T_\beta] = i f_{\alpha\beta\gamma} T_\gamma \tag{B.12}$$

and the anticommutation relation

$$\{T_\alpha, T_\beta\} = \frac{1}{3} \delta_{\alpha\beta} + d_{\alpha\beta\gamma} T_\gamma \tag{B.13}$$

where $f_{\alpha\beta\gamma}$ and $d_{\alpha\beta\gamma}$ are the antisymmetric and symmetric structure constants, respectively. The non-zero values for $f_{\alpha\beta\gamma}$ are given by

α	β	γ	$f_{\alpha\beta\gamma}$
1	2	3	1
1	4	7	1/2
1	5	6	-1/2
2	4	6	1/2
2	5	7	1/2
3	4	5	1/2
3	6	7	-1/2
4	5	8	$\sqrt{3}/2$
6	7	8	$\sqrt{3}/2$

whereas the non-zero values for $d_{\alpha\beta\gamma}$ are given by

α	β	γ	$d_{\alpha\beta\gamma}$
1	1	8	$1/\sqrt{3}$
1	4	6	$1/2$
1	5	7	$1/2$
2	2	8	$1/\sqrt{3}$
2	4	7	$-1/2$
2	5	6	$1/2$
3	3	8	$1/\sqrt{3}$
3	4	4	$1/2$
3	5	5	$1/2$
3	6	6	$-1/2$
3	7	7	$-1/2$
4	4	8	$-1/(2\sqrt{3})$
5	5	8	$-1/(2\sqrt{3})$
6	6	8	$-1/(2\sqrt{3})$
7	7	8	$-1/(2\sqrt{3})$
8	8	8	$-1/\sqrt{3}$

Jacobi equations for the structure constants exist and are

$$f_{\alpha\beta\epsilon}f_{\epsilon\gamma\delta} + f_{\gamma\beta\epsilon}f_{\alpha\epsilon\delta} + f_{\delta\beta\epsilon}f_{\alpha\gamma\epsilon} = 0 \quad (\text{B.14})$$

$$f_{\alpha\beta\epsilon}d_{\epsilon\gamma\delta} + f_{\gamma\beta\epsilon}d_{\gamma\epsilon\delta} + f_{\delta\beta\epsilon}d_{\alpha\gamma\epsilon} = 0$$

APPENDIX C DATA SYSTEMATICS

In section 5.3, the systematic uncertainty for the data was found to be dominated by changes in impact parameter requirements. A method for determining the uncertainty was formulated using the difference between data obtained with a 0.5 cm and no impact parameter requirement. To further insure that the procedure produces reliable values, the QFL detector simulation package is employed [91, 92].

Theoretical predictions of the dijet sample are produced by PYTHIA 6.157 and the generated particle lists are submitted to the QFL algorithm. Each Monte Carlo file contains 15,000 events. Four files corresponding to the hard 2-to-2 scattering process momenta $p_T^{\text{hard}} \geq 3, 10, 20, \text{ and } 30 \text{ GeV}/c$ are created. Particles coincident with the location in pseudorapidity of the beam beam counters are required. Monte Carlo and QFL events are subjected to the same track selection criteria. Systematic uncertainties are determined by comparing the observable quantities before and after QFL simulation. The results for the overall and transverse average charge multiplicity uncertainties as a function of the leading charged jet are shown in figures C.1 and C.2.

The uncertainties derived from the Monte Carlo and QFL analysis are generally less than those determined from data by varying impact parameter criteria. Only two values in figure C.1 result in greater uncertainty from Monte Carlo and QFL simulation. For the transverse region, this number increases to 8 with a maximal difference between these uncertainties of only ~ 0.4 . Therefore, in comparison

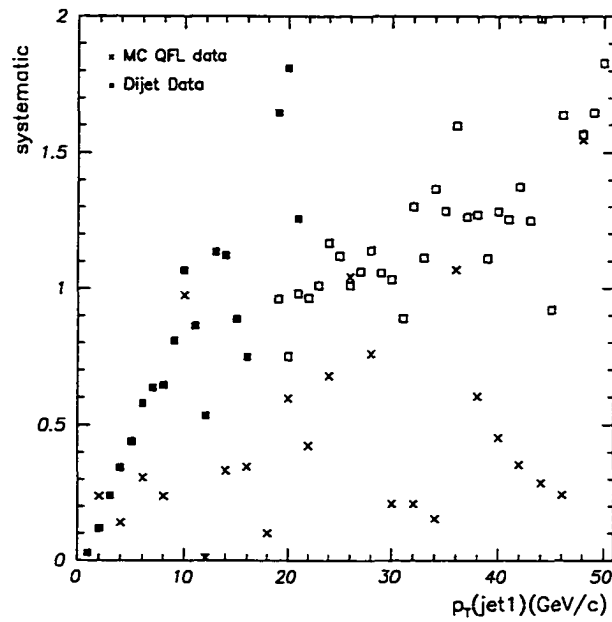


Figure C.1: Systematic uncertainty associated with the overall average charge multiplicity as a function of the leading charged jet for the dijet sample. The solid and open boxes represent the uncertainty from the Min-Bias and Jet20 data with bin size 1 GeV/c in $p_T(\text{jet1})$, respectively. The crosses are systematics in 2 GeV/c bins derived from Monte Carlo and QFL.

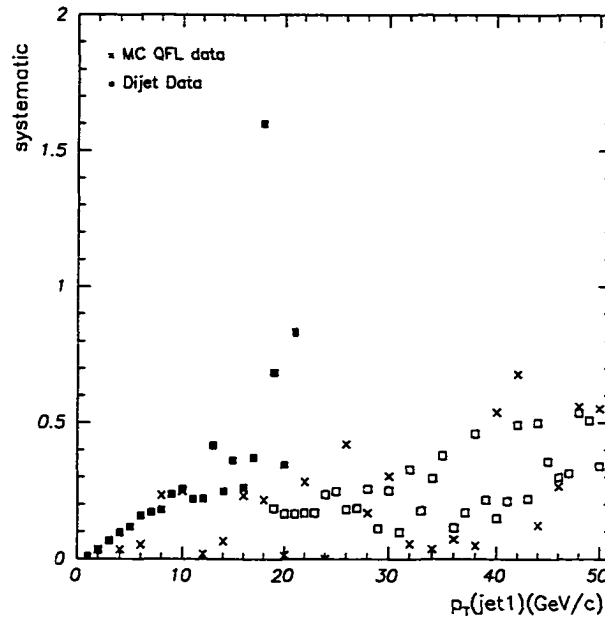


Figure C.2: Systematic uncertainty associated with the transverse average charge multiplicity as a function of the leading charged jet for the dijet sample. The solid and open boxes represent the uncertainty from the Min-Bias and Jet20 data with bin size 1 GeV/c in $p_T(\text{jet1})$, respectively. The crosses are systematics in 2 GeV/c bins derived from Monte Carlo and QFL.

to the Monte Carlo and QFL generated systematics. the uncertainties determined from impact parameter requirements applied to the data represent conservative estimates.

-

REFERENCES

- [1] F. Reines and C. Cowan, Jr. *Physical Review*, 92:830, 1953.
- [2] B. Pontecorvo. *Soviet Physics JETP*, 37:1236. 1960.
- [3] G. Danby *et al.* *Physical Review Letters*, 9:36. 1962.
- [4] M. Gell-Mann and Y. Ne'eman. *The Eightfold Way*. W.A. Benjamin, New York, 1964.
- [5] M. Gell-Mann. *Physics Letters*, 8:214, 1964.
- [6] G. Zweig. An $SU(3)$ Model for Strong Interaction Symmetry and its Breaking I. Preprint CERN-8182-TH-401, 1964.
- [7] O.W. Greenberg. *Physical Review Letters*. 13:598, 1964.
- [8] M. Breidenbach *et al.* *Physical Review Letters*, 23:935, 1969.
- [9] J.J. Aubert *et al.* *Physical Review Letters*. 33:1404, 1974.
- [10] J.E. Augustin *et al.* *Physical Review Letters*. 33:1406, 1974.
- [11] M. Perl *et al.* *Physical Review Letters*, 35:1489, 1975.
- [12] S.W. Herb *et al.* *Physical Review Letters*, 39:252, 1977.
- [13] S.L. Glashow. *Nuclear Physics*, B22:579, 1961.
- [14] S. Weinberg. *Physical Review Letters*, 19:1264, 1967.
- [15] A. Salam. In N. Svartholm, editor, *Elementary Particle Theory*, page 367. Almquist and Wiskell, 1968.
- [16] G. Arnison *et al.* *Physics Letters*, 122B:103, 1983.
- [17] G. Arnison *et al.* *Physics Letters*, 126B:398, 1983.
- [18] CDF Collaboration, F. Abe *et al.* *Physical Review Letters*. 74:2626, 1995.

- [19] D0 Collaboration, S. Abachi *et al.* *Physical Review Letters*, 74:2632, 1995.
- [20] DONUT Collaboration, K. Kodama *et al.* *Submitted to Physics Letters B*. 2001. Preprint at LANL hep-ex/0012035.
- [21] Super-Kamiokande Collaboration, Y. Fukuda *et al.* *Physical Review Letters*. 81:1562, 1998.
- [22] D.E. Groom *et al.* *The European Physical Journal*, C15:1, 2000.
- [23] The Top Averaging Group, L. Demortier *et al.* Combining the top quark mass results for Run 1 from CDF and D0. Preprint FERMILAB-TM-2084. 1999.
- [24] M. Goldhaber, L. Grodzins, and A. Sunyar. *Physical Review*. 109:1015. 1958.
- [25] M. Bardon *et al.* *Physical Review Letters*, 7:23, 1961.
- [26] J. Erler and P. Langacker. Status of the Standard Model. In *Proceedings of the 5th International WEIN Symposium (WEIN 98)*, page 1. Santa Fe. NM. June 1998.
- [27] S. Weinberg. *Physical Review D*, 19:1277, 1979.
- [28] L. Susskind. *Physical Review D*, 20:2619, 1979.
- [29] E. Eichten, I. Hinchliffe, K. Lane, and C. Quigg. *Physical Review D*. 34:1547. 1986.
- [30] S. Martin. A Supersymmetry Primer. In G. Kane, editor, *Perspectives on Supersymmetry*, page 1. World Scientific, Singapore, 1997.
- [31] J.C. Pati and A. Salam. *Physical Review D*, 8:1240, 1973.
- [32] H. Georgi and S. Glashow. *Physical Review Letters*, 32:438, 1974.
- [33] E. Farhi and L. Susskind. *Physics Reports*, 74:277, 1981.
- [34] K. Lane and M. Ramana. *Physical Review D*, 44:2678, 1991.
- [35] CDF Collaboration, T. Affolder *et al.* *Physical Review Letters*, 85:2056, 2000.
- [36] N. Arkani-Hamed, S. Dimopoulos, and G. Dvali. *Physics Letters*, B429:263. 1998.
- [37] R.D. Field. *Applications of Perturbative QCD*. Addison-Wesley, Redwood City, CA, 1989.

- [38] W. Caswell. *Physical Review Letters*, 33:244, 1974.
- [39] S. Coleman and D.J. Gross. *Physical Review Letters*, 31:851, 1973.
- [40] H. Plathow-Besch. PDFLIB: Proton, Pion and Photon Parton Density Functions, Parton Density Functions of the Nucleus, and α_s Calculations. Preprint CERN-ETT/TT, 2000.
- [41] CDF Collaboration, T. Affolder *et al.* *To be submitted to Physical Review D*. 2001.
- [42] R. Field, H. Frisch, R. Haas, and D. Stuart. The Underlying Event: Dijet vs. Z-jet. CDF internal publication 5295, 2000.
- [43] R. Field and R. Haas. The Underlying Event in $B J/\psi$ Data. In Progress. 2001.
- [44] T. Sjöstrand. *Computer Physics Communications*, 82:74, 1994.
- [45] S. Catani, G. Marchesini, and B.R. Webber. *Nuclear Physics*. B349:635, 1991.
- [46] G. Marchesini, B.R. Webber, G. Abbiendi, I.G. Knowles, M.H. Seymour, and L. Stanco. *Computer Physics Communications*, 67:465, 1992.
- [47] H. Baer, F. Paige, S. Protopopescu, and X. Tata. ISAJET 7.48: A Monte Carlo Event Generator for pp , $\bar{p}p$, and e^+e^- Reactions. Preprint at LANL hep-ph/0001086, 1999.
- [48] T. Sjöstrand, P. Edén, C. Friberg, L. Lönnblad, G. Miu. S. Mrenna, and E. Norrbin. *Submitted to Computer Physics Communications*, 2000. Preprint at LANL hep-ph/0010017.
- [49] UA5 Collaboration, G. Alner *et al.* *Nuclear Physics*, B291:445, 1987.
- [50] D. Amati and G. Veneziano. *Physics Letters*, B83:87, 1979.
- [51] Y. Azimov, Y. Dokshitzer, V. Khoze, and S. Troyan. *Physics Letters*. B165:147, 1985.
- [52] Y. Azimov, Y. Dokshitzer, V. Khoze, and S. Troyan. *Zeitschrift für Physik C*, 27:65, 1985.
- [53] B. Webber. *Nuclear Physics*, B238:492, 1984.

- [54] Y. Dokshitzer, V. Khoze, A. Mueller, and S. Troyan. *Basics of Perturbative QCD*. Editions Frontières, Singapore, 1991.
- [55] V. Abramovsky, V. Gribov, and O. Kancheli. *Yadernaya Fizika*, 18:595, 1973.
- [56] P.D.B. Collins. *An Introduction to Regge Theory and High Energy Physics*. Cambridge University Press, Cambridge, 1977.
- [57] R.D. Field and R.P. Feynman. *Nuclear Physics*, B136:1, 1978.
- [58] B. Andersson, G. Gustafson, G. Ingelman, and T. Sjöstrand. *Physics Reports*, 97:31, 1983.
- [59] J. Thompson. Introduction to Colliding Beams at Fermilab. Preprint FERMILAB-TM-1909, 1994.
- [60] Fermilab WWW document. Concepts Rookie Book. Located at <http://www-bd.fnal.gov/operations/r-okie.books/concepts/conceptstoc.html>. April 2000.
- [61] D.H. Perkins. *Introduction to High Energy Physics*. Addison-Wesley, Menlo Park, CA, 1987.
- [62] J.R. Sanford. *Annual Review of Nuclear and Particle Science*, 26:151, 1976.
- [63] Fermilab WWW document. Pbar Rookie Book. Located at <http://www-bd.fnal.gov/operations/rookie.books/pbar.book/contents.html>. April 2000.
- [64] A.V. Tollestrup and G. Dugan. Elementary Stochastic Cooling. Preprint FERMILAB-TM-1227, 1983.
- [65] A.G. Ruggiero. *IEEE Transactions on Nuclear Science*, 30:2478, 1983.
- [66] B. Autin, J. Marriner, A. Ruggiero, and K. Takayama. Fast Betatron Cooling in the Debuncher Ring for the Fermilab Tevatron I Project. *IEEE Transactions on Nuclear Science*, 30:2593, 1983.
- [67] CDF Collaboration, F. Abe *et al.* *Nuclear Instruments and Methods in Physics Research*, Sect. A 350:74, 1994.
- [68] CDF Collaboration, F. Abe *et al.* *Nuclear Instruments and Methods in Physics Research*, Sect. A 271:387, 1988.
- [69] S. Tkaczyk *et al.* *Nuclear Physics*, A342:240, 1994.
- [70] D. Amidei *et al.* *Nuclear Physics*, A350:73, 1994.

- [71] D. Amidei *et al.* *Nuclear Instruments and Methods in Physics Research*, A360:137, 1995.
- [72] A. Warburton. Run 1A and 1B Low- p_T Single- and Double-Track CTC Pattern Recognition Efficiencies. CDF internal publication 4139, 1997.
- [73] CDF Collaboration, F. Abe *et al.* *Physical Review D*, 50:2966, 1994.
- [74] D. Cronin-Hennessy, A. Beretvas, and P. Derwent. *Nuclear Instruments and Methods in Physics Research*, 443:37, 2000.
- [75] CDF Collaboration, F. Abe *et al.* *Physical Review Letters*, 76:3070, 1996.
- [76] CDF Collaboration, F. Abe *et al.* *Physical Review D*, 50:5550, 1994.
- [77] P. Derwent, C. Pilcher, and S. Belforte. $\sigma_{B\bar{B}C}$ Derivation. Results, and Proposal for New Normalization. CDF internal publication 2361, 1994.
- [78] D. Amidei *et al.* *Nuclear Instruments and Methods in Physics Research*, A269:51, 1988.
- [79] A. Korytov and A. Safonov. CTC Track Reconstruction Efficiency in Jets. CDF internal publication 4883, 1999.
- [80] R. Field and D. Stuart. The Underlying Event in Hard Scattering. CDF internal publication 5244, 2000.
- [81] CDF Collaboration, F. Abe *et al.* *Physical Review D*, 52:2624, 1995.
- [82] CDF Collaboration, F. Abe *et al.* *Physical Review Letters*, 77:2616, 1996.
- [83] CDF Collaboration, T. Affolder *et al.* *Physical Review Letters*, 84:845, 2000.
- [84] CDF Collaboration, F. Abe *et al.* *Physical Review D*, 57:5382, 1998.
- [85] CDF Collaboration, T. Affolder *et al.* *Physical Review Letters*, 85:2886, 2000.
- [86] S. Pappas, J. Lewis, and G. Michail. Run 1B Low p_T Central Dimuon Trigger Efficiencies. CDF internal publication 4076, 1997.
- [87] H. Wenzel, D. Benjamin, A. Sill, D. Stuart, and R. Snider. Beamlines. CDF internal publication 3334, 1995.
- [88] CDF Collaboration, F. Abe *et al.* *Physical Review D*, 45:1448, 1992.

- [89] R. Field. The Sources of b Quarks at the Tevatron. CDF internal publication 5558, 2001.
- [90] CDF Collaboration, F. Abe *et al.* *Physical Review D*, 41:2330, 1990.
- [91] M. Shapiro, D. Brown, and S. Kannappan. QFL Version 2.0: Improvements and Checks. CDF internal publication 753, 1988.
- [92] A. Caner. CDFSIM+QFL Simulation of the CDF Detector. CDF internal publication 2177, 1993.

BIOGRAPHICAL SKETCH

Richard Haas [REDACTED]
[REDACTED]


[REDACTED] During high school and college, Richard resided in New Hampshire. He relocated to Florida to attend the doctoral program in physics at the University of Florida.

Richard graduated from Phillips Exeter Academy and matriculated at Dartmouth College in 1990. While at Dartmouth, he pursued degrees in physics and philosophy. In the summer of 1992, Richard joined a research group investigating the behavior of plasma in the magnetosphere. He created computational algorithms which generated theoretical predictions and compared results to AMPTE/IRM satellite data. During his senior year, Richard examined the evolution and behavior of Gaussian wavepackets subject to different conditions according to a quantum mechanical formulation. He was awarded a degree in physics with high honors for this work and a degree in philosophy upon graduation in 1994.

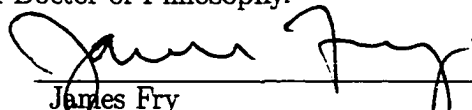
In order to continue an analysis started during his last term as a senior, Richard enrolled as a master's student at Dartmouth College. Field configurations which modeled pseudo-stable false vacuum states in theories of the electroweak phase transition were investigated. Richard worked at Fermilab for several months in the astronomy and astrophysics group with his advisor, Marcelo Gleiser. Richard graduated from Dartmouth with a Master of Science degree in 1995.

In 1996, Richard enrolled in the physics Ph.D. program at the University of Florida. He began work with his advisor, Rick Field, in 1997 calculating various quantum chromodynamical effects. The allure of comparing predictions to real data compelled both advisor and student to join the Collider Detector at Fermilab (CDF) collaboration in 1998. Richard officially became a member of CDF in 1999.

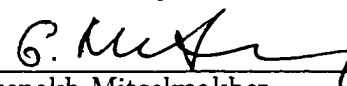
I certify that I have read this study and that in my opinion it conforms to acceptable standards of scholarly presentation and is fully adequate, in scope and quality, as a dissertation for the degree of Doctor of Philosophy.


Richard Field, Chairman
Professor of Physics

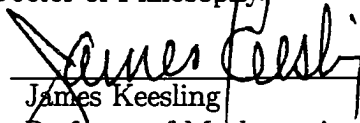
I certify that I have read this study and that in my opinion it conforms to acceptable standards of scholarly presentation and is fully adequate, in scope and quality, as a dissertation for the degree of Doctor of Philosophy.


James Fry
Professor of Physics

I certify that I have read this study and that in my opinion it conforms to acceptable standards of scholarly presentation and is fully adequate, in scope and quality, as a dissertation for the degree of Doctor of Philosophy.


Guenakh Mitselmakher
Professor of Physics

I certify that I have read this study and that in my opinion it conforms to acceptable standards of scholarly presentation and is fully adequate, in scope and quality, as a dissertation for the degree of Doctor of Philosophy.


James Keesling
Professor of Mathematics

This dissertation was submitted to the Graduate Faculty of the Department of Physics in the College of Liberal Arts and Sciences and to the Graduate School and was accepted as partial fulfillment of the requirements for the degree of Doctor of Philosophy.

August 2001


Dean, Graduate School



2017 ProQuest Distribution Agreement

This Agreement is between the author (Author) and ProQuest LLC, through its ProQuest Dissertation Distribution business (formerly ProQuest/UMI). Under this Agreement, Author grants ProQuest certain rights to preserve, archive and distribute the dissertation or thesis (the Work), abstract, and index terms provided by Author to ProQuest.

Section I. License for Inclusion of the Work in ProQuest Publishing Program

Grant of Rights. Author hereby grants to ProQuest the **non-exclusive**, worldwide right to reproduce, distribute, display and transmit the Work (in whole or in part) in such tangible and electronic formats as may be in existence now or developed in the future. Author further grants to ProQuest the right to include the abstract, bibliography and other metadata in the ProQuest Dissertations & Theses database (PQDT) and in ProQuest Dissertation Abstracts International and any successor or related index and/or finding products or services.

ProQuest Publishing Program - Election and Elements. The rights granted above shall be exercised according to the publishing option selected by Author in Section III, Author Options, and subject to the following additional Publishing Program requirements:

- **Distribution of the Work.** Except as restricted by Author in the publishing option selected, the rights granted by Author automatically include (1) the right to allow sale and distribution of the Work, in whole or in part, by ProQuest and its sales agents and distributors and (2) the right to make the Abstract, bibliographic data and any meta data associated with the Work available to search engines and harvesters.
- **Restrictions.** ProQuest will use commercially reasonable efforts to restrict the distribution of the Work as provided under the publishing option selected by Author or *as later elected by Author* through direct contact with ProQuest. Such election is subject to Author's Degree Granting Institution Directives. With respect to restrictions requested after submission of the Work, Author acknowledges that ProQuest cannot recall or amend previously distributed versions of the Work.
- **Removal of Work from the Program.** ProQuest may elect not to distribute the Work if it believes that all necessary rights of third parties have not been secured. Refer to the website http://www.proquest.com/products_umi/dissertations/ for information about copyright and your dissertation or thesis. If Author's degree is rescinded, and/or the degree-granting institution so directs, ProQuest will expunge the Work from its publishing program in accordance with its then current publishing policies.
- **Degree Granting Institution Directives.** Author is solely responsible for any conflict between policies and directions of Author's degree-granting institution, Author's choice of publishing model, and/or any restriction Author places on the use of the Work. For the avoidance of doubt, ProQuest is not responsible for access to the Work that is provided by Author's degree-granting institution through its library or institutional repository. Author must work directly with Author's degree granting institution to ensure application of any restrictions to access relating to the Work by Author's degree granting institution.

Delivery of the Work. Author shall provide to ProQuest the Work and all necessary supporting documents during the online submission process, according to the Instructions accompanying this agreement.

Rights Verification. Author represents and warrants that Author is the copyright holder of the Work and has obtained all necessary rights to permit ProQuest to reproduce and distribute third party materials contained in any part of the Work, including all necessary licenses for any non-public, third party software necessary to access, display, and run or print the Work. Author is solely responsible and will indemnify ProQuest for any third party claims related to the Work as submitted for publication.

Open Access Publishing Plus

- ☒ I want the broadest possible dissemination of my work, and I want to provide free global access to the electronic copy of my work via the internet.
- ☒ I understand that I will not be eligible to receive royalties.

I want major search engines (e.g. Google, Yahoo) to discover my work. Learn more: <http://www.proquest.com/en-US/products/dissertations/google.shtml>

- ☒ Yes
- ☐ No

Acknowledgment: I have read, understand and agree to this ProQuest Publishing Agreement, including all rights and restrictions included within the publishing option chosen by me as indicated above.

REQUIRED Author's signature

Date

8/21/17

(Print Name) Richard Haas

Institution conferring degree University of Florida

Committee Member _____ Committee Member _____

Language of manuscript English

Primary Subject Category: Enter the 4-digit code and category name from the Subject Category Guide that most closely describes the area of your research. Code 0798 Category Particle Physics

You may suggest two additional subject categories that may aid in the discovery of your work in our digital database.

Code _____ Category _____ Code _____ Category _____

Provide up to 6 keywords or short phrases for citation indices, library cataloging, and database searching.

High Energy Particle Physics Proton Antiproton Collisions Quantum Chromodynamics

Monte Carlo Models

Current Contact Information Current Email Address rhaas06@gmail.com

Street Address _____

Please provide your postal address if you are interested in receiving royalties on sales of your thesis.

City _____ Province _____ Daytime Phone _____

Country _____ Postal Code _____ Evening Phone _____

Permanent Contact Information

Permanent Email Address rhaas06@gmail.com

Street Address (line 1) _____

City _____ Province _____ Future Phone _____

Country _____ Postal Code _____ Alternate Future Phone _____

THIS PAGE MUST ACCOMPANY YOUR MANUSCRIPT AND THE REST OF YOUR SUBMISSION MATERIALS

Subject Categories

The ProQuest Dissertations & Theses (PQDT) database and the ProQuest citation indices are arranged by subject categories. Please select the one category below that best describes your field of research or creative work. You may add one or two additional categories on your submission form that will also be associated with your work as secondary subjects.

Arts, Business, Education, Humanities, and Social Sciences

AREA, ETHNIC, AND GENDER STUDIES

African American studies	0296
African studies	0293
American studies	0323
Asian American studies	0343
Asian studies	0342
Baltic studies	0361
Black studies	0325
Canadian studies	0385
Caribbean studies	0432
Classical studies	0434
East European studies	0437
Ethnic studies	0631
European studies	0440
French Canadian culture	0482
Gender studies	0733
GLBT studies	0492
Hispanic American studies	0737

Holocaust studies	0507
Islamic culture	0512
Judaic studies	0751
Latin American studies	0550
Middle Eastern studies	0555
Native American studies	0740
Near Eastern studies	0559
North African studies	0560
Pacific Rim studies	0561
Regional studies	0604
Scandinavian studies	0613
Slavic studies	0614
South African studies	0654
South Asian studies	0638
Sub Saharan Africa studies	0639
Women's studies	0453

BUSINESS

Accounting	0272
Arts management	0424
Banking	0770
Business	0310
Entrepreneurship	0429
Finance	0508
Management	0454
Marketing	0338
Sports management	0430

COMMUNICATIONS AND INFORMATION SCIENCES

Communication	0459
Information science	0723
Journalism	0391
Library science	0399
Mass communication	0708
Technical communication	0643

This page must accompany your manuscript and the rest of the submission materials

Please check type of manuscript:

☐ M (Master's Thesis)

☒ D (Dissertation)

Dissertation/Master's Thesis Submission Form

Please print clearly in block letters

Personal Information

Last Name	<u>Haas</u>	Middle Name or Initial	<u></u>
First Name	<u>Richard</u>	Country (ies) of Citizenship	<u>USA</u>

Degree & Dissertation Information

Title of Dissertation/ Thesis	<u>The Underlying Event in Hard Scattering Collisions of Proton and Antiproton at 1.8 TeV</u>		
Institution conferring degree	<u>University of Florida</u>	Degree awarded (abbreviate; e.g., Ph.D.)	<u>PhD</u>
College, School, or Division	<u></u>	Year degree awarded	<u>2001</u>
Department or Program	<u>Department of Physics</u>	Year manuscript completed	<u>2001</u>
Advisor/Committee Chair	<u>Richard Field</u>		
Committee Member	<u>James Fry</u>	Committee Member	<u>James Keesling</u>
Committee Member	<u>Guenakh Mitselmakher</u>	Committee Member	<u></u>